Effective Field Theory Analysis and Active Neutron Veto Design for the Cryogenic Dark Matter Search

A THESIS
SUBMITTED TO THE FACULTY OF THE GRADUATE SCHOOL
OF THE UNIVERSITY OF MINNESOTA
BY

Hannah Elizabeth Rogers

IN PARTIAL FULFILLMENT OF THE REQUIREMENTS
FOR THE DEGREE OF
Doctor of Philosophy

Vuk Mandic, Advisor

May, 2018

Acknowledgements

No good physicists work without help from those around them. Therefore, like every scientist before me, there are many people I would like to acknowledge, without whom I would not have successfully made it through to a doctorate in physics.

My thesis was most directly shaped by my advisor, Vuk Mandic, and unofficial second advisor, Prisca Cushman. I have learned more from their guidance and leadership than any other source. I am grateful for the hours you spent reading and editing my papers and for the opportunity to learn from your expertise. Thank you both for letting me work with you in CDMS for the past five years!

My experience at the University of Minnesota would not have been complete without the rest of of the CDMS team. The postdocs at UMN have all been good scientist role models for me. Working with Hassan Chagani in the cryogenic lab taught me what it really meant to be a physicist, and the advice I've received from Anthony Villano and Matt Fritts have been invaluable in both my research and my time in grad school. The graduate students and lab technicians, both past and current, in the CDMS group have also helped me in many ways. Allison Kennedy, Roxanne Radpour, David Strandberg, and Nick Mast were good company in the cryolab and taught me more than I ended up needing to know about running a cryogenic refrigerator. Scott Fallows, Tommy Hofer, Mark Pepin, Florian Livet, D'Ann Barker, Jack Nelson, and Derek Sincavage have all been entertaining and helpful office mates as well. No list of "thank you"s would be complete without mentioning the undergraduate students I have worked with. I enjoyed wasting time with and hearing stories from Alex Codoreanu, Chris Pheneci, and Dan Codoluto in the cryolab and working with Alex Medved, David-Michael Poehlmann, Ryan Schmitz, and Tanmay Agarwal in the scintillator lab.

I appreciate that CDMS has collaborators outside of the physics department. We

would not have been able to start the polymerizing process without the help of Marc Hillmyer and his student Jake Brutman of the UMN chemistry department. I am also grateful for the CDMS collaborators that have taken an interest in and put in their time to improve my research and published papers. First and foremost here is David Cerdeño, who has helped guide and shape my EFT analysis almost as much as Vuk! I would also like to thank Ray Bunker, Rob Caulkins, Blas Cabrera, Scott Oser, Wolfgang Rau, Steve Yellin, Kristi Schneck, and Bill Page for their contributions towards making sure my research is thorough and correct.

My time at UMN was made more enjoyable by my fellow graduate students. I would not have survived first and second year classes without the help from Chris Conklin, Julie Vievering, Andy Julin, Pat Meyers, Zach Lesko, Peter Hansen, Allison Kennedy, D'Ann Barker and others. I am also grateful for the many social activities than Chris, Julie, and Karlen Shahinyan would plan as well as the CMS group that I frequently have lunch with (Zach, Peter, Josh Hiltbrand, Michael Revering, and Neil Schroeder).

Before I made it into graduate school, there were professors and teachers who made this thesis possible. From Augustana College, I would like to thank my physics professors (Erik Wells, Drew Alton, and Nathan Grau) for providing me with a high quality and personalizable physics education. As my first research advisor, Drew Alton also gave me my first introduction to dark matter. My physical chemistry professor, Bijoy Dey, taught me physics from a different perspective and how applicable even the most theoretically-based physics could become. One of my math teachers from Wayzata High School, William Skerbitz is responsible for me even considering physics to begin with. If he had not taken it upon himself to design and teach a Linear Algebra/Differential Equations course for students who finished AP Calc in their junior year, I would have never seen physics as the most exciting practical application of high level mathematics.

The people who should take the most credit for this accomplishment are my parents, Ann and Steve, although they may sometimes feel bewildered as to where my inclination for science and mathematics came from. They provided my sister, Kristina, and me with access to as many educational and science opportunities as we were interested in, and my mother especially, strived to make learning fun for us from a very young age. I want to thank them for raising me to never question the fact that women can accomplish whatever goals they might have, whether that was their intention or not. I would also

like to thank Kristina for always being somebody worth competing against. I doubt I would have done as well in school if you weren't always one step ahead of me. Without the support of my family, I would never have made it this far.

No acknowledgment is complete without mentioning the furry friends that have kept me sane. My two-and-a-half year old miniature schnauzer, Fredericka, is the best companion I could ask for. Late nights are made much better when she insists on snuggling up next to me while I work. Mitch's cat Mango has grown on me, and his incessant purring behind my head has been a good soundtrack to work to as well. I've also always enjoyed seeing Prisca's dogs, Xena and Pepper, when they were in her office.

Last, but definitely not least, I would like to thank my amazing boyfriend, Mitch Kinney, for the many roles he has played in helping me finish my thesis. These range from stress relief and a welcome distraction, to support and encouragement, to being my expert statistician and making sure I understand all the nuances of the statistical analysis in my thesis. I don't know how I would have made it through these last few years without you!

Dedication

to The Learning Company, the creators of the DOS game Super Solvers: Gizmos & Gadgets, my first real introduction to physics

Abstract

Astrophysical measurements and cosmological predictions suggest the exists of a large amount of matter in the universe that does not interact via electromagnetic forces. This non-luminescent matter, known dark matter, exists in halos that encompass and are within galaxies, including the Milky Way. Therefore, dark matter particles should should be directly detectable by experiments on Earth, such as the Super Cryogenic Dark Matter Search (SuperCDMS). Dark matter is assumed to be low mass (< 100 GeV/c^2) and interact via the weak force using either a spin-independent or spin-dependent coupling. However, making incorrect assumptions about dark matter interactions can lead to misleading results. Because interactions with dark matter particles are rare, direct detection experiments must be able to shield for or reject backgrounds to very low levels. Low energy neutron backgrounds that make it to the detectors are especially dangerous, because they cannot be easily distinguished from the expected dark matter signal.

Scintillator doped with a high neutron-capture cross-section material can be used to detect neutrons via their resulting gamma rays. Examples of such detectors using liquid scintillator have been successfully used in past high-energy physics (HEP) experiments. However, a liquid scintillator can leak and is not as amenable to modular or complex shapes as a solid scintillator. The light outputs and efficiencies of gadolinium-loaded polystyrene-based scintillators have been explored using a wide variety of gadolinium compounds with varying concentrations. Collection strategies using a wavelength shifting (WLS) fiber and silicon photomultipliers (SiPMs) were also evaluated as a possible neutron veto for an upgrade to SuperCDMS SNOLAB.

The scattering of dark matter particles off nuclei in direct detection experiments can be described in terms of a multidimensional effective field theory (EFT). A new systematic analysis technique is developed using the EFT approach and Bayesian inference methods to exploit, when possible, the energy-dependent information of the detected events, experimental efficiencies, and backgrounds. Highly dimensional likelihoods are calculated over the mass of the weakly interacting massive particle (WIMP) and multiple EFT coupling coefficients, which can then be used to set limits on these parameters

and choose models (EFT operators) that best fit the direct detection data. Expanding the parameter space beyond the standard spin-independent isoscalar cross section and WIMP mass reduces tensions between previously published experiments. Combining these experiments to form a single joint likelihood leads to stronger limits than when each experiment is considered on its own. Simulations using two nonstandard operators ($\mathcal{O}_3$ and $\mathcal{O}_8$) are used to test the proposed analysis technique in up to five dimensions and demonstrate the importance of using multiple likelihood projections when determining constraints on WIMP mass and EFT coupling coefficients. In particular, this shows that an explicit momentum dependence in dark matter scattering can be identified.

CDMSlite Run 2 was a search for Weakly Interacting Massive Particles (WIMPs) with a cryogenic 600 g Germanium detector operated deep underground. It was operated in a mode optimizing sensitivity to WIMPs of relatively low mass, 2 - 20 GeV, while sacrificing background rejection. An EFT analysis of CDMSlite Run 2 data from SuperCDMS Soudan is presented here. A binned likelihood Bayesian analysis was performed on the data, optimizing over the parameters of EFT interactions and the recoil energy spectra due to the dominant Compton scattering and tritium backgrounds. Recoil energy regions within 5σ of known activation peaks were removed from the analysis. The Bayesian evidences of the resulting likelihoods show that CDMSlite Run 2 data is entirely consistent with the background models with no EFT interaction necessary. Upper limits on the WIMP mass and coupling coefficients amplitudes and phases are presented for each EFT operator.

Contents

List of Tables

List of Figures

Chapter 1

Introduction to Dark Matter

1.1 Cosmological Evidence for Dark Matter

Dark matter, first recognized by astrophysicists in the 1920s and 1930s to explain gravitational effects in galactic dynamics [1–3], makes up about 80% of matter in the Universe. Astrophysical evidence supports the existence of dark matter [4–6]. Other than gravitational interactions, dark matter should interact with baryonic matter on the scale of the weak force [7–9], which makes detection accessible to experiments sensitive to nuclear scattering from a variety of targets. Investigations into dark matter may help complete the standard model of particle physics and explain large-scale structure evolution.

The effects of dark matter can be seen in the rotational curves of spiral galaxies and in the velocity dispersion of elliptical galaxies. Based on the visible matter in a spiral galaxy, the shape of the rotational curve is expected to fall off as the density drops at larger radii. However, if a large, diffuse cloud of constant density were present within and surrounding the galaxy, the rotational curve would stay flat out to larger distances. This second possibility is what has been measured for spiral galaxies, confirming the presence of the dark matter halo [10, 11]. Figure 1.1a shows the measured rotational curve for spiral galaxy M33 compared to the contribution from the luminous (stars and gas) matter and the dark matter halo. The corresponding density distribution contributions for each component is shown in Figure 1.1b. The dark matter density is represented by the Navarro-Frank-White distribution with a central density of $(1.00 \pm$

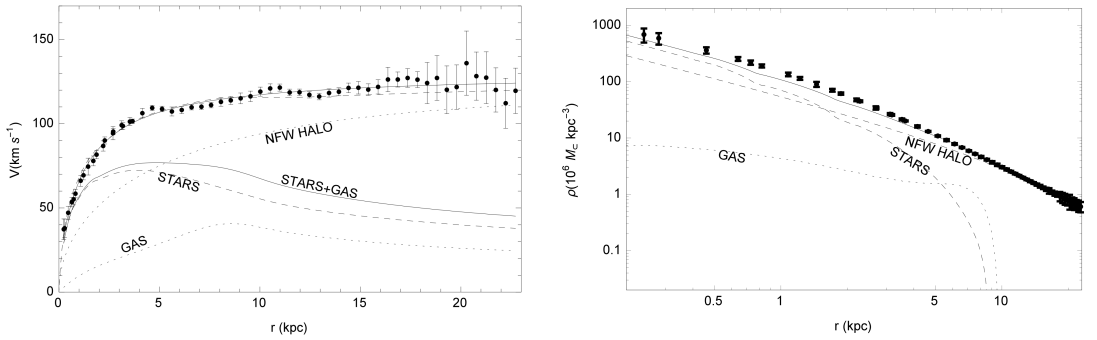

(a) M33 velocity rotational curve

(b) M33 density distribution

Figure 1.1: Comparison of the measured rotational curve (points) with the analytical best fits (solid and dashed with no labels) to the contributions from luminous matter (labeled STARS and GAS) and the dark matter halo (labeled NFW HALO) (left). Resulting density distribution for each component (right). Figures from [10].

$0.18) \times 10^{14}$ GeV/km^3 or $(12.3 \pm 1.0) \times 10^6$ $M_\odot$/kpc^3 and scale radius of 9.6 ± 0.5 kpc [10].

The existence of dark matter has also been confirmed through comparisons of the luminous to gravitational masses of galaxy clusters. The gravitational mass of a galaxy or galaxy cluster can be measured from gravitational lensing, the velocity dispersion, and measured x-ray emissions. Gravitational lensing is the effect of the gravitational field of a foreground galaxy cluster distorting the image of a more distant object. The strength of the distortion or sheer, an example of which is shown in Figure 1.2a, is proportional to the gravitational mass of the foreground galaxy cluster and the relative distances between the two objects. In many cases the sheer is greater than expected by the amount of visible mass. This discrepancy is attributed to the presence of a dark matter halo around the galaxy cluster [5, 12]. A weak gravitational lensing study of 22 galaxies using the Hubble Space Telescope (HST) found that $27 \pm 4\%$ of the mass within the star-dominated central region of the galaxies consisted of dark matter [14]. Figure 1.2b shows an example of a comparison between the gravitational and luminous mass.

Big bang nucleosynthesis (BBN) gives estimates of the mass density for baryonic and total matter in the universe by comparing the rate of weak interactions, Γ to the expansion rate of the very early universe. The universe started in a very hot and

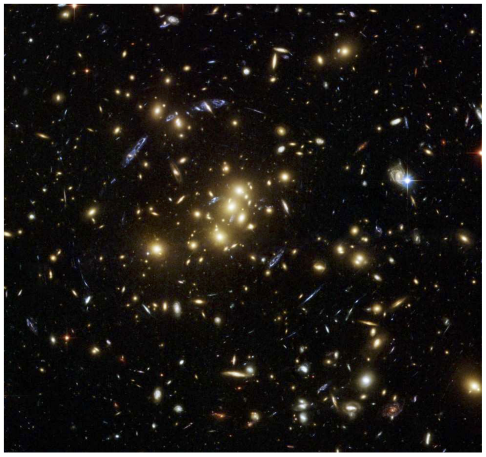

(a) Strong lensing. Figure from [12].

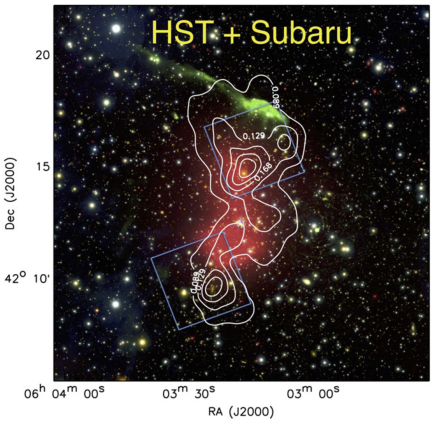

(b) Gravitational and luminous mass comparison. Figure from [13].

Figure 1.2: Examples of gravitational lensing. Left: The sheer caused from gravitational lensing around galaxy cluster CL0024+17 is visible in tangental arc shapes of the blue elongated galaxies behind the yellow elliptical galaxies of the cluster appearing [12]. Right: Comparison of the gravitational mass reconstructed from lensing (white contours) to the luminous mass as detected in radio by the GMRT, x-ray by Chandra, and optical by Subaru/Suprime Cam and HST for merging galaxy cluster RX J0603.3+4214 [13].

dense plasma in thermal equilibrium. As the universe expanded, the plasma cooled and protons and neutrons decoupled from thermal equilibrium after the rate of weak interactions became less than the Hubble expansion rate, H. At around a temperature of 1 MeV, protons and neutrons fell out of thermal equilibrium leading to the formation of ^{4}He and ^{2}H as well as ^{3}He and ^{7}Li [7]. Estimates of the total baryonic mass density, Ω_b can be made from measurements of the current abundances of these isotopes. The total baryonic mass density is dependent on the the assumptions made about the Hubble constant but can be bounded from above as $\Omega_b \leq 0.10$ [15]. The difference between the baryonic density and the total density of matter ($\Omega_b < \Omega_m$) implies the existence of a non-baryonic component to dark matter [16]. Like baryonic matter, assuming dark matter self-annihilates into quark pairs via the weak force, the final abundance of dark

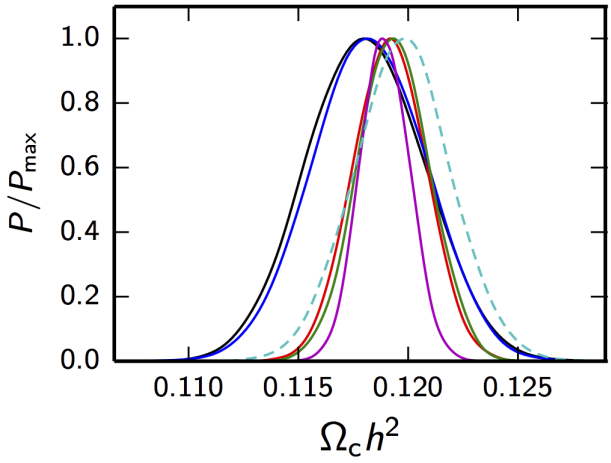

Figure 1.3: Marginalized limits of the dark matter density, $\Omega_\chi h^2$, from Planck measurements of the CMB. Figure from [4].

matter can be calculated [7]. The freeze-out condition for dark matter is

$$\Gamma_\chi = n_\chi \langle \sigma_A v \rangle = H, \tag{1.1}$$

where n_χ is the number density of dark matter and is related to the current entropy density of the universe, and $\langle \sigma_A v \rangle$ is the annihilation cross-section. Therefore, the final mass density of dark matter is

$$\Omega_\chi h^2 = \frac{3 \times 10^{-27}}{\langle \sigma_A v \rangle} \text{ cm}^2 \text{ s}^{-1} \tag{1.2}$$

and is still dependent on the annihilation cross-section. As the annihilation cross-section increases, the dark matter mass density decreases [8].

As the universe cooled, photons decoupled. This radiation left-over from the Big Bang is known as the cosmic microwave background (CMB) [7]. Measurements of the CMB anisotropy map the density distribution of dark matter at the time of photon decoupling. The structure information in the high-redshift universe complements the calculations of dark matter structure from weak lensing experiments [17]. Recently, Plank published the results of a multidimensional likelihood analysis of CMB data giving $\Omega_\chi h^2 = 0.1198 \pm 0.0015$. There were a total of 10 ΛCDM cosmological parameters in

this likelihood including the Hubble constant, H_0, the reionization optical depth, τ, and the baryon mass density $\Omega_b h^2$. Figure 1.3 shows the marginalized likelihood for $\Omega_\chi h^2$ for different combinations of CMB polarization measurements, lensing measurements, and baryon acoustic oscillation measurements. [4] These Planck results are in good agreement with previous WMAP measurements [18].

Data from these sources support the idea that a non-baryonic component of dark matter exists, which suggests the possibility that the current standard model is incomplete. The dark matter particle is expected to a neutral, massive, and stable. Baryonic candidates for dark matter exist (brown dwarfs, neutron starts, ect.) [19] but cannot make up the entirety of dark matter [20, 21]. The prime candidate for a non-baryonic cold dark matter particle is the weakly interacting massive particle (WIMP) [8], but other candidates, such as the axion [22, 23], have been suggested as well. Neutrinos have been considered as a hot dark matter particle candidate; however, due to N-body simulations that state that hot dark matter cannot clump until cooled to non-relativistic velocities, they can't explain the current large-scale structure of the universe [24].

A WIMP is naturally predicted by supersymmetric theories of particle physics as the lightest supersymmetric particle, which is often the neutralino, a linear combination of the supersymmetric partners of the photon, Z^0, and Higgs bosons [8]. The neutralino is stable if R-parity invariance is required. R-parity, which relates to lepton number, baryon number, and spin, gives R = 1 (R = -1) for standard model (supersymmetric) particles [8, 16]. The neutralino is expected to have spin $S_\chi = \frac{1}{2}$ [25], while extra dimension models predict dark matter with spin $S_\chi = 1$ [26] and electroweak symmetry breaking models predict spin $S_\chi = 1$ or $S_\chi = 0$ [27, 28]. The neutralino would interact with a strength characteristic of the weak force. This makes the neutralino a possible dark matter candidate, because an annihilation cross-section on the scale of the weak force is necessary to recreate the relic abundance of dark matter [8, 9].

1.2 Indirect Detection of Dark Matter

Theories of WIMP annihilations make it possible to search for indirect evidence of WIMPs. Pair-annihilations elsewhere in the universe are expected to produce neutrinos [29–32], γ-rays [33–37], and antimatter [25, 38, 39] that can be detected by experiments and telescopes on earth and in near-Earth orbit. These experiments attempt to calculate or set limits on the velocity-dependent annihilation cross-section, $< \sigma_A v >$, by integrating over the dark matter velocity distribution [25, 29, 33, 38]; however, these results can also make estimations on the cross-section between dark matter and target nucleons as well [36].

VERITAS [33], HESS [34, 35], and the Fermi Large Area Telescope (LAT) [36, 37] look for γ-rays from the Galactic center, dwarf galaxies, and galaxy clusters for signatures of the WIMP-WIMP annihilation. If dark matter annihilation results in secondary particles, then the γ-ray spectrum would be continuous across many orders of magnitude, similar to the background of astrophysical sources. Even though it is loop-suppressed, dark matter could also annihilate directly into $\gamma\gamma/\gamma Z$ with a sharp spectral line at $E_\gamma \approx m_\chi$ or into a γ-particle pair with $E_\gamma \approx m_\chi/2$ [34]. VERITAS uses ground based Cherenkov telescopes to detect gammas from 100 GeV to 10 TeV through the Cherenkov radiation from the secondary shower of particles of a gamma in the Earth's upper atmosphere [33]. HESS uses a four telescope array similarly to VERTAS [35] but also attempted to search for the very high energy γ-rays associated with the loop-suppressed channels [34]. The Fermi LAT is a space telescope launched in 2008 designed to detect γ-rays from 20 MeV to over 300 GeV [37].

Neutrinos are also expected as products from WIMP annihilations. When dark matter is captured by the Sun, self-annihilations can cause an increase in high-energy neutrino flux that can be measured [30] by neutrino telescopes like Super-Kamiokande (Super-K) [31], IceCube [29], and ANTARES [32]. Depending on how dark matter is assumed to interact in the sun, neutrino detectors can set limits on both spin-dependent and spin-independent WIMP interactions [30, 31]. IceCube, located at the South Pole, detects the Cherenkov light of secondary particles created when neutrinos with $E_\nu \sim$ 100s GeV travel through the ice and nearby bedrock. This experiment focuses on a mass range of 300 GeV to 100 TeV [29]. Super-K, a water-based Cherenkov detector

in Japan, focuses on lower mass WIMPs ($m_\chi < 100$ GeV) due to its lower energy threshold [31]. The undersea neutrino telescope, ANTARES, detects Cherenkov light in the Mediterranean Sea off the coast of France. ANTARES can detect WIMPS between 50 GeV and 1 TeV, although sensitivity is lost below 100 GeV [32].

Another expected byproduct of dark matter pair-annihilation is an increased anti-matter flux from annihilations into quark-pairs. The ballon-based BESS-PolarII, located in Antarctica, measures the antiproton flux. BESS-PolarII is sensitive to WIMP masses up to 200 GeV [38, 39]. The satellite-based PAMELA measures the positron flux due to cold dark matter annihilations in the galactic halo for WIMP masses up to 1 TeV. Because the shape of the spectrum is expected to be different depending on the value of the WIMP spin ($s_\chi = 0, \frac{1}{2}, 1$), PAMELA should be able to determine which spin is correct [25].

1.3 Direct Detection of Dark Matter

If dark matter is in the form of weakly interacting massive particles (WIMPs) and interacts with baryonic matter on the scale of the weak interaction, it could be accessible to direct detection experiments sensitive to nuclear scattering from a variety of targets. The nuclear recoil energy is quite small and is expected to occur within the range of 1 to 100 keV for a WIMP mass range of 10 to 1000 GeV [40] using natural units with $c = \hbar = 1$. The simplest form of the differential rate is given by

$$\frac{dR}{dE_R} = \frac{\rho_\chi}{m_T m_\chi} \int_{v_{\min}}^{\infty} v f(\vec{v}) \frac{d\sigma}{dE_R} d^3\vec{v}, \tag{1.3}$$

where E_R is the nuclear recoil energy, ρ_χ is the expected local dark matter density, m_T is the target nuclear mass, m_χ is the WIMP mass, $f(v)$ is the velocity distribution of the dark matter halo, and $d\sigma/dE_R$ is the differential cross section for the target-WIMP interaction [41]. The minimum velocity, which is determined from nonrelativistic scattering in the center-of-mass frame, is related to the nuclear recoil energy by

$$v_{\min} = \sqrt{\frac{m_N E_R}{2\mu^2}}, \tag{1.4}$$

where μ is the reduced mass of the system, and m_N is the mass of the neutron.

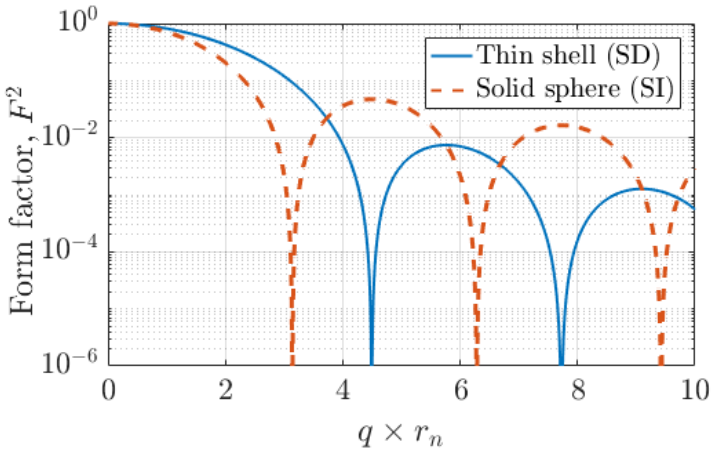

Figure 1.4: The thin-shell approximation for the spin-dependent form factor from Equation 1.7 (solid blue line) compared to the solid-sphere approximation for the spin-independent form factor from Equation 1.6 (dashed orange line).

The non-relativistic limit is considered valid for direct cold dark matter detection. The generally accepted velocity distribution for the dark matter halo is Maxwell-Boltzmann shifted by the Earth's velocity, $v_E \sim 232$ km/s, and with the width determined by the mean velocity of the particles in the dark matter halo encompassing the galaxy, $v_0 = 220$ km/s. The probability of finding a dark matter particle with a velocity greater than the galactic escape velocity, $v_{\text{esc}} = 544$ km/s, is roughly zero [40]. This is introduced through a cutoff to the Maxwell-Boltzmann distribution [42, 43], giving the velocity distribution function of

$$f(\vec{v}) \propto e^{-(\vec{v}+\vec{v}_E)^2/v_0^2} - e^{-v_{\text{esc}}^2/v_0^2}. \tag{1.5}$$

Realistically, the simple differential rate calculation is complicated by the details of the experimental set up. Detectors have some lowest detectable recoil energy threshold set by the detector sensitivity, resolution, and noise of the electronics and data acquisition instruments. There is also an energy-dependent detector efficiency that effects the shape of the expected differential event rate. Depending on the target material, there is a form-factor correction due to the shape and size of the target and the type of interaction [40].

The two most widely accepted standard interaction types are a spin-independent

interaction and a spin-dependent interaction. In this view, the differential cross-section would have a component from each interaction which can be calculated from their expected form-factors. The from-factors are commonly approximated as the Fourier transform of the target nuclear density distributions. For the spin-independent interaction, the nucleus is assumed to be a solid sphere, meaning the WIMP and target interact with the whole nucleus. The solid-sphere approximation gives a form factor of

$$F(q) = 3\frac{\sin(qr_n) - qr_n\cos(qr_n)}{(qr_n)^3}, \tag{1.6}$$

where q is the momentum transfer and r_n is a measure of the nuclear radius. The spin-dependent interaction is approximated by a thin shell and only considers contributions from unpaired nucleons. The spin-dependent form-factor is

$$F(q) = \frac{\sin(qr_n)}{qr_n}. \tag{1.7}$$

The solid-sphere and thin-shell form factors are shown in Figure 1.4.

Once a theoretical model has been determined, it must be compared to data in order to determine bounds or an upper limit on the coupling coefficients or interaction cross-sections. The comparison should take into account known or unknown sources of background in the experiment [44]. One current technique to set these limits when very few events have been detected is called the Optimum Interval method developed by Steve Yellin [45].

The Optimum Interval method is an extension of the Maximum Gap method. For a given differential event rate, dR/dE_R, and only one coupling, the cross-section, σ, can be seen as an overall normalization factor. The shape of the distribution of the differential event rate is decided by the assumed WIMP mass and velocity distribution. The goal of the Maximum Gap method is to determine the upper limit on the cross-section based on the energy distribution of the detected events. This method finds the largest energy gap between detected events and compares it to the the theoretical number of events that should have been seen in that gap. This method allows for an unknown (non-negative) background to be present in the data. By choosing the maximum energy gap as the comparison range, this method becomes less sensitive to this unknown background, but because this background may be present, only an upper limit on cross-section is possible.

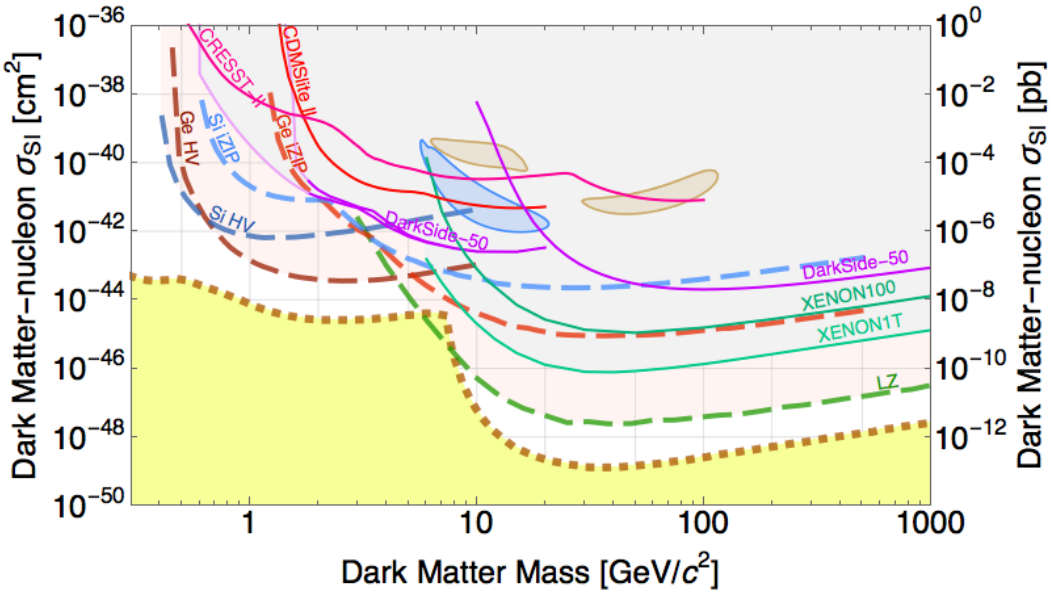

Figure 1.5: Comparison of the projected [46, 47] (dashed lines) and measured [48–54] (solid lines) upper limits on the spin-independent WIMP-nucleon interaction cross sections for many of the direct dark matter experiments shown over the limiting background from neutrino scattering [55]. Detection contours from CDMS II Si [56] (blue) and DAMA/LIBRA [57] (brown) are shown as well.

This upper limit is determined using the equation

$$C_0(x, N) = \sum_{k=0}^{m} \frac{(kx - N)^k e^{-kx}}{k!} \left(1 + \frac{k}{N - kx}\right), \tag{1.8}$$

where C_0 is the confidence of the upper limit, N is the expected number of events in the maximum gap given σ, x is the size of the maximum gap, and m is the largest integer that is less than or equal to N/x. Usually, $C_0 = 90\%$, so for this confidence and the size of the experimental maximum gap, the maximum expected number of events, and therefore cross-section, can be determined. The Optimum Interval extends this method for a greater density of events by allowing the "maximum gap" intervals to contain some number of events less than the number in the maximum possible interval. The confidence of the upper limit now depends on the events in the maximum interval [45].

The energy deposited by this nuclear recoil can be observed in the form of some

combination of complementary signals of ionization, scintillation, and phonon emission depending on the target material chosen which allows for discrimination between nuclear recoil and background electron recoil events. There are many direct detection technologies and a variety of targets. Examples include noble liquids (argon, xenon, and neon), cryogenic semiconducting crystal detectors (germanium, silicon, calcium tungstate), scintillating crystal arrays (NaI, CsI), and superheated bubble chambers using a variety of fluorinated hydrocarbons. Specifics of detector sensitivity and noise determine a detector-dependent recoil energy threshold, and the discrimination afforded by complementary signals affects background discrimination [40]. A comparison of the projected and measured limits on WIMP-nucleon interaction cross section for a variety of direct dark matter experiments is shown in Figure 1.5.

1.3.1 Cryogenic Liquid Detectors

Cryogenic noble liquid direct dark matter detectors are typically xenon- or argon-based dual-phased time-projection chambers (TPC). The cryostat holds a lower liquid stage and gaseous stage on top. An interaction in the target material produces a prompt scintillation signal (S1) which is detected by arrays of PMTs surrounding the liquid bath and an ionization signal. The electrons emitted in the ionization signal are pulled by an electric field into the gaseous phase where they produce a second scintillation (S2). The prompt scintillation signal is used to determine the energy of the recoil event, and the ratio between the scintillation and ionization signals ($S2/S1$) is used to discriminate between nuclear and electronic recoil [58]. The TPC can also be used to reconstruct a three-dimensional location coordinate for the interaction. This allows for a fiducial volume cut by taking advantage of self-shielding techniques [53].

XENON currently uses a 2000 kg liquid xenon target located at the Gran Sasso National Laboratory (LNGS) in Italy [44, 50] and LUX a 250 kg liquid xenon target located at the Sanford Underground Research Facility in South Dakota [58, 59]. As shown in Figure 1.5, XENON currently has the best limit on cross section for high mass WIMPs [50], although LUX has a very similar limit as well [59]. Xenon is a good target material for spin-independent interactions due to its high mass and good for spin-dependent interactions due to the unpaired neutron in ^{129}Xe and ^{131}Xe [58]. DarkSide uses a 50 kg liquid argon target and is located at LNGS [53, 60, 61].

1.3.2 Scintillation-only Detectors

Scintillation-only detectors, such as DAMA/LIBRA or its predecessor DAMA/NaI, search for WIMP signals through annual modulation of the nuclear recoil spectrum from scintillation detection only. As the Earth travels through the WIMP halo of the Milky Way, the strength of the nuclear recoil signal due to WIMPS should change with a period of one year. The maximum modulation is expected on June 2 and the minimum on December 2. DAMA/LIBRA uses radio-pure thallium-doped NaI targets [58]. The observed annual modulation signal from DAMA corresponds to a WIMP mass around 10 GeV and cross-section around 2×10^{-40} cm^2. However, as shown in Figure 1.5, this region has been excluded by upper limits set by other direct dark matter experiments including SuperCDMS and LUX [57, 62]. Recently, new experiments using NaI are being developed in order to test the DAMA/LIBRA detection. These include SABRE, which will have detectors in both LNGS and in Australia [63], DM-Ice at the geographic South Pole and the Boulby Underground Laboratory [64], and ANAIS at the Canfranc Underground Laboratory [65].

1.3.3 Superheated Bubble Chambers

Superheated bubble chambers look for bubble nucleations that occur when a particle enters a superheated liquid. These bubbles are observed photographically and through acoustic and pressure measurements. The energy of the particle that caused the bubble to form cannot be directly measured; however, the energy threshold of the bubble-formation can change with the chamber temperature. This allows some knowledge of the energy-dependence of a candidate WIMP interaction. The predominant background for a superheated bubble chamber are alphas. Background from electron recoil is easily eliminated by setting the pressure and temperature of the chamber to an appropriate setting. The alphas and other sources of background can be differentiated from a possible WIMP signal through acoustic measurements and photographic and pressure measurements looking for events outside the fiducial volume or that caused multiple bubble nucleations [44, 58].

COUPP is located at SNOLab in Sudbury, Canada and uses 4kg of CF_4I [66]. The French detecter, SIMPLE, uses C_2ClF_5 [67]. PICASSO, also located at SNOLab, uses

32 detector modules of C_4F_{10} [68]. PICO, an experiment that represents the merging of COUPP and PICASSO, uses 52 kg of C_3F_8 and is located at SNOLab [69]. Fluorine, which is present in all three superheated bubble chamber detectors, is a good target for spin-dependent interactions due to its unpaired proton. Iodine, which is present in COUPP, is a good target for spin-independent interactions because of its high mass [44].

Chapter 2

Cryogenic Dark Matter Search

2.1 SuperCDMS

CDMS uses cryogenically cooled crystals of germanium (Ge) or silicon (Si) to measure the phonon and ionization signals from a nuclear recoil due to an interaction with a dark matter particle. The most recent experiment, known as SuperCDMS Soudan included five towers of three 0.6 kg Ge crystals and was run underground at the Soudan Underground Laboratory in northern Minnesota. Each crystal is referred to as an iZIP (interleaved Z-sensitive Ionization and Phonon) detector [70]. The next iteration of CDMS will be SuperCDMS SNOLAB, which will sit roughly 2 km underground in Sudbury, ON, Canada. This run will include both 1.39 kg Ge and 0.61 kg Si crystals [46].

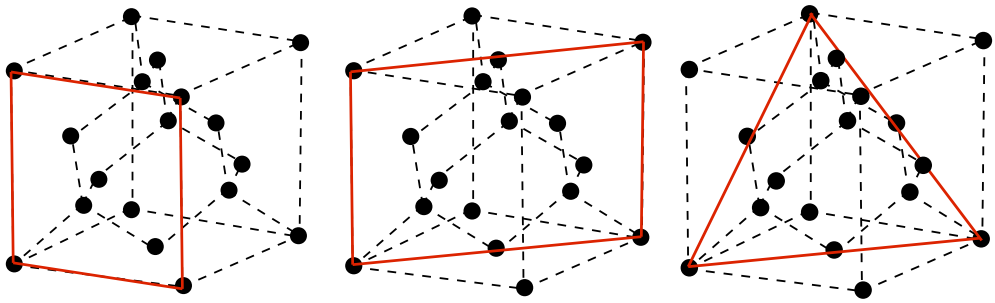

(a) [100] (b) [110] (c) [111]

Figure 2.1: Germanium structure with crystal plane designations in red.

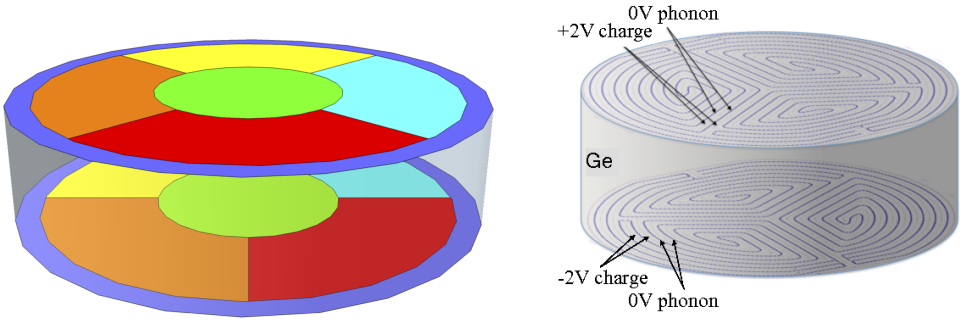

(a) One configuration of the phonon channels on the iZIPs [46] for SuperCDMS SNOLAB.

(b) Example configuration of the interleaved phonon and charge channels [71] from SuperCDMS Soudan.

Figure 2.2: Details about the SuperCDMS iZIPs.

Each iZIP detector is made out of a cylindrical germanium crystal that is 3 - 4 inches in diameter and 1 - 1.33 inches thick cut along the [100] crystal plane. Germanium is a group IV semiconductor with a diamond crystal structure. Figure 2.1 shows the [100] plane for a diamond structured crystal. Each side of the detector holds multiple charge and phonon channels. The phonon channels consist of outer guard rings and inner channels split into regions in order to aide location reconstruction. The inner channels on one side are shifted from the channels on the opposite side such that no edge along a radial line occurs at the same location on both sides of the iZIP. One possible configuration is shown in Figure 2.2a [46]. The phonon rails are grounded and interleaved with the charge rails which are held at about $+(-)2$ V for the top (bottom) of the crystal, as shown in Figure 2.2b [71]. Having anode and cathode lines on each side of the detector helps determine the location of an event and can be used to veto the background-induced interactions near the crystal surface [72].

Because a WIMP-nuclear collision is rare and low energy, the detector must be both well shielded from background sources and discriminate between unshielded background and WIMP signal events. The first layer of shielding used is the Earth itself. The experiment is operated underground because the Earth blocks cosmogenic background sources such as cosmic rays. The deeper the site, the better the shielding of these sources. SNOLab in Sudbury, Canada is almost 4000 m (water equivalent) deeper than

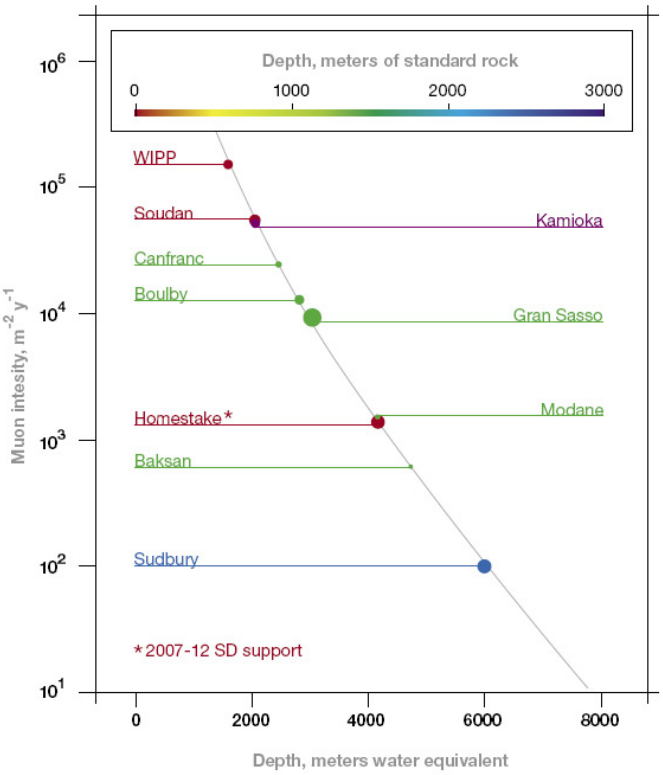

Figure 2.3: Comparison of the depth of underground physics laboratories. CDMS currently sits in the Soudan Underground Laboratory and is moving to SNOLab in Sudbury, Canada. Image from Deep Science [73].

Soudan, which cuts the intensity of the muon flux by a factor of about 10^3 [73]. A comparison of underground sites can be seen in Figure 2.3.

Figure 2.4 shows all of the shielding layers for SuperCDMS SNOLAB. The outer most layer of shielding is a water shield for blocking neutrons from the surrounding rock of the cavern. The next layers of shielding include passive gamma and neutron shields made from layers of lead and polyethylene. These shield block energy from radioactive decay in the environment of the detector [46]. The current arrangement does not shield for internal sources of radiation, so all materials used to build the detectors, detector housing, shields, and support structors must be highly radiopure [16].

A WIMP is expected to interact with the nucleus of the target material, leading to

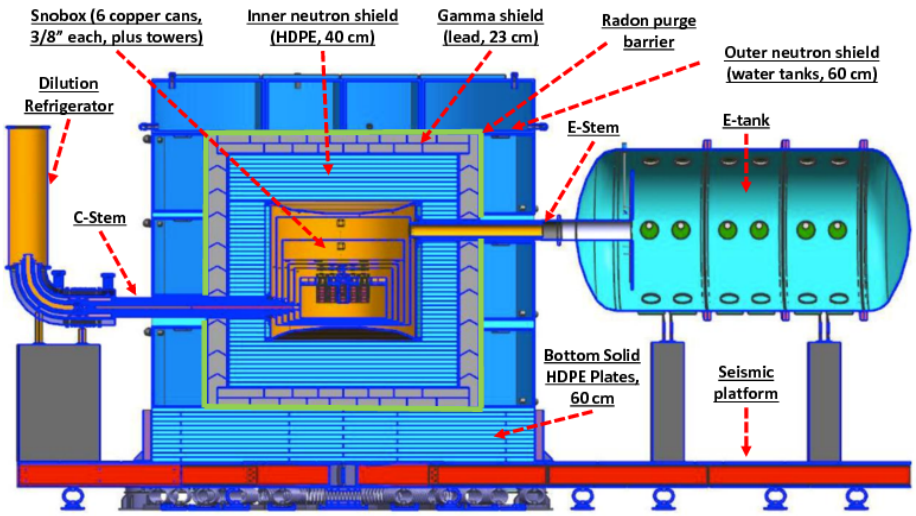

Figure 2.4: Shielding configuration for SuperCDMS SNOLAB [46]. The inner neutron shield, labeled as consisting of HDPE, could be replaced with a scintillating neutron veto.

nuclear recoil. When the nucleus is knocked out of its lattice site, it can interact with other nuclei via Rutherford scattering or nearby valence electrons. Both processes lose energy into the lattice in the form of phonons and ionization. An electron-hole pair that is created by an interaction in the detector would be accelerated in opposite directions across the detector by an applied electric field creating a cascade of more electron-hole pairs in the process [72]. The ionization signal is collected on each side of the detector on the voltage-biased charge rails and amplified by the JFET. The collected charge creates a voltage across the feedback capacitor of a JFET. The measured ionization signal is the voltage created by the reaction of the amplifier [75]. The charge readout system, including the FET (labeled HEMT), is shown on the right side of Figure 2.5.

As the electron-hole pairs are accelerated across the crystal, they lose energy via secondary, Luke phonons. The phonon signal, therefore, consists of both prompt and Luke phonons and is absorbed in superconducting aluminum fins. Quasiparticles formed in these fins are then captured by tungsten transition edge sensors (TES) that are kept at the superconducting transition edge such that as the TES heats up, the resistance

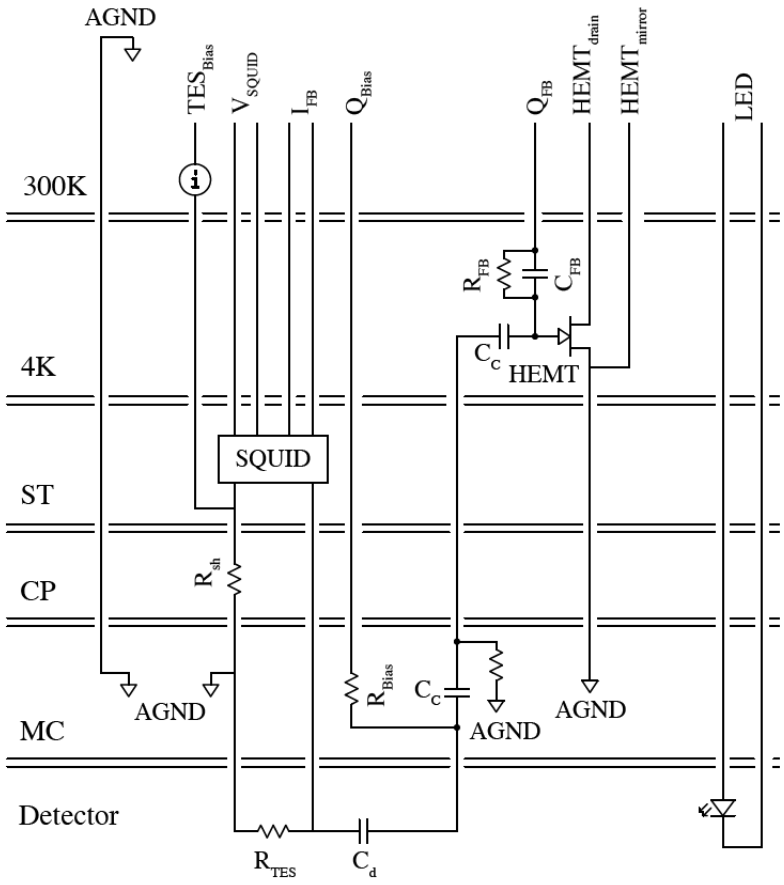

Figure 2.5: The charge and phonon readout systems designed for SuperCDMS SNOLab. Note that here the HEMT is a replacement for the current JFET of the charge readout system. Figure from [74].

of the TES increases. This increase in resistance changes the current through the input coil of the SQUID (Superconducting Quantum Interference Device), which is used for clean amplification of the signal [75]. The phonon readout system, including the SQUID and TES, is shown on the left side of Figure 2.5.

Not all of the background sources can be blocked by the shields. The most common background to reach the detectors, gammas or β-particles, come from within the shields and interact in the detectors differently than a WIMP is expected to interact. Low energy gammas interact in the detector through photoelectric absorption. High energy

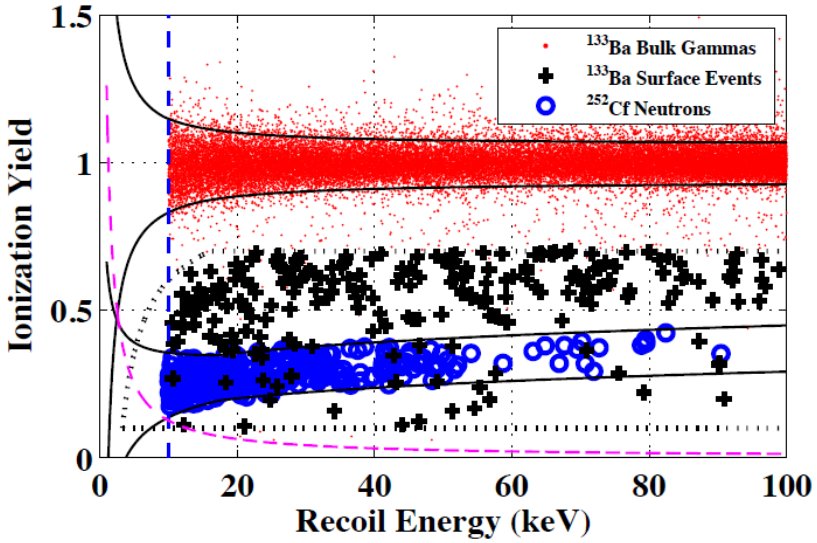

Figure 2.6: Ionization yield versus recoil energy from a CDMSII run in 2009. The electron recoil band is given by the black solid lines surrounding the red bulk gamma events. The nuclear recoil band is given by the black solid lines surrounding the blue neutron events. The surface events are shown by the black crosses to show the reduced yield near the edges of the detector. Figure from [76].

gammas Compton scatter in the detectors until they leave the system or lose enough energy to end in photoelectric absorption. Both interactions occur with valence electrons and lead to a high energy electron from which a rapid cascade leads to a high number of electron-hole pairs. The electron-hole pairs are accelerated by an electric field and lose energy via Luke phonons until the semiconductor band-gap energy is reached [72].

Beta particles interact, like gammas, with the valence electrons. However, because of their short attenuation lengths, these interactions occur near the surface of the detectors. Incomplete charge collection due to fringe electric field effects can cause reduced ionization collection compared to the detected phonon energy. These events can be discriminated from events that occur in the bulk of the detector in order to remove beta interaction from consideration. Since charge channels are on both sides of the detector and the phonon and electron rails are interleaved, the ionization signal from events that occur close to the top or bottom of the detector will mostly be collected on only one

side of the detector. Events that are detected mostly in the outer ring of the charge channels can also be vetoed as surface events [72].

The charge signal for nuclear recoils is smaller than an electron recoil for similar incident energies; however, nuclear and electron recoils of equivalent energies result in the same sized phonon signal. This is referred to as "nuclear quenching" [72]. The difference between an electronic and nuclear recoils is distinguishable in a detector by a ratio of the ionization energy to the phonon energy, known as the yield. Because both nuclear recoil events and surface beta events have reduced yield, only bulk events should be considered for analysis. An example plot of recoil energy versus yield is shown in Figure 2.6. The nuclear recoil band is clearly shown with blue circles, the electron recoils with red points, and the reduced yield of surface events with black crosses [76].

The final type of possible background is neutrons. Unfortunately, neutrons interact in the exact same way as WIMPs are expected to. Neutrons have much higher cross-sections than the WIMP, so some of the interactions from neutrons can be ignored if they scatter in more than one detector [16]. Other than looking for multiple scatters, there is currently no way to distinguish neutrons that happen to only interact once in the detectors from a candidate WIMP interaction. The plan for SuperCDMS SNOLab is to build an active neutron veto, similar to the active muon veto, within the passive shielding layers to detect internal neutrons from radioactive sources. Research and design work for a scintillating neutron veto that would replace the inner neutron shield and detect radiation from internal sources is currently in progress.

2.2 CDMSlite

When a low voltage ($\sim$ 4 V) is put across the crystal, discrimination between electron and nuclear recoil events can be accomplished by comparing the strengths of the phonon and ionization signals. If a high voltage ($\sim$ 70 V) is put across the crystal, then the secondary (Luke) phonons are greatly amplified, dwarfing the prompt phonon signal and reducing the experimental threshold to focus on low mass WIMP detection. In the high-voltage (HV) mode, the ionization signal is not measured; therefore, the nuclear and electron recoil events can not be distinguished as it is in the traditional low-voltage case. As a consequence, the background for a HV dataset includes all electron-recoil

backgrounds, with the dominant contributions including the spectral lines due to various activations and the continuous backgrounds due to tritium contamination and Compton scattering.

Running CDMS in this HV mode is known as the CDMS low ionization threshold experiment (CDMSlite) [48,70,77]. CDMSlite Run 2 ran at the Soudan Underground Laboratory in northern Minnesota in 2014. Results from this run were previously published up to 20 keV_{ee} (electron equivalent energy) or ~ 60 keV_{nr} (nuclear recoil energy) [48,77].

The energy measured when in CDMSlite mode is the total phonon energy, E_{T}, which is a sum of the prompt phonons, E_{r}, and the secondary Luke phonons. The Luke phonons are produced by electron-hole pairs drifting apart across the detector; therefore, this signal is directly proportional to the number of electron-hole pairs created, $N_{\text{e-e}^-}$. This leads to

$$E_{\text{T}} = E_{\text{r}} + eV_{\text{HV}}N_{\text{e-e}^-}, \tag{2.1}$$

where e is the fundamental charge of the electron and V_{HV} is the voltage across the crystal. The number of electron-hole pairs can be given by

$$N_{\text{e-e}^-} = \frac{E_{\text{r}}Y(E_{\text{r}})}{\epsilon}, \tag{2.2}$$

where $\epsilon = 3$ eV is the average energy of the created electron-hole pairs in Ge and $Y(E_{\text{r}})$ is the yield of the recoil at energy E_{r}. For electron recoils, $Y(E_{\text{ee}}) \equiv 1$ for all E_{ee} [70]. For nuclear recoils, $Y(E_{\text{nr}})$ is given by the Lindhard yield model,

$$Y(E_{\text{nr}}) = \frac{k \times g}{1 + k \times g}, \tag{2.3}$$

with E_{nr} in keV_{nr} and

$$g = 3x^{0.15} + 7x^{0.6} + x \tag{2.4}$$

with $x = 11.5E_{\text{nr}}Z^{-7/3}$ [78–80]. For germanium, $k = 0.157$ and $Z = 32$. The Lindhard yield model has been experimentally tested and verified by many sources using silicon and using germanium. For both crystals the experimental verification is at higher energies than the current use of the yield model [81, 82]. Figure 2.7 compares the ionization yield in silicon (Figure 2.7a) or germanium (Figure 2.7b) as determined by Lindhard model to the experimentally measured values.

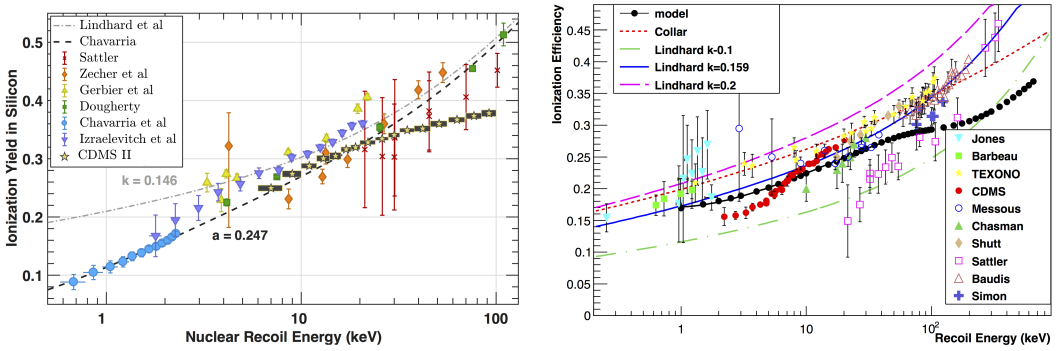

(a) Ionization yield in silicon as determined by Lindhard with $k = 0.146$ (grey dot-dashed line) compared to the experimentally measured values [81, 83–88]. Figure adapted from [81].

(b) Ionization yield in germanium as determined by Lindhard with varying k-values, including $k = 0.157$ (blue solid line), compared to experimentally measured values [89–98]. Figure from [82].

Figure 2.7: Experimental verification of the Lindhard yield model for silicon and germanium at higher energies.

.

This leads to total energy, E_{T} of

$$E_{\mathrm{T}} = E_{\mathrm{r}} \times \left(1 + \frac{eV_{\mathrm{HV}}}{\epsilon} Y(E_{\mathrm{r}})\right), \tag{2.5}$$

where the yield is as defined above for electron recoils (r = EE) or nuclear recoils (r = NR). By assuming $E_{\mathrm{T}}(\mathrm{r} = \mathrm{EE}) = E_{\mathrm{T}}(\mathrm{r} = \mathrm{NR})$, electron equivalent energy can be related to nuclear recoil energy by [70, 77]

$$E_{\mathrm{ee}} = E_{\mathrm{nr}} \times \frac{(1 + Y(E_{\mathrm{nr}}) \times eV_{\mathrm{HV}}/\epsilon)}{1 + eV_{\mathrm{HV}}/\epsilon}. \tag{2.6}$$

Chapter 3

SuperCDMS SNOLAB Neutron Veto Development

Note: Much of this chapter will be published in Poehlmann *et al.* [99].

3.1 Neutron Shielding for SuperCDMS SNOLAB

The outermost layer of shielding planned for SuperCDMS SNOLAB is a water shield that should reduce neutron interactions from the cavern environment of the detectors by 5 orders of magnitude to around 0.04 neutrons / m^2 /day [100]. This means that the major concern will be neutrons from trace contaminants in the nearest shielding layers or on the detectors themselves. For the initial payload of 4 towers, the remaining neutron background is small enough that a neutron veto is not required. However, as the payload and exposure increases, the neutron background will become more relevant. As mentioned in Section 2.1, neutron backgrounds cannot be rejected from the analysis in the way γ-rays or β-particles can. If a neutron does not scatter within multiple detectors, there is currently no way to distinguish between it and a possible WIMP event.

In order to tag single-scatter neutron events, an active neutron veto can replace the passive inner polyethylene neutron shield (refer to Figure 2.4). The plan for the active neutron veto is to include wedge-shaped sections of liquid or plastic organic scintillator. Each section of organic scintillator would have wavelength shifting (WLS) fibers

embedded in order to concentrate the light output to match the smaller readout area of a silicon photomultiplier (SiPM). The SiPMs would be cooled to -20°C to reduce the dark count rate to a few MHz. The proposed liquid scintillator cocktail is linear alkylbenzene (LAB) doped with fluorescent dyes and trimethyl borate (TMB) to increase the neutron capture cross-section. The TMB would be loaded into LAB for up to 3% boron by weight. For plastic scintillators, polystyrene would be polymerized with the necessary fluorescent dyes and would be uniformly doped with 1% wt. gadolinium.

These studies of designing an active neutron veto were guided by radioactive backgrounds simulations in GEANT4 and independent optical photon propagations simulations. The simulations suggest that active neutron shielding could provide a neutron veto efficiency of 98% against single-scatter neutrons [100]. Additional simulations show that the uniformly-doped gadolinium-loaded plastic scintillators could be replaced with layers of un-doped plastic and gadolinium resin and retain a veto efficiency of 80% [99].

Small polystyrene scintillators (20 - 50 g) were polymerized for testing and characterization. These cylindrical samples had a diameter of 2 - 2.5 cm and were machined into lengths of roughly 5 cm. Gadolinium-containing compounds can be added before the polymerization process. These small samples were used to benchmark the quality of the scintillator and determine the effect of adding gadolinium to the light output of the samples.

A quarter-scale prototype of the proposed active neutron veto was also fabricated to practice embedding WLS fibers into large-scale plastic. This prototype incorporates the SiPMs, WLS fibers, and commercial-grade scintillator from Saint-Gobain. The quarter-scale plastic prototype, shown in Figure 3.1, consists of 4 panels of scintillator, each of length 24", width, 13", and height 1.2". Each panel has four grooves machined to hold one 1.3 mm WLS fiber each. The four fibers between the same two panels were bundled together on one end to be read out by one 3 mm^2 SiPM. Further testing and optical simulations of the prototype can help optimize SiPM readout.

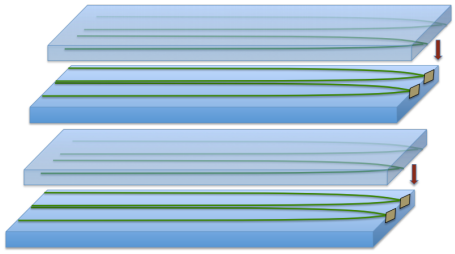

(a) Initial plan for the quarter-scale prototype.

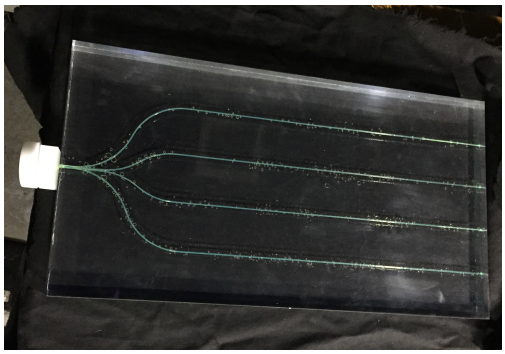

(b) One half of the fully machined quarter-scale prototype.

Figure 3.1: Quarter-scale prototype of the plastic scintillator. The prototype consists of four panels of plastic scintillator with two sets of four WLS fibers machined between two panels. The WLS fibers are bundled together at one of the plastic in order to be read out by SiPMs.

3.2 Introduction to Scintillator Physics

Organic scintillator is ubiquitous in the detection of charged particles but is less efficient as a neutron detector. Doping scintillator with a material of high neutron-capture cross-section allows neutron detection via the resulting secondary particles. Scintillators used in high-energy physics (HEP) are typically organic liquid or plastic scintillators. Plastic scintillators are made by polymerizing monomers such as styrene or vinyl toluene. The resulting plastics are relatively cheap and easy to machine into complex shapes. The liquid alternative is easier to make; however, they must be hermetically sealed to prevent leaks and contact with atmospheric oxygen [101], because dissolved oxygen will quench a light signal [102]. The dopants frequently used in liquid organic scintillators, such as trimethyl borate (TMB), are also highly dangerous and flammable. However, when dissolved into plastics, some of these more dangerous properties may be mitigated. Plastic scintillators are a good fit for HEP experiments because of the very fast decay times of their light pulses (down to ~ 5 ns) which allows for very high count rates ($\sim 10^6$ Hz) [103].

Plastic scintillators are doped with fluorescent dyes to optimize light output. The

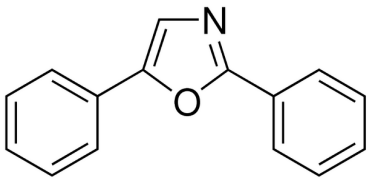

(a) PPO structure.

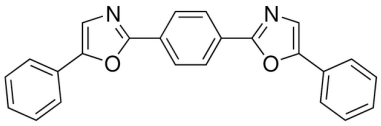

(b) POPOP structure

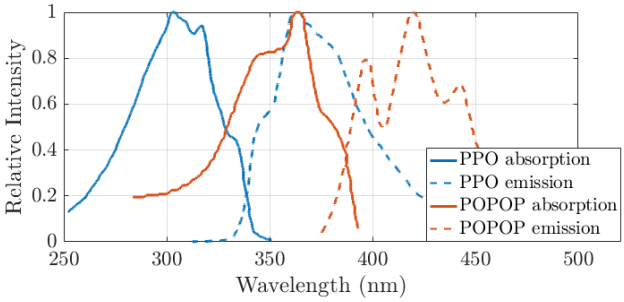

(c) Fluor absorption and emission spectra.

Figure 3.2: Chemical structures (left) and absorption and emission spectra (right) of the fluorescent dyes commonly used in organic plastic scintillators. Figures adapted from [104].

primary fluorescent dye compound is 2,5-diphenyloxazole (PPO), and the secondary dye is 5-phynyl-2-[4-(5-phenyl-1,3-oxazole-2-yl)phenyl]-1,3-oxazole (POPOP). The chemical structures are shown in Figure 3.2. The PPO acts as a pump for the POPOP [103], which fluoresces naturally with a maximum intensity at 429 nm, as shown in Figure 3.2c. Scintillation from PPO and POPOP lead to light pulses with two components. Each light pulse contains a short (prompt) and long (delayed) decay component. The prompt scintillation comes from direct radiative de-excitation of an excited POPOP singlet state (S_1), while the delayed scintillation is from the interactions between two POPOP triplet states (T_1) [105] by

$$T_1 + T_1 \rightarrow S_0 + S_1. \tag{3.1}$$

This second singlet decay (S_1) has the same spectral distribution as the original singlet decay but occurs later, but the triplet decay to S_0 is of lower energy [102]. These two time components result in a pulse shape with a double-exponential decay:

$$V(t) \propto e^{-(t-t_o)/\tau_{\text{rise}}} - a_{\text{fast}} e^{-(t-t_o)/\tau_{\text{fast}}} - a_{\text{slow}} e^{-(t-t_o)/\tau_{\text{slow}}} \tag{3.2}$$

where t_0 characterizes any time delay in the pulse, τ_{rise} is the rise-time of the pulse from the electronics of the data acquisition system, τ_{fast} is the decay-time of the prompt

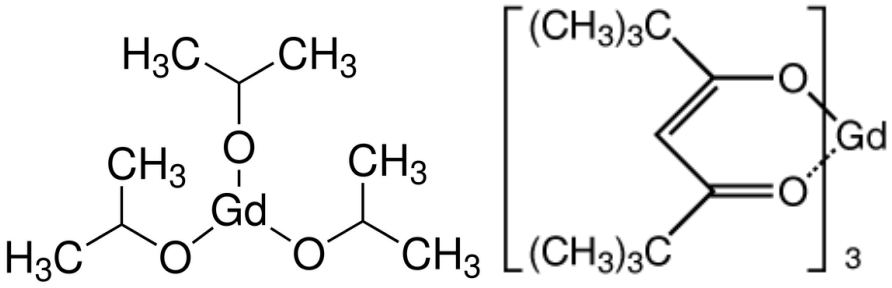

(a) Structure of Gd(i-Pr)$_3$ [108].

(b) Structure of Gd(TMHD)$_3$ [109].

Figure 3.3: Two examples of Gd-containing compounds used for increasing the thermal-neutron absorption cross-section in organic scintillators.

component of the scintillation, and τ_{slow} is the decay-time of the delayed component of the scintillation [106]. The decay times, τ_{fast} and τ_{slow}, are roughly the same for plastic scintillators unless very high concentrations of PPO and POPOP are used. When higher concentrations are used, the differences in pulse shape can be used to distinguish between neutron and γ interactions [105, 107].

In order to detect neutrons more efficiently, scintillators must be loaded with a compound with a high cross-section for thermal-neutron absorption. Compounds containing gadolinium (Gd), lithium (Li), and boron (B) are commonly used for this [101, 103, 110, 111]. Two Gd isotopes have the highest thermal neutron absorption cross-section of any naturally occurring element: ^{155}Gd (14.7% abundance) with a cross-section of 6.1 x 10^{-20} cm^2 and ^{157}Gd (15.7% abundance) with a cross-section of 2.6 x 10^{-19} cm^2 [112]. Compounds such as gadolinium isopropoxide (Gd(i-Pr)$_3$) and gadolinium 2,2,6,6-tetramethyl-3,5-heptanedione (Gd(TMHD)$_3$), whose chemical structures are both shown in Figure 3.3, are good examples of gadolinium-containing compounds that can be added to plastic scintillators to increase the thermal-neutron absorption cross-section. Interactions between thermal neutrons and gadolinium result in low energy internal conversion electrons and a cascade of Auger electrons and γ-rays. Conversion electrons are emitted from an interaction with an atom's excited nucleus, and Auger electrons are ejected after an outer-shell electron falls into an inner-shell opening [110, 111]. Additionally, atomic spectral x-rays are emitted 50% of the time.

The energy released from an interaction with a neutron is a cascade of γ-rays with a total energy of 7.8 MeV [101]. The endpoint energy for neutron capture on ^{155}Ge (^{157}Ge) is 8.5 MeV (7.9 MeV) [113].

Isotopes of Li and B have high neutron cross-sections as well. For lithium, ^{6}Li (7.5% abundance) has a cross-section of 9.4×10^{-22} cm^2, and boron, ^{10}B (20% abundance) with a cross-section of 3.853×10^{-21} cm^2 [114]. Interactions between neutrons and ^{6}Li or ^{10}B produce alpha particles with endpoint energies at 4.78 MeV or 2.79 MeV. Additionally, interactions with ^{6}Li produce tritium with an energy of 2.73 MeV and do not produce the gamma-ray emission given by interactions with ^{10}B [103]. 6% of the time, the ^{10}B interaction produces a 1.78 MeV alpha, and 94% of the time, it produces a 1.47 MeV alpha and a 477 keV gamma [115]. Gadolinium may be preferred over lithium or boron because the relevant isotopes have a neutron interaction cross-section several orders of magnitude higher and appear in higher natural abundances. Additionally, the endpoint energies of the interactions with Gd are higher than for lithium or boron.

The scintillation from plastic scintillators can be read out from photomultiplier tubes (PMTs) or from solid-state silicon photomultipliers (SiPMs). The typical gain (the ratio of detected electrons to electrons emitted by incident light) of a PMT is around 10^7 [102]. Unlike the PMT, a SiPM consists of a 2D array of PN junctions. Each junction acts as a single pixel for the whole SiPM. This 2D pixel array, shown in Figure 3.4c, has dead-space between pixels that limits the overall detection efficiency compared to a PMT. The incident light causes a voltage across a PN junction (shown in Figures 3.4a and 3.4b), which then causes a measurable current. A PN junction is an avalanche photodiode (APD) run in Geiger mode, which means the reverse bias is greater than the breakdown voltage. This results in an internal gain ($\sim10^6$) that gives it good sensitivity to low level signals. When an APD is illuminated with a photon of energy greater than the band gap energy (1.12 eV for silicon at room temperature) a valence electron is excited into the conduction band leaving an electron hole behind. As the electron is accelerated by the electric field across the depletion layer, it collides with the lattice, which excites more electrons into the conduction band.

There is a strong temperature dependence of this avalanche process. At higher temperatures, the lattice is vibrating more, which decreases the carriers released in the avalanche process. Because not all generated carriers will manifest in a measurable

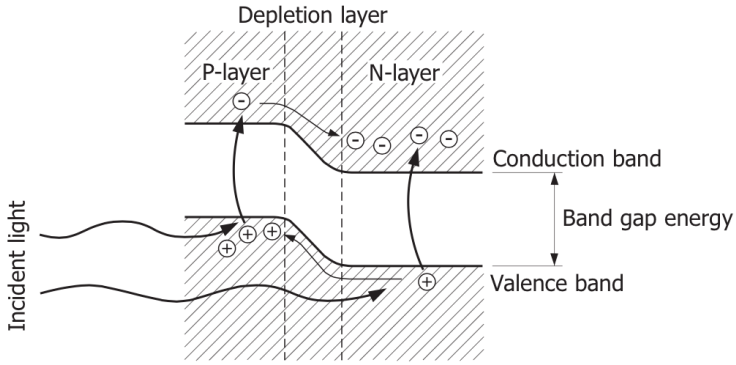

(a) PN junction in a SiPM

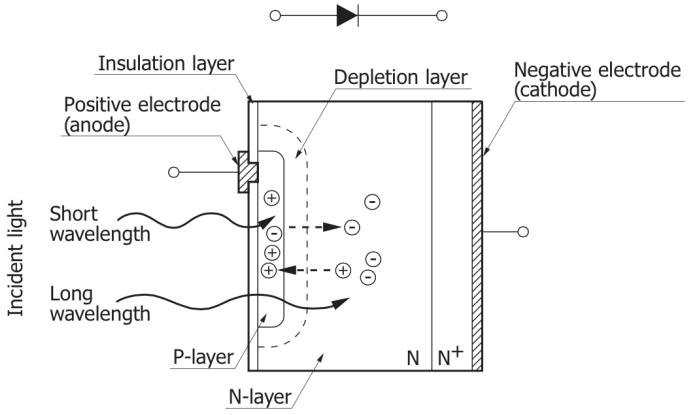

(b) SiPM cross-section

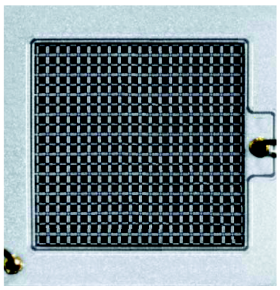

(c) Example SiPM face

Figure 3.4: Internal details of a SiPM. Figures from [116].

pulse, the photon detection efficiency is lower for an APD than for other photodiodes. Thermal excitations may also cause an avalanche process. The frequency of these "dark count" events can be reduced by operating at a lower temperature. Another side effect of running a Si APD in Geiger mode is a phenomenon called after-pulsing. An after-pulse occurs when a charge carrier from an avalanche gets trapped by a defect in the crystal structure of the silicon and is released after some time delay. This phenomenon is made worse at lower temperatures, so choosing an optimal operating temperature is a balance between quenching the avalanche process/dark counts and after-pulsing.

Both PMTs and SiPMs are able to read out low intensity pulses, but SiPMs are

more radioactively clean, which is very important for a veto that would sit within the shielding layers of SuperCDMS SNOLAB. SiPMs are also smaller and create less electronic noise, which allows for a simpler configuration within the outer CDMS shields. SiPMs also have a higher quantum efficiency, where we define quantum efficiency as the ratio between the number of photoelectrons released to the number of incident photons. For incident light with wavelength, λ, the number of incident photons, N_γ, is

$$N_\gamma = \frac{E_{\text{det}}}{hc/\lambda}, \tag{3.3}$$

where E_{det} is the energy of light incident on the cathode of the photodetector. After all stages of amplification, the number of photoelectrons released, N_{pe}, can be calculated as

$$N_{\text{pe}} = \frac{S}{G} E_{\text{det}}, \tag{3.4}$$

where, for a PMT, S is the anode responsivity and can be converted to the cathode responsivity by dividing by the gain, G. Therefore, the quantum efficiency, QE is dependent on the wavelength of the incident photon by

$$\text{QE}(\lambda) = \frac{hc}{\lambda}\frac{S}{G}. \tag{3.5}$$

A typical PMT has a quantum efficiency of around 20 - 30%. For SiPMs, there is an additional geometric efficiency due to the dead-space between pixels. This total efficiency is called the photon detection efficiency (PDE) and can be calculated by

$$\text{PDE}(\lambda) = \text{QE}(\lambda) \times f \times P_A, \tag{3.6}$$

where QE is the quantum efficiency of the SiPM, f is a measure of the effective pixel size, and P_A is the probability of an avalanche occurring. The effective pixel size takes into account dead space between pixels, shown in Figure 3.4c. A typical SiPM with a pixel size of 1 mm^2 might have a maximum PDE of around 40 - 70% [116].

3.3 Characterization of Photon Detectors

Four 1.33 mm^2 CPTA 151 SiPMs and a bialkali Hamamatsu R1332 2 inch PMT were chosen for testing and characterization. The PMT data was read out using a LeCroy

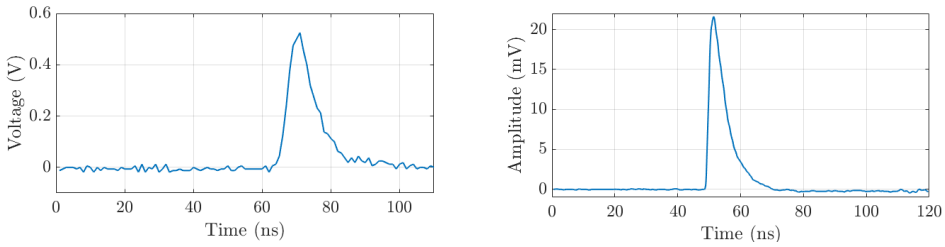

(a) Hamamatsu PMT. (b) CPTA SiPM.

Figure 3.5: Example pulses from each photo detector option used.

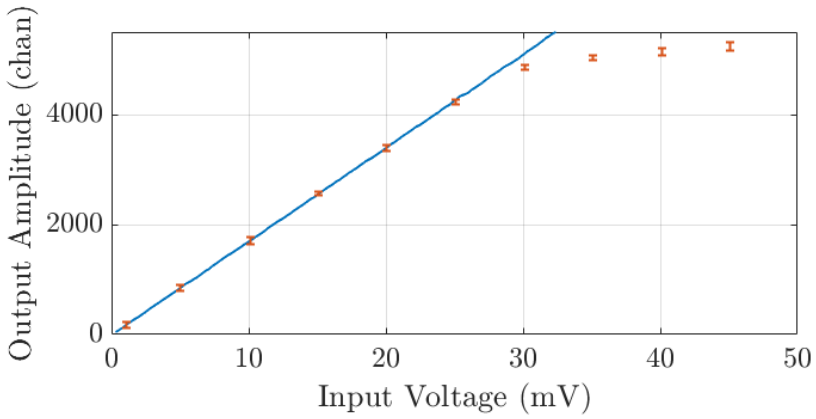

Figure 3.6: Measurement of the response of the digitizer to convert pulse amplitude from channels to mV and determine the saturation point of the digitizer. The measured points are shown in orange, and the best fit line (before the saturation point) is shown in blue.

WaveSurfer oscilloscope controlled by a LabVIEW VI. Typically the trigger for the oscilloscope was determined using an external NIM coincidence unit. An example PMT muon pulse is shown in Figure 3.5a.

The full amplitude versus time signal of each SiPM was read out by an electronics test board (TB4) built at Fermi National Laboratory [117]. The TB4 board has four SiPM channels. Each channel is read out into a computer through a digitizer that converts a pulse into a set of data points that can be processed to determine the area under each pulse. The area is a measure of the energy of the incident light. The timing of a pulse was determined from the 212.416 MHz sampling rate of the digitizer. A

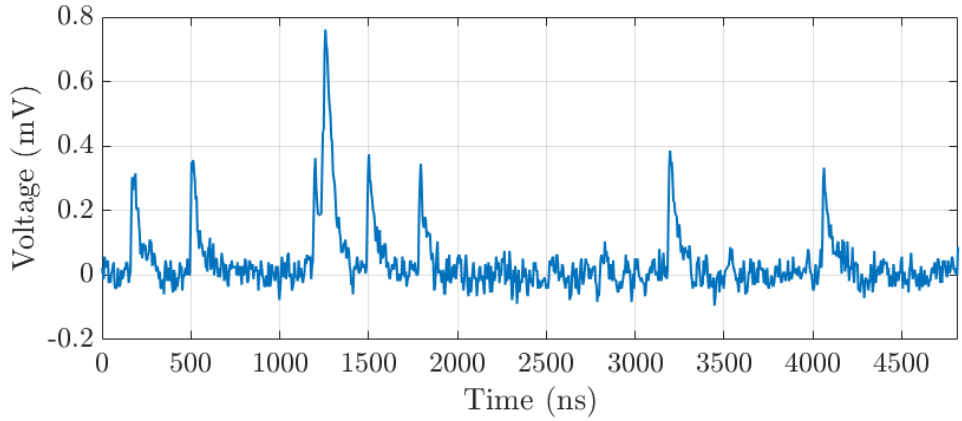

Figure 3.7: Example pulses for SiPM 4 with no light source. The calculated dark count rate for this event is 1.660 MHz.

sample SiPM light pulse is shown in Figure 3.5b.

The response of the digitizer was determined by sending square pulses of known amplitude from a signal generator into the data acquisition system in the place of a SiPM. A graph of input and output amplitudes for square pulses of varying amplitudes is shown in Figure 3.6. The digitizer has a very linear response with a slope of 169.70 ± 0.97 channels/mV up to around 30 mV. Past 30 mV, the digitizer becomes saturated. With this measurement, the amplitude of each pulse can be converted from arbitrary ADC channels to a meaningful measure of voltage, as shown in Figure 3.5b.

3.3.1 SiPM Dark Count Rate

The dark count rate of a SiPM can be measured by reading out randomly triggered pulses of a SiPM with no light source. SiPM 4 was placed in a light tight box, and random triggers with a timing window of 4821 ns each were recorded. For each time window, the number of single and double dark count pulses were counted. A single dark count pulse has a maximum amplitude above the threshold of 0.265 mV, and a double dark count pulse has a maximum amplitude greater than 0.589 mV. These thresholds could be set on either pulse area or amplitude; however, because a dark count peak can occur anywhere within the timing window, the amplitude threshold allows for a more automated analysis. An example pulse is shown in Figure 3.7. This example has six

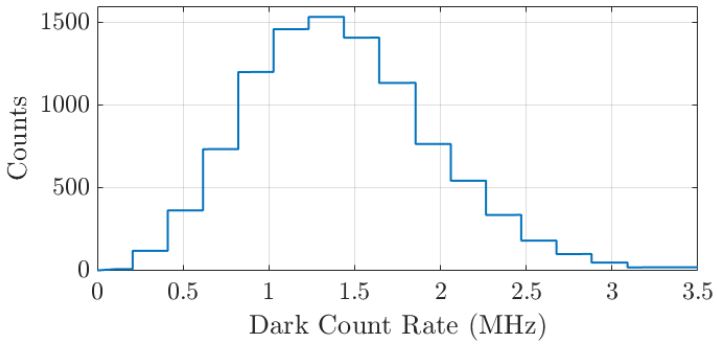

Figure 3.8: Dark count rate for SiPM 4 for all measured events.

single dark counts and one double dark counts for a total of eight dark counts in the 4821 ns window, which gives a rate of 1.660 MHz. This calculation was repeated for all random triggers. The resulting histogram is shown in Figure 3.8. From this histogram, the average dark count rate for SiPM 4 is 1.33 ± 0.52 MHz, which is, before cooling, within the target dark count rate range for SuperCDMS SNOLAB. The probability of two dark counts occurring at the same is is 5.80%.

3.3.2 Quantum Efficiency Measurements

For a PMT, the gain, which is necessary to calculate the quantum efficiency as shown in Equation 3.5, is determined by the area under a single photoelectron peak, given by

$$G = \frac{1}{eR} \int V(t)dt, \tag{3.7}$$

where $V(t)$ is the time-dependent voltage of the measured pulse, $R = 50\Omega$ is the resistance over which the signal voltage was measured, and $e = 1.602 \times 10^{-19}$ C is the fundamental charge of an electron [118]. Using a 0.5 mV trigger and a bias voltage of 1800 V, the pulse area of the single photoelectron peak was determined to be (20.3 ± 0.2) pVs for a gain of $(2.54 \pm 0.03) \times 10^6$ [99].

In order to measure the anode responsivity, the intensity output of the Hamamatsu PMT was compared to that of a calibrated photodiode using a monochromator illuminated by a white-light source. Figure 3.9a shows the setup necessary to make this measurement. Using the calculated gain and an additional correction for active detector

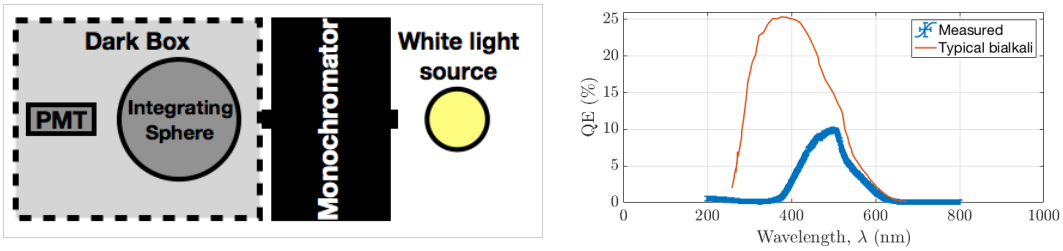

(a) Monochromator set up used for PMT quantum efficiency measurement.

(b) Measured quantum efficiency compared to a typical Hamamatsu bialkali PMT [119].

Figure 3.9: Details of the quantum efficiency measurement for the Hamamatsu PMT. Figures adapted from [99].

area, the wavelength-dependent quantum efficiency was calculated from Equation 3.5 and is shown in Figure 3.9b. The Hamamatsu PMT had a maximum quantum efficiency of $10.0 \pm 0.3\%$ at 500.0 ± 0.5 nm [99], which is lower than expected for a typical bialkali PMT.

The response of the SiPM is defined as the distance between each photoelectron peak in a very low-energy pulse-area spectra. The low-energy spectra were obtained using a blue LED flashed with a very high frequency to reduce the light output. Due to the excellent photon counting properties of the SiPM, up to eight photoelectron peaks are visible, as shown in Figure 3.10a. The pedestal is below 0.02 nVs (also labeled as the 0th photoelectron peak) with the first photoelectron peak at ∼0.03 nVs. The average distance between photoelectron peaks for SiPM 3 was determined to be 0.01972±0.00036 nVs by fitting each peak to a Gaussian function. The spacing between photoelectron peaks for the other SiPMs are shown in Table 3.1.

For a SiPM, the gain (G) can be calculated by

$$G = \frac{1}{eR} \int V(t)dt = \frac{\Delta n_{\text{pe}}}{eR}, \tag{3.8}$$

where $R = 50\Omega$ is the typical load resistance of the couplings to the digitizer, $\int V(t)dt$ is the area under a single photoelectron peak, and Δn_{pe} is the spacing between photoelectron peaks. Due to the better statistics, the average distance between photoelectron peaks in a pulse-area spectra is a better measure than the area under one peak. The calculated gain for each SiPM is shown in Table 3.1.

SiPM	Photopeak spacing (nVs)	Gain
1	0.01836±0.00018	$(2.29 \pm 0.02) \times 10^6$
2	0.01735±0.00017	$(2.16 \pm 0.02) \times 10^6$
3	0.01972±0.00036	$(2.46 \pm 0.04) \times 10^6$
4	0.01689±0.00044	$(2.11 \pm 0.06) \times 10^6$

Table 3.1: The spacing between each photoelectron peak and the calculated gain for each SiPM.

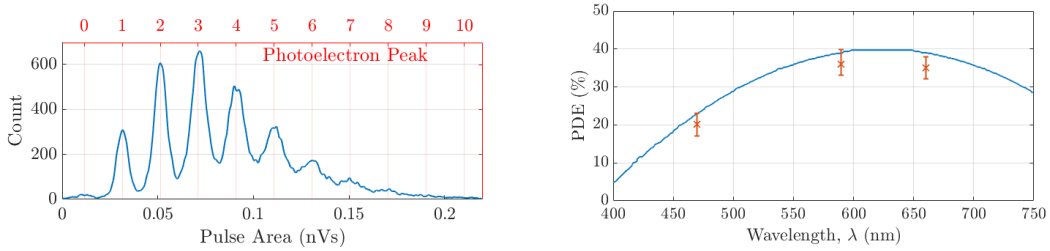

(a) Histogram of the area under each pulse for SiPM 3. The top x-axis shows the conversion to number of photoelectrons detected.

(b) Measured SiPM PDE at specific wavelengths (orange x) compared to the manufacturer's specifications (blue line) [120].

Figure 3.10: SiPM measurements used to calculate gain and PDE.

The PDE of a SiPM can be measured using the set up shown in Figure 3.9a. The PMT was replaced with a SiPM, and the white light source was replaced with an LED of a specific wavelength, because the white light source saturated the SiPM. Three LEDs were used for measurements at three specific wavelengths. Since the dark count for the SiPM is much higher than for the PMT, the measured intensities were corrected for dark count before being used for the PDE calculation. The resulting PDE measurements are shown in Figure 3.10b compared to the manufacturer's specifications.

Loading Compound	Max. Loading (%wt. Gd)	Tested	Notes
$Gd(i\text{-}Pr)_3$ [110]	5%	yes	Clear samples
$Gd(TMHD)_3$ [111]	5%	yes	Clear samples
GdB_6*	—	yes	Purple samples
$Gd(OTf)_3$*	—	yes	Orange samples
$Gd(NO_3)_3(TBP)_3$* [101]	12%	yes	Yellow samples
$Gd(PPr)_3$ [121]	8%	no	—

Table 3.2: Possible metal-containing compounds for use as high neutron cross-section dopants in plastic scintillators. The maximum loading column lists the highest loading percentage, by mass, achieved in the referenced paper. The "Tested" column refers to whether or not we polymerized a scintillator sample containing that compound, and the "Notes" column briefly describes that sample. The (*) denotes compounds trials that were discontinued due to sample discoloration.

3.4 Polymerization of Gadolinium-Loaded Plastic Scintillator Samples

3.4.1 Production Methods

Small polystyrene scintillators (20-50 g) were polymerized from styrene monomer for testing and characterization. Any compound with a high neutron cross-section can be added before the polymerization process in order to increase functionality as a neutron shield or detector. Here, the focus was on Gd-containing compounds. These dopants were added in varying weight percentages. Table 3.2 shows an overview of possible Gd-containing compounds for use as high neutron cross-section dopants.

The polymerization process roughly followed the method as described by Bell *et al.* [101] with minor changes. Before polymerization could occur, the inhibitor and other possible impurities were removed from the styrene monomer using a column of alumina. At this point, any high neutron cross-section dopant of interest was added to the purified styrene in the desired weight percentage. The styrene monomer and metallic-compound mixture was then mixed with 1% wt. PPO and 0.1% wt. POPOP.

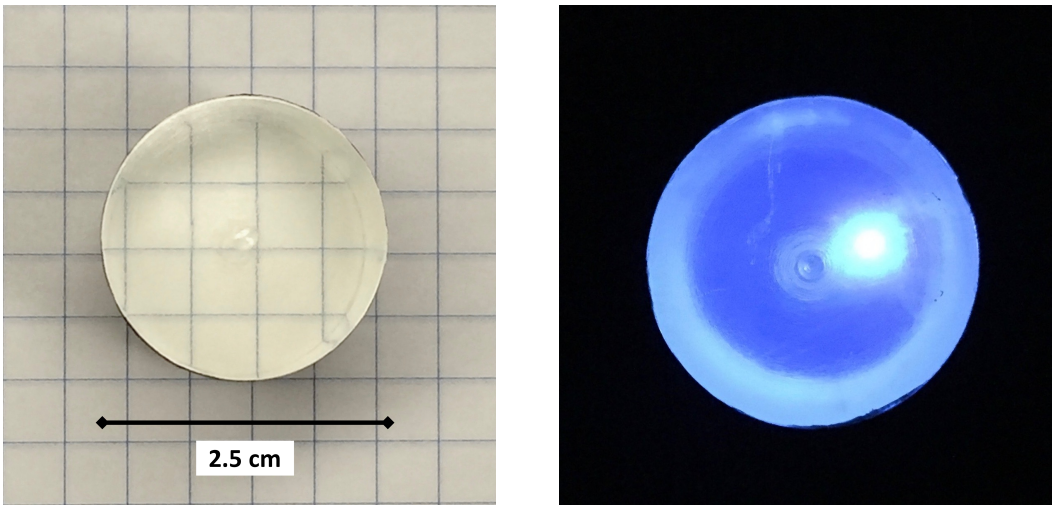

(a) Fully polymerized, machined, and polished plastic sample.

(b) Sample illuminated by UV LED.

Figure 3.11: A non-gadolinium doped plastic scintillator, after being machined and polished, is shown above (left). The outer circumference has been painted with three coats of EJ-510 reflective paint and one coat of black paint to limit light loss. The same sample is illuminated by an off-center 305 nm LED (right). Figure from [99].

Purified benzoyl peroxide (added in at 0.8% wt.) was used as a catalyst for the polymerization. Samples were sonicated for up to an hour to encourage complete dissolution. Dry nitrogen was bubbled through this mixture for at least an hour to remove water and oxygen. If water was not removed from the system completely, bubbles would form in the polystyrene during polymerization. The styrene was polymerized in a $\sim$60°C water bath for $\sim$5 days under nitrogen and slowly cooled to room temperature over the course of 12 hours. The time for each step was optimized through multiple trials. An example of a fully polymerized, machined, and polished polystyrene sample is shown in Figure 3.11a. Samples diameters were typically 2.5 cm while sample lengths ranged from 4 cm to 11 cm. One sample (unLS-WLS) had a 1.0 $\oslash$mm wavelength shifting (WLS) fiber machined down the center lengthwise.

Sample Name	Dopant	% wt. Gd	Length (cm)	Diameter (cm)
unLS	None	0%	11.10 ± 0.02	2.50 ± 0.05
unLS-WLS*	None	0%	4.50 ± 0.02	2.11 ± 0.05 (long), 1.94 ± 0.05 (short)
LS-iPr	Gd(i-Pr)$_3$	0.055%	11.10 ± 0.02	2.50 ± 0.05
LS-TMHD	Gd(TMHD)$_3$	0.055%	11.10 ± 0.02	2.50 ± 0.05

Table 3.3: A summary of the fabricated samples is shown above. The * indicates that sample unLS-WLS had a wavelength-shifting fiber embedded down the center of the sample. Pictures of these samples can be found in Figure 3.12.

3.4.2 Gadolinium Loading Attempts

For the scintillators fabricated following the procedure described in Section 3.4.1, maximum loadings of 0.15% wt. using Gd(i-Pr)$_3$ and 0.25% wt. using Gd(TMHD)$_3$ were achieved, which are both significantly less than expected from previous publications [110, 111]. Additional heating and sonication prior to and throughout the polymerization process did not improve the solubility of either compound but instead decreased the transparency of the resulting scintillator. While not explicitly mentioned, Bertrand *et al.* [111] added an unspecified polar co-monomer at 20-25% wt. of the total monomer. It was hypothesized by Bertrand *et al.* that partial ligand exchange or completion of the Gd coordination sphere with the polar co-monomers allowed for higher concentrations to be reached. However, the specific co-monomer used for Gd(TMHD)$_3$ is not known, as it is considered to be a trade secret.[1]

Gadolinium-loaded plastic samples were fabricated by loading Gd(i-Pr)$_3$ or Gd(TMHD)$_3$ at the highest possible concentrations, such that the metal dopant was fully dissolved to the same mass percentage for both compounds. This resulted in much lower concentrations than if co-monomers had been used. Information about each fabricated sample along with loading compound and concentration are listed in Table 3.3 and a picture of each sample is shown in Figure 3.12. In early trials with Gd(i-Pr)$_3$, cloudy samples were observed. This was linked to impurities in the metallic compound that resulted in a white, wispy precipitate that could be filtered out of the styrene-metal

[1] 2017/01/24: email communication with Guillaume Bertrand, Guillaume.BERTRAND@cea.fr

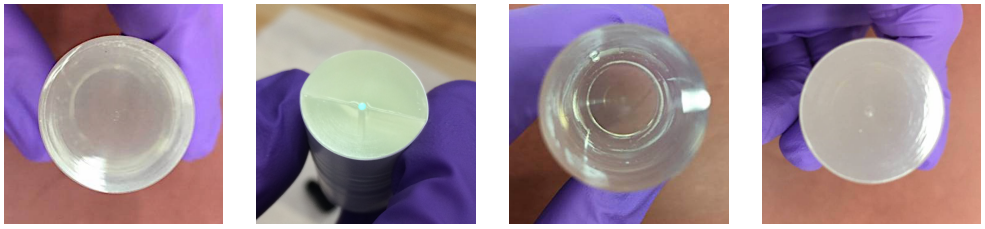

(a) unLS (b) unLS-WLS (c) LS-iPr (d) LS-TMHD

Figure 3.12: The samples listed in Table 3.3 are shown above. The samples unLS, LS-iPr, and LS-TMHD were unwrapped when photographed. Sample unLS-WLS was wrapped with PTFE tape when photographed. The WLS fiber embedded down the center of unLS-WLS is visible in green.

dopant solution before polymerization. The mass of precipitate recovered was smaller than the uncertainty in the balance used to measure the doping compound, suggesting that any Gd lost had a negligible effect on the calculated Gd concentration. Elemental analysis of this precipitate using energy dispersive spectroscopy on a scanning electron microscope showed its composition was inconsistent with that of Gd(i-Pr)$_3$ and instead one of the oxides of gadolinium, most likely Gd_2O_3. Thus, the white wispy precipitate was not undissolved Gd(i-Pr)$_3$ but rather impurities within the dopant.[2] When loading polystyrene with Gd(TMHD)$_3$, the compound appeared to have dissolved fully at concentrations up to 0.5% wt. Gd after 1 hour of sonication. However, the gadolinium compound precipitated out of the styrene monomer during the polymerization process when loaded at concentrations greater than 0.25% wt. Gd(TMHD)$_3$.

Instead of exploring various co-monomers to use with Gd(i-Pr)$_3$ or Gd(TMHD)$_3$, tests were made to overload samples with these Gd-containing compounds in order to increase the concentration of Gd past the solubility point of the compound. The hope was that the un-desolved gadolinium would settle into gradient layers of increasing concentration. Simulations of a neutron veto using layers of gadolinium and plastic scintillator instead of a uniformly doped veto at 1% wt. Gd showed that for a veto with 40 - 200 segments, veto efficiency ranges from 75% to 85% compared to the 90% efficiency of the uniformly doped option [99]. Because1% wt. Gd loading is not possible without

[2] SEM data was obtained and interpretated by Dr. Nick Seaton, SEM & LM Specialist of the Characterization Facility at the University of Minnesota.

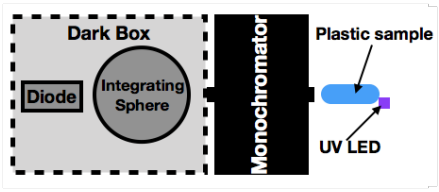

(a) Setup used to obtain emission spectra.

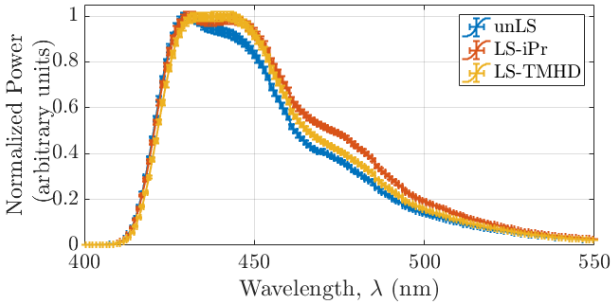

(b) Resulting emission spectra normalized to the highest peak.

Figure 3.13: Each sample was wrapped with PTFE tape and illuminated by an off-center 305 nm surface-mounted LED and centered on the input slit of the monochromator. A calibrated photodiode was used to measure the output power of the monochromator as a function of wavelength. Figures adapted from [99].

use of a co-polymer, the overloading technique would combine a uniformly doped veto (with less than 1% wt. Gd) with the layers of more highly-concentrated overloaded Gd in order to improve the overall efficiency of neutron detection. Unfortunately, the ability of these samples to fully polymerize was compromised by the increased amount of Gd-containing compound. The samples tested ended up only partially polymerizing, and even the most promising attempts ended up too soft to machine or polish.

3.5 Characterization of Plastic Scintillator Samples

3.5.1 Emission Spectra

A monochromator was used to determine the effect of dissolving Gd in polystyrene on the relative light output and peak emission wavelengths of the scintillator samples. Each scintillator sample was centered on the input slit of the monochromator and illuminated by an off-centered 305 nm surface-mounted LED, as shown in Figure 3.11b. Figure 3.13a shows the setup used for these monochrometer measurements. The LED used to illuminate the sample was chosen such that its peak wavelength was near the peak of the PPO absorption spectrum, shown in Figure 3.2c, so as to replicate the photoemission

process. An additional benefit of using a UV LED is that the light illuminating the sample and possibly leaking into the input slit of the monochrometer was outside of the wavelength range of interest for this measurement. A calibrated photodiode was used to measure the output power of the monochromator as a function of selected wavelength for each scintillator sample.

The results of the monochromator measurements are shown in Figure 3.13b, normalized to the highest peak in order to compare the shapes of the resulting spectra. The peak emission wavelength for all samples is located at (431.0 ± 0.5) nm, a value consistent with typical spectra of plastics in which POPOP is used as the secondary fluor, indicated in Figure 3.2c [122]. For both Gd-loaded samples, LS-iPr and LS-TMHD, an additional peak was observed at (441.0 ± 0.5) nm, which is not present in the unloaded sample, unLS. Therefore, even small amounts of Gd in the sample changes the shape of the emission spectra of the plastic scintillator.

3.5.2 Attenuation Length Measurements

The remaining intensity, $I(x)$ of a photon after traveling a distance, x, through a material is given by

$$I(x) = I_0 e^{-x/\lambda}, \tag{3.9}$$

where λ is defined as the attenuation length, or mean free path, of the photon. The effective attenuation length can be measured by placing a source of photons at precise locations along the length of a long plastic scintillator sample and measuring the resulting in intensity at each point. Cosmogenic muons are a reliable source for energy calibration for the interaction between particles and a plastic scintillator sample. The energy a muon will deposit in a scintillator depends on the density and size of the sample tested. Monte Carlo simulations yielded a most probably energy deposition value of (4.68 ± 0.36) MeV [99].

The energy deposited can be measured with a muon telescope as shown in Figure 3.14a, consisting of three layers of plastic scintillator. The top and bottom scintillators, which were placed perpendicular to each other in order to reduce the cross-sectional area, were coupled to PMTs and used in coincidence as a trigger for the center PMT. The center PMT was coupled to the middle scintillator, which was the plastic scintillator sample being tested. The cross-sectional area of the top and bottom scintillator was

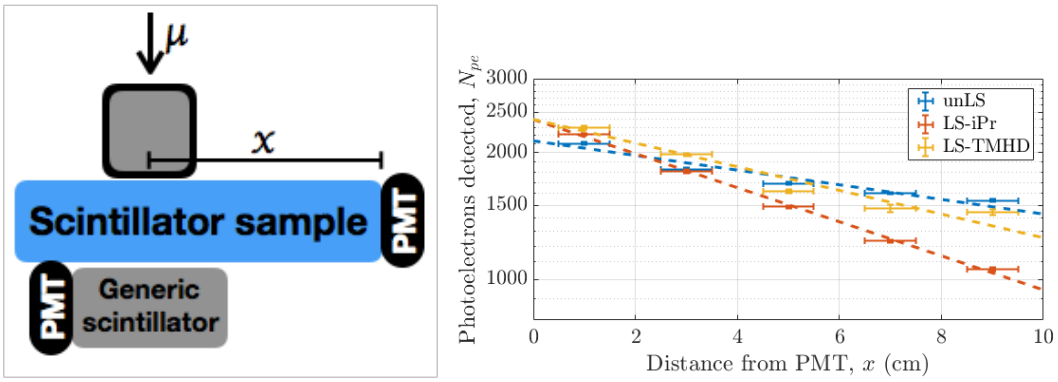

(a) Setup used for muon telescope.

(b) Attenuation lengths of fabricated samples.

Figure 3.14: In order to create the muon telescope (left), two generic scintillators placed in a perpendicular configuration were coupled to PMTs. At each distance, x, from the sample PMT, a histogram of the number of photoelectrons detected was fit to a Gaussian distribution. The mean of each fit was plotted against the distance (right). Figure adapted from [99].

limited to 2 cm×2 cm, such that a muon passing through both the top and the bottom scintillator would be bound to also pass through middle, sample scintillator close the center of the cross-section.

In order to minimize reflections from the back side of the sample scintillator distorting the expected distance traveled, x, a matte black material was used to cover the back of the sample. The remaining exterior surfaces were wrapped with PTFE tape for diffuse reflection. The number of photoelectrons detected per incident muon as a function of the distance of the muon interaction location from the face of the PMT was plotted to determine an effective attenuation length, shown Figure 3.14b. Attenuation lengths of 24.9 ± 2.1 cm for unLS, 10.70 ± 0.85 cm for LS-iPr, and 15.5 ± 1.3 cm for LS-TMHD were determined by fitting Equation 3.9 to the data from each sample. LS-iPr and LS-TMHD have the same Gd loading, so the difference between these two attenuation lengths (4.7 ± 2.2 cm) gives a measure of the systematic error due to the quality of the scintillator sample. Even with this additional error, the unloaded sampled still has a higher effective attenuation length than the loaded samples, suggesting that the presence of the gadolinium reduces the effective attenuation length of plastic

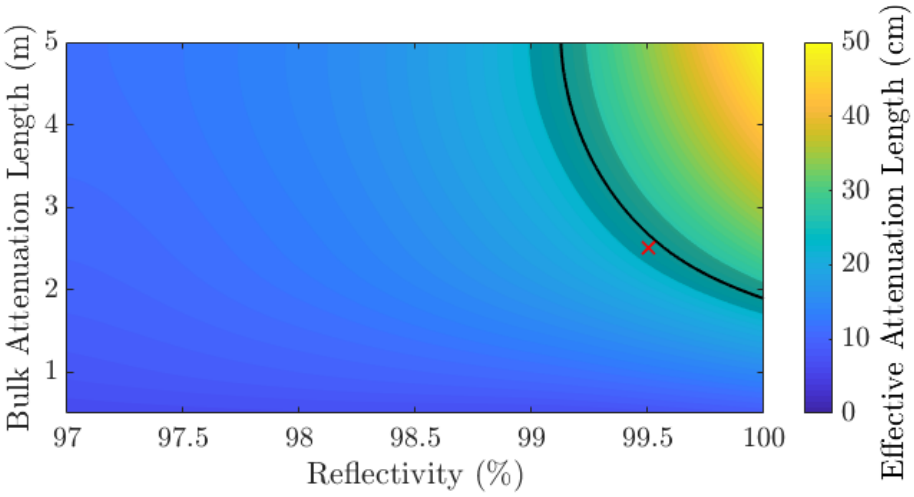

Figure 3.15: GEANT4-based simulations of muons interacting at varying distances, x, along the length of a scintillator sample give the effect of the 2D parameter space of bulk attenuation length and outer reflectivity on the effective attenuation length. The measured effective attenuation length is shown by the black curve with 1σ errors, and the chosen simulation parameters by the red x. Figure from [99].

scintillator.

The measured effective attenuation lengths for a small samples depend on its shape and the reflectivity of the coatings on its outer edges as well as bulk attenuation length listed in commercial specification sheets. A GEANT4-based simulation with additional optical properties defined and photon tracking enabled and using the same geometry and setup as the experimental measurement was used to determine the effect of outer reflectivity and bulk attenuation length on the effective attenuation length and determine reasonable values for these parameters. [99]. The effect of this 2D parameter space is shown in Figure 3.15. The measured effective attenuation length of the unloaded sample is shown by the black curve with 1σ errors. Without additional information to break the degeneracy between bulk attenuation length and reflectivity, any choice within the gray band could be reasonable. However, 2.5 m is a typical bulk attenuation length for plastics [123], so for further use in simulations of unloaded plastic scintillator, that was chosen for the bulk attenuation length. In order to stay within the gray 1σ band, the reflectivity of the outer wrapping was chosen to be 99.5%. This point is represented by

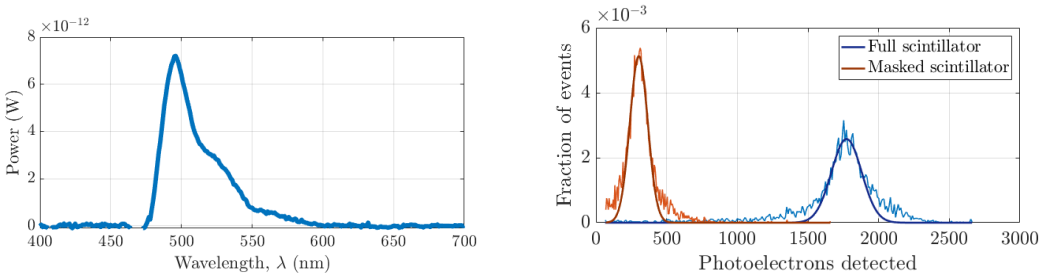

(a) Measured WLS fiber emission spectrum. (b) WLS fiber trapping efficiency measurement. The line thickness depicts measurement error.

Figure 3.16: Measurements of the WLS fiber. Figures from [99].

the red x in Figure 3.15.

3.5.3 Characterizing the WLS Fiber

To better understand the propagation of optical photons in a large volume of plastic scintillator containing WLS fibers, WLS fibers were embedded in some samples. Tests were made to add the WLS fiber during polymerization, but the in situ fibers melted due to the exothermic nature of the polymerization reaction. Ultimately, the best technique was to machine the fiber in place after polymerization had finished. The WLS fiber was cemented in a groove machined lengthwise down the center of sample unLS-WLS, as shown in Figure 3.12b. The end of the WLS fiber was painted with a reflective titanium-oxide-based paint, and then the entire sample was wrapped in PTFE for reflectivity.

The emission spectrum of the embedded WLS fiber was determined using a setup similar to what is shown in Figure 3.13 with the plastic sample replaced by a length of WLS fiber. Additionally, in order to ensure that the light entering the monochromator was only from the WLS fiber, the light source was placed perpendicular to the length of the fiber and blocked from the monochromator by black felt. The resulting emission spectrum is shown in Figure 3.16a. As expected the peak emission wavelength of the WLS fiber is shifted from the peak emission wavelength of the plastic scintillator. The maximum wavelength for the plastic was 431 ± 0.5 nm, and the maximum wavelength for the WLS fiber was 496 ± 0.5 nm.

The trapping efficiency is defined as

$$\text{Fiber trapping efficiency} = \frac{\text{optical photons at PMT from fiber}}{\text{optical photons produced in scintillator volume}} \tag{3.10}$$

and must be obtained using simulation. However, the light loss from using the fiber is a measurable quantity and is defined as

$$\text{light loss} = 1 - \frac{n_{\text{wls}}}{n_{\text{full scintillator}} - n_{\text{wls}}}, \tag{3.11}$$

where $n_{\text{full scintillator}}$ (n_{wls}) is the number of photoelectrons detected from the entire face of scintillator, including from the WLS fiber (from the WLS fiber only). Once the light loss has been measured, it can be compared to simulation of the same geometry in order to determine the WLS fiber trapping efficiency. In order to determine the light loss of the WLS fiber in the plastic samples, the energy deposited by muons was measured in two configurations. In the first configuration, the sample was connected to the PMT as shown previously, in Figure 3.14a. In the second configuration, a foil mask was placed between the sample and the PMT with a hole such that only the fiber was exposed. The muon peaks, shown in Figure 3.16b, were fit to Gaussian distributions.

Unfortunately, the hole in the foil mask used to block light from the scintillator was large enough to let in some light from the surrounding scintillator. GEANT4 based simulations using the parameters determined in Figure 3.15 were used to estimate the number of photoelectrons that would have been detected if the hole in the mask had been more appropriately sized. Experimentally, without the mask 1770 ± 110 photoelectrons were detected, and when using the mask, 304 ± 64 photoelectrons were detected. The simulations showed that only 187 ± 16 of the detected photoelectrons with the mask should be from the WLS fiber [99]. This leads to a calculated light loss of $88.2 \pm 1.4\%$. The simulation of the masked sample also give a fiber trapping efficiency of $8.8 \pm 3.3\%$ (or light loss of $91.2 \pm 3.3\%$), which is within error of the calculated light loss.

3.6 Future Plans for SuperCDMS SNOLAB

The results of the neutron veto sample testing show that upgrading the SuperCDMS SNOLAB shields to include a neutron veto is feasible. Plastic is an attractive choice because it mitigates the danger of leaks from a liquid option. The feasibility of using

gadolinium doped organic plastic scintillators read out using SiPMs coupled to WLS fibers has been tested in order to inform design decisions. WLS fibers were successfully machined into the quarter-scale prototype (Figure 3.1), and further testing and measurement can confirm whether or not the light output and fiber efficiency in that configuration will work for SuperCDMS SNOLAB.

Samples of Gd-doped plastic scintillators were successfully fabricated with up to 0.055% wt. Gd. This is a significantly lower concentration than what simulations show are necessary for SuperCDMS SNOLAB (loading of 1%. wt Gd); however, higher concentrations are possible with the use of co-monomers [111]. Collaboration with the Bertrand *et al.* [111] group has begun with the plan of testing their more highly-loaded samples. Additional testing of the layered (overloaded) plastic scintillator is also possible.

The proposed readout strategies for the active neutron veto were tested and characterized. These included quantum efficiency and photon detection efficiency measurements of the PMT and SiPMs respectively. Included within these measurements was a calculation of the gain of each photo detector. The gains were all calculated to be on the order of 10^6, and the quantum efficiencies were reasonably similar to the manufacturer's specifications (Figures 3.9b and 3.10b). Additionally, the dark count of one SiPM was measured to be 1.33 ± 0.52 MHz, which matches the the acceptable dark count rate at room temperature given by Hamamatsu [116].

The optical tests of plastic scintillator samples that were polymerized at UMN included the emission spectra (Figure 3.13b) and effective attenuation length measurements (Figure 3.14b). These tests showed only minor changes due to gadolinium loading; however, confirming this result at higher loadings would require additional testing. The corresponding simulations showed the degeneracy between the reflectivity of the outer wrapping and the bulk attenuation length of the plastic. The WLS fiber was also characterized by the emission spectrum and the fiber trapping efficiency. The results fall within a reasonable range, and therefore, the WLS fiber was determined to be a reasonable choice for the design.

Additional tests of the gadolinium-loaded samples are necessary in order to verify the neutron detection efficiency. Due to the small size of the samples, the gammas produced by the neutron interaction with gadolinium leave the scintillator sample and

are therefore not detected. Because the process of scaling up the samples is non-trivial, the most feasible plan is to surround the gadolinium-loaded samples with larger blocks of scintillator. The current design includes two large NaI crystals on opposite sides of the sample. Unfortunately, due to dead-time limitations of the data acquisition software and a limited supply of gadolinium, this task has not yet proved successful.

Chapter 4

Dark Matter Effective Field Theory

Note: This chapter has been previously published in Rogers *et al.* [124].

4.1 Introduction to Dark Matter Effective Field Theory

In the case of a positive signature in any direct dark matter detection experiment, the observed number of events and the spectral shape of the nuclear recoil spectrum can be used to determine the dark matter properties [125], including potential nonstandard momentum dependent contributions [126]. The goodness of the reconstruction is very sensitive to uncertainties in the astrophysical parameters describing the Milky Way halo [127] as well as in the nuclear form factors [128] and is also subject to statistical limitations [129]. Regarding the WIMP-nucleus cross section, current dark matter direct detection analyses generally interpret results based on the simplest models of spin-independent or spin-dependent interactions to foster easy comparison between experiments. These conventional assumptions include form factors that are based on models of the weak force that limit the possible structure of the target nucleus and dark matter itself. It was found that, while a single experiment would be insufficient to unambiguously discriminate between even spin-dependent and spin-independent couplings, a combination of targets [130–132] could be used to this aim.

Recently, a general description of the WIMP-nucleus interaction has been derived

using an effective field theory (EFT) approach [133–135]. This formalism extends the model-driven conventional technique by considering all relevant couplings in the non-relativistic limit [44, 58]. The addition of angular-momentum-dependent and spin-and-angular-momentum-dependent couplings means that EFT includes interaction operators which are also dependent on momentum transfer and the initial velocities [133]. The reconstruction of WIMP parameters is even more challenging in the resulting multidimensional parameter space. However, since each target nucleus is sensitive to different aspects of dark matter interactions [134], combining the results from multiple targets and techniques strongly constrains theoretical models in the absence of a detection and allows for determination of the underlying physics of the interaction once a signal is seen [58, 136]. It has thus been argued that next generation experiments constitute an excellent tool to probe the general EFT parameter space [137, 138] and identify the right theory [139, 140] of dark matter interactions. Adding information from annual modulation [141, 142] is particularly useful to identify a certain class of unconventional operators.

All interactions considered in the dark matter EFT formalism, listed in Table 4.1 by broad category, are four-fermion operators of elastic scattering between a dark matter particle (χ) and a target nucleon (N). The effective interaction Lagrangian is expected to be of the form

$$\mathscr{L}_{\text{int}} = \sum_{\tau} \sum_{i} c_i^{\tau} \mathcal{O}_i \overline{\chi} \chi \overline{\tau} \tau, \tag{4.1}$$

where τ can either be a sum over proton and neutron interactions or over isoscalar and isovector interactions and i sums over all interaction types (operators). Here, the isoscalar/isovector basis will be used instead of the proton/neutron one. While the goal of EFT is model independence, there are some symmetries and assumptions that limit the interaction types considered, as follows. The operator variables of the effective interaction Lagrangian must have Galilean invariance. This means that the momentum- and velocity-dependent terms must appear as the momentum transfer, $\vec{q} = \vec{p}_{\chi,\text{out}} - \vec{p}_{\chi,\text{in}}$, and the relative incoming velocities, $\vec{v} = \vec{v}_{\chi,\text{in}} - \vec{v}_{N,\text{in}}$. Only elastic collisions are considered, so the kinetic energy must be conserved [134] by

$$\frac{1}{2}\mu v^2 = \frac{1}{2}\mu(\vec{v} + \frac{\vec{q}}{\mu})^2, \tag{4.2}$$

Operator	Lagrangian expression	Nuclear response
P-even, $\vec{S}_\chi$-independent, T-conserving		
$\mathcal{O}_1$	1	M
$\mathcal{O}_2$	$(v^\perp)^2$	–
$\mathcal{O}_3$	$i\vec{S}_N \cdot (\vec{q}/m_N \times \vec{v}^\perp)$	Φ''/Σ'
P-even, $\vec{S}_\chi$-dependent, T-conserving		
$\mathcal{O}_4$	$\vec{S}_\chi \cdot \vec{S}_N$	Σ'/Σ''
$\mathcal{O}_5$	$i\vec{S}_\chi \cdot (\vec{q}/m_N \times \vec{v}^\perp)$	M/Δ
$\mathcal{O}_6$	$(\vec{S}_\chi \cdot \vec{q}/m_N)(\vec{S}_N \cdot \vec{q}/m_N)$	Σ''
P-odd, $\vec{S}_\chi$-independent,T-conserving		
$\mathcal{O}_7$	$\vec{S}_N \cdot \vec{v}^\perp$	Σ'
P-odd, $\vec{S}_\chi$-dependent, T-conserving		
$\mathcal{O}_8$	$\vec{S}_\chi \cdot \vec{v}^\perp$	M/Δ
$\mathcal{O}_9$	$i\vec{S}_\chi \cdot (\vec{S}_N \times \vec{q}/m_N)$	Σ'
P-odd, $\vec{S}_\chi$-independent, T-violating		
$\mathcal{O}_{10}$	$i\vec{S}_N \cdot \vec{q}/m_N$	Σ''
P-odd, $\vec{S}_\chi$-dependent, T-violating		
$\mathcal{O}_{11}$	$i\vec{S}_\chi \cdot \vec{q}/m_N$	M

Table 4.1: EFT interaction operators of the effective interaction Lagrangian separated into categories of similar parity, time-reversal symmetry, and WIMP spin dependence. The nuclear responses of the target nucleus is included as well [133].

which leads to

$$\vec{v} \cdot \vec{q} = -\frac{q^2}{2\mu}. \tag{4.3}$$

Requiring the interaction to be Hermitian means that only four terms may appear anywhere in the effective interaction Lagrangian: the momentum transfer, $i\vec{q}/m_N$, the spin of the target, $\vec{S}_N$, the possible spin of the dark matter particle, $\vec{S}_\chi$, and the transverse component of the incoming velocity, $\vec{v}^\perp = \vec{v} + \vec{q}/2\mu$ [135]. The transverse component of the incoming velocity is chosen such that each term is linearly independent

of all others. For example,

$$\vec{v}^{\perp} \cdot \vec{q} = 0. \tag{4.4}$$

The EFT operators shown in Table 4.1 all consist of combinations of these four terms, except for $\mathcal{O}_1$, which, as the spin-independent (SI) operator, is the simplest interaction possible. Standard SI dark matter analyses compute parameter constraints assuming that interactions with protons and neutrons are the same. This corresponds to the EFT isoscalar case defined here. EFT $\mathcal{O}_4$ is the standard spin-dependent (SD) operator and is dependent on the spin of both dark matter and the target nuclei. Past SD analyses typically assumed the proton/neutron basis instead of the isoscalar/isovector basis. Operators may also have angular-momentum-dependent (LD) or spin-and-angular-momentum-dependent (LSD) interactions. Some operators, such as $\mathcal{O}_3$ and $\mathcal{O}_5$, are dependent on the momentum transfer and are characterized by different shapes of the recoil energy spectra than is typically assumed. As shown later, experiments with low energy thresholds are particularly important for discriminating between operators associated with different spectral shapes.

If Lorentz invariance is required, then time-reversal symmetry must also be considered. Therefore, the possible interaction terms are organized by Table 4.1 into T-conserving and T-violating types. The interactions are also classified by whether they have even or odd parity and if they depend on dark matter spin, $\vec{S}_{\chi}$. Within similar regions, there can be interference between operators. For example, interference terms in the Lagrangian exist between $\mathcal{O}_1$ and $\mathcal{O}_3$, $\mathcal{O}_4$ and $\mathcal{O}_5$, $\mathcal{O}_4$ and $\mathcal{O}_6$, and $\mathcal{O}_8$ and $\mathcal{O}_9$ [133].

All of the EFT operators are found as leading-order terms in the nonrelativistic reduction of a relativistic operator with a traditional spin-0 or spin-1 mediator except for $\mathcal{O}_2$. For this reason, $\mathcal{O}_2$ is not considered. Four more nonrelativistic operators exist from interactions without a spin-0 or spin-1 mediator; however, these are not linearly independent from the first eleven and are therefore not considered [135].

In order to calculate the cross-section or event rate expected from the effective interactive Lagrangian, the nuclear response for each isotope of the target material must be known for each interaction term. The most general assumptions separate out interaction with protons and neutrons. These nuclear responses were determined by Fitzpatrick et al. [133, 134] by approximating the structure of the nucleus with a shell model and implementing well-tested electroweak interactions. The full shell model is

Nuclear Response	Description	Type
M	SI	scalar
Σ"	SD1	vector
Σ'	SD2	vector
Δ	LD	vector
Φ"	LSD	tensor
M, Φ"	SI and LSD	interference
Σ', Δ	SD2 and LD	interference

Table 4.2: Nuclear responses and interference terms. See [133, 134] for full description.

expanded as a translationally-seperable harmonic-oscillator Slater-determinant basis. The basis is transferred into the center-of-mass frame in order to use the $1s$ state. A multipole expansion was used to simplify the calculated form factors from known selection rules based on rotational invariance and parity and time-reversal symmetries [133]. The density matrices used to calculate nuclear responses use a shell approximation instead of a point-nucleus approximation, because, for the energy ranges of interest, the momentum transfer and the inverse nuclear size are relatively close. This density matrix can be calculated using the equation

$$\Psi^{J;\tau}_{|\alpha|,|\beta|} \equiv \frac{1}{\sqrt{(2J+1)(2\tau+1)}} \langle j_N; T \vdots\vdots \left[c^\dagger_{|\alpha|} \otimes \tilde{c}_{|\beta|} \right]_{J;\tau} \vdots\vdots j_N; T \rangle, \tag{4.5}$$

where $c^\dagger_{|\alpha|}$ is a single particle creation operator and $\tilde{c}_{|\beta|}$ is a destruction operator. The triple dots ($\vdots\vdots$) denote that this matrix element is reduced in both spin and isospin [135]. In general, the dark matter response is not completely separate from the nuclear response because a single nuclear matrix element may contain several EFT couplings. For example, the spin-independent nuclear response (M) can be found in the couplings of $\mathcal{O}_1$, $\mathcal{O}_5$, $\mathcal{O}_8$, and $\mathcal{O}_{11}$ [133].

The form factors calculated from this theory for the eleven operators listed in Table 4.1 use five nuclear responses, and the operator interference terms use two nuclear response interference terms, listed in Table 4.2. There is a SI response (M), two SD responses (Σ' and Σ''), a LD response (Δ), and a LSD response (Φ''). One of the SD responses, Σ'', is the projection of the spin in the direction parallel to momentum

transfer, $\vec{q}$, and the other, Σ', is the projection of spin in the direction perpendicular to momentum transfer. The standard SD interaction is a linear combination of these two nuclear responses [134].

All isotopes of a particular target will have form factors for SI or scalar interactions. Only isotopes with ground-state spins greater than 1/2 will have form factors for SD or vector interactions, and only isotopes with ground-state spins greater than 1 will have form factors for tensor interactions. For Germanium isotopes (^{70}Ge, ^{72}Ge, ^{73}Ge, ^{74}Ge, and ^{76}Ge) only ^{73}Ge, whose spin is 9/2, will have form factors for vector or tensor interactions [133].

Once the form factors for each interaction are known, the differential cross section is calculated as follows:

$$\frac{d\sigma}{d\cos\theta} = \frac{\mu^2}{32\pi m_\chi^2 m_N^2} \sum_{i,j=1}^{11} \sum_{\tau,\tau'} c_i^\tau c_j^{\tau'} F_{i,j}^{\tau,\tau'}(v^2, q^2), \tag{4.6}$$

where c_i^τ is the coupling coefficient for the i^{th} interaction term to the nucleon or isospin. A listing of form factors for fluorine, sodium, germanium, iodine, and xenon can be found in Fitzpatrick *et al* [133]. This leads to a differential event rate per detector mass (cf. Equation 1.3) of

$$\frac{dR}{dE_R} = N_T \frac{\rho_\chi m_T}{32\pi m_\chi^3 m_N^2} \int_{v_{min}}^{\infty} d^3\vec{v} \frac{f(\vec{v})}{v} \sum_{i,j=1}^{11} \sum_{\tau,\tau'} c_i^\tau c_j^{\tau'} F_{i,j}^{\tau,\tau'}(v^2, q^2), \tag{4.7}$$

where N_T is the number of target nuclei per detector mass and the maximum WIMP velocity is encoded in the Gaussian cutoff defined in Equation 1.5.

The differential rate equation (Equation 4.7) can be calculated as a sum over isospin (isoscalar and isovector) or as a sum over protons and neutrons. The coupling coefficients, c_i^τ, can be converted between the nucleon and isospin bases by

$$c_i^0 = \frac{1}{2}(c_i^p + c_i^n) \tag{4.8}$$

and

$$c_i^1 = \frac{1}{2}(c_i^p - c_i^n), \tag{4.9}$$

where c_i^0 is the isoscalar interaction and c_i^1 is the isovector interaction [135].

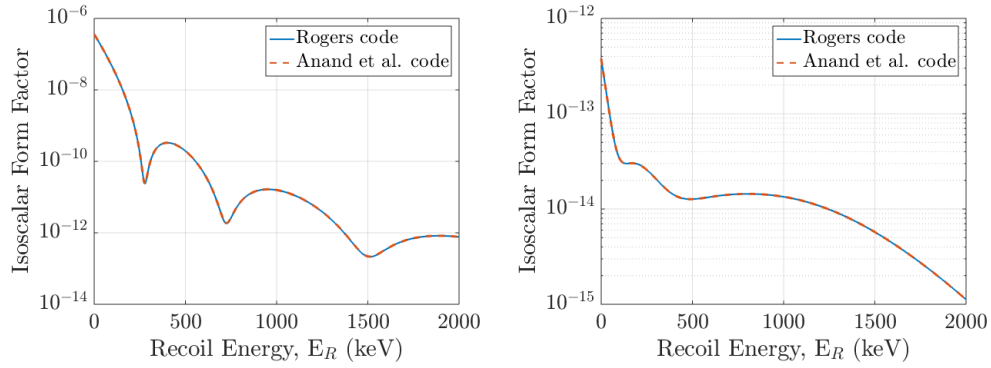

(a) $\mathcal{O}_1$ (isoscalar) coupling form factor (b) $\mathcal{O}_4$ (isoscalar) coupling form factor

Figure 4.1: Comparison of the calculated form factor from Anand et al. [135] and my MatLab code for operators $\mathcal{O}_1$ and $\mathcal{O}_4$. The two lines are nearly identical, and therefore, no difference is visible between the two on these plots.

4.2 Multidimensional EFT Analysis Technique

Anand et al. [135] have written a general dark matter EFT package in Mathematica that calculates the differential event rate or differential cross-section, among other options, given a WIMP mass and non-zero coupling coefficients. I have written a version of this code for CDMS in MatLab. A comparison of the form factors for two of the couplings are shown in Figure 4.1, and a comparison of differential event rate is shown in Figure 4.2. The discrepancies of the event rate at ~ 15 keV are due to the differences in velocity distributions used in the code.

Instead of the Optimum Interval method, in order to interpret data from direct detection experiments within the general context of EFT operators, a likelihood calculation is carried out comparing the data to theoretical models. The main drawback to using the Optimum Interval method to explore the EFT operators is that it sets limits for only one interaction at a time. Because of interference between EFT operators, this method cannot be used to give an accurate description of the full dimension of the EFT parameter space.

Given the low number of expected detected WIMP events, a Poissonian likelihood function is the most reasonable choice to compare the detected recoil energy spectra with

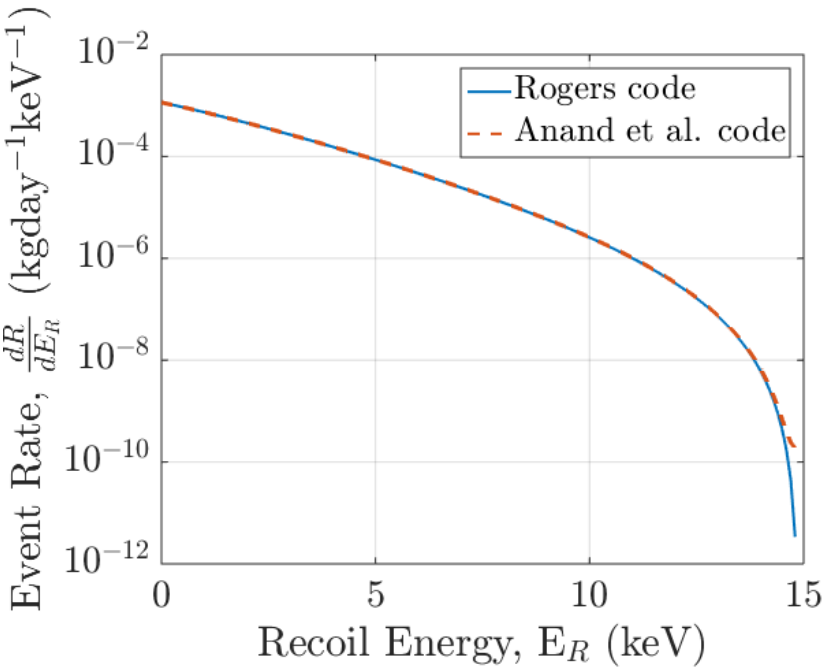

Figure 4.2: Comparison of calculated differential event rate for operator $\mathcal{O}_1$ at a WIMP mass of 10 GeV/c^2 for Anand et al. [135] and my MatLab code.

the theoretical spectra. This method has been used in maximum likelihood analyses for many different dark matter experiments. Often in dark matter analyses the likelihood function used includes only a single energy bin, sacrificing discrimination based on the recoil energy for simplicity [44, 58, 129, 137, 138, 142]. In order to include the spectral information of both the expected WIMP spectrum and the detected events, the Poissonian likelihood can be split into n bins, giving a dark matter-only likelihood, $\mathcal{L}^{\mathrm{DM}}$, of

$$\mathcal{L}^{\mathrm{DM}} = \prod_{k=1}^{n} \frac{1}{N_k!} \eta_k^{N_k} e^{-\eta_k}, \tag{4.10}$$

where η_k is the expected number of events, and N_k is the number of detected events in the k^{th} energy bin. Binned likelihood functions have been used in some previous dark matter analyses as well [136, 140]. The expected number of events in any given energy bin is calculated using Equation 4.7 for a chosen combination of WIMP mass, m_χ, and

nonzero coupling coefficients; therefore,

$$\eta_k(\{m_\chi, c_i^0, c_i^1\}) = \int_{E_k} \epsilon(E_R) \frac{dR}{dE_R}\, dE_R, \tag{4.11}$$

where $\epsilon(E_R)$ is the energy-dependent efficiency and exposure, i ranges over any operators with nonzero coupling coefficients in either isoscalar (c_i^0) or isovector (c_i^1) directions, and the integral is evaluated over the k^{th} energy bin E_k.

If only one EFT operator is considered, instead of calculating the likelihoods in terms of the coupling coefficients, likelihoods can also be calculated in polar EFT coordinates of amplitude, A, and phase, θ. The total coupling coefficient amplitude is calculated by

$$A_i^2 = (c_i^0)^2 + (c_i^1)^2 \tag{4.12}$$

and can be seen as an analogue to cross-section, σ_i with approximately $\sigma_i \propto A_i^2$. The coupling coefficient phase is calculated by

$$\theta_i = \tan\left(c_i^0 / c_i^1\right). \tag{4.13}$$

The limits set in polar coordinates can be converted into the coupling-coefficient plane by recognizing that

$$\begin{aligned} c_i^0 &= A_i \sin(\theta_i) \\ c_i^1 &= A_i \cos(\theta_i). \end{aligned} \tag{4.14}$$

If the energy dependence of the backgrounds is known for an experiment, this can be added into the likelihood function as

$$\mathcal{L}^{\text{DM+bkg}} = \prod_{k=1}^{n} \frac{1}{N_k!} (\eta_k + b_k)^{N_k} e^{-(\eta_k + b_k)}, \tag{4.15}$$

where b_k is the number of background events in the k^{th} energy bin. Most experiments only publish an estimate of their backgrounds across their entire energy range. Because of this, previous analyses have ignored expected background all together [136, 137, 140, 142] or only used simplistic and assumed background models [138, 139]. In order to include the background, our likelihood definition, therefore, must allow for a constraint on the total (single energy bin) background estimate, while still retaining the binned energy formalism for the WIMP data. In order to include an unbinned background in

a binned likelihood, we consider all possible background configurations across energy bins that yield a total count within 2σ of the expected total background, B. The background configuration that maximizes the likelihood is then accepted. The number of background configurations to be tested is determined by how many ways the total number of background counts can be distributed into all of the energy bins and is, most generally,

$$\text{number of background combinations} = \frac{(n+B-1)!}{(n-1)!B!}. \tag{4.16}$$

For $n = 100$ energy bins, the number of combinations necessary to test is computationally feasible for a maximum expected background of four counts or less ($B + 2\sigma \leq 4.49$). Using this method, the likelihood can be defined for an expected total background B with error σ as

$$\mathcal{L}^{\text{DM+bkg}} = \frac{1}{\sqrt{2\pi\sigma}} e^{-(\sum_k^n b_k - B)^2/2\sigma^2} \prod_{k=1}^{n} \frac{1}{N_k!} (\eta_k + b_k)^{N_k} e^{-(\eta_k + b_k)}. \tag{4.17}$$

Once the likelihood has been calculated for a specific experiment, it can be combined with the likelihoods for other experiments (with potentially different targets) in order to better probe the operator space, as has been shown to be useful in previous analyses [126, 129, 136]. The likelihoods are combined as

$$\mathcal{L}_{\text{combined}} = \prod_j \mathcal{L}_j, \tag{4.18}$$

where $\mathcal{L}_j$ is the likelihood of the j^{th} experiment. The resulting likelihoods can be used to show the effect of each experiment (or target) on the chosen operator space and to set joint constraints on the operator space due to all available experiments. Generally, once multiplied together, the 95% confidence contours calculated from the joint likelihood are tighter and more clearly defined.

The theoretical spectrum, η_k, is a function of the WIMP mass and all of the possible EFT coupling coefficients, thus our parameter space $\{m_\chi, c_i^0, c_i^1\}$ contains up to 23 variables. An efficient method of scanning over all possible dimensions, especially since the likelihood functions tend to be multimodal, is by using the nested sampling Monte Carlo software package MultiNest [143–145], a Bayesian inference tool that can be used for parameter estimation or model comparison and selection. The nested sampling technique used by MultiNest involves an optimized set of live points from the full

likelihood. This optimized set includes the points of highest likelihood such that at each iteration of the algorithm a live point of the lowest likelihood is replaced with a point of higher likelihood [143].

Even with a software program like MultiNest, calculating a 23-dimensional likelihood remains computationally intensive and time consuming. Hence, exploring the likelihood over 3D subspaces corresponding to individual EFT operators (spanned by $\{m_\chi, c_i^0, c_i^1\}$ for the operator $\mathcal{O}_i$) could be used to initially identify which operators are the most consistent with the data. For this purpose we use the Bayesian evidence, $\mathcal{Z}$, to calculate the probability that the detected data, N_k, is best represented by a given operator hypothesis, H, and is calculated by

$$\mathcal{Z} = \int dH \mathcal{L}(N_k|H)\Pr(H), \tag{4.19}$$

with the integral over all parameters belonging to that operator hypothesis and where $\Pr(H)$ is the prior for each parameter. For the 3D example with a single operator $\mathcal{O}_i$,

$$\mathcal{Z}_i = \int dm_\chi dc_i^0 dc_i^1 \mathcal{L}(\{m_\chi, c_i^0, c_i^1\})\Pr(\{m_\chi, c_i^0, c_i^1\}) \tag{4.20}$$

with flat priors assumed for each parameter. The evidence is used in Bayes' theorem as

$$\mathcal{P}(\{m_\chi, c_i^0, c_i^1\}|N_k) = \frac{\mathcal{L}(N_k|\{m_\chi, c_i^0, c_i^1\})\Pr(\{m_\chi, c_i^0, c_i^1\})}{\mathcal{Z}}, \tag{4.21}$$

where $\mathcal{P}(\{m_\chi, c_i^0, c_i^1\}|\{N_k\})$ is the posterior probability distribution in the $\{m_\chi, c_i^0, c_i^1\}$ parameter space given the observed data, $\{N_k\}$. For a given experiment, the operators with the highest Bayesian evidence [1] should be most relevant to the data and thus most likely to give nonzero coupling coefficients when analyzed jointly with other operators. The Bayesian evidence has become a fairly standard way of comparing competing models within dark matter likelihood analyses [137, 138, 140, 142, 143]. In order to visualize 3D or higher dimensional likelihoods, the likelihoods can be marginalized down

[1] Suppose the class of models considered consists of two models, A and B, with model A having *a priori* probability P_A and separate Bayesian evidence $\mathcal{Z}_\mathrm{A}$, while model B has probability $P_\mathrm{B} = 1 - P_\mathrm{A}$ and Bayesian evidence $\mathcal{Z}_\mathrm{B}$. Then the data can be considered to favor model A if the posterior probability, P'_A, is larger than the *a priori* probability, P_A. Bayes' theorem gives

$$P'_\mathrm{A} = \frac{P_\mathrm{A}\mathcal{Z}_\mathrm{A}}{P_\mathrm{A}\mathcal{Z}_\mathrm{A} + (1 - P_\mathrm{A})\mathcal{Z}_\mathrm{B}} \tag{4.22}$$

which implies $P'_\mathrm{A} > P_\mathrm{A}$ if and only if $\mathcal{Z}_\mathrm{A}/\mathcal{Z}_\mathrm{B} > 1$. If there are more than two hypotheses considered in the class of models, this holds true as long as model B includes all models except model A.

to multiple 2D and 1D marginalized likelihoods. Contours at 95% confidence can be calculated in 2D planes to place constraints on likely WIMP mass and coupling coefficient values. 1D marginalized likelihoods can be used to determine the 95% confidence regions for each parameter individually, by integrating down from the point of highest likelihood. We calculate the 95% confidence intervals, because they have been shown to be a reliable method of estimating the true values of likelihood parameters for dark matter experiments [129].

We propose the following procedure for analyzing direct dark matter detection data from one or more experiments in the vast EFT parameter space:

1. Assuming a flat prior for all parameters involved, run 3D analysis for each EFT operator computing the likelihood dependent only on the WIMP mass and the isoscalar and isovector coupling coefficients of that operator.

2. Calculate the Bayesian evidence, as defined in Equation 4.20, for each operator's 3D likelihood. The evidence can be used to determine which operators or combination of operators are most relevant to the data set and therefore, which model best represents the dark matter interaction.

3. Run 5D or higher dimensional analysis for the combination of two or more relevant operators determined in step 2, and compute constraints on the WIMP mass and relevant coupling coefficients simultaneously over all relevant EFT operators.

4. Combine the likelihoods of individual experiments for relevant operators into one likelihood. The joint likelihood can be used to compute the most stringent constraints on EFT parameters, using information from all available experiments.

Chapter 5

Dark Matter EFT Analysis

Note: Most of this chapter has been previously published in Rogers et al. [124] or will be published in Agnese *et al.* [146].

5.1 Exploration of EFT Parameter Space

Each operator of the dark matter EFT, shown in Table 4.1 requires two parameters to describe the coupling to the target material. These parameters can be either the coupling coefficients (isoscalar/isovector or proton/neutron) or the amplitude and phase as defined in Equations 4.12 and 4.13. Including WIMP mass, this leads to 21 parameters describing the full EFT parameter space. Further analysis is necessary in order to understand how each parameter effects the overall shape of the theoretical spectrum. This has been done previously using a principal component analysis to determine directions of maximum destructive and constructive interference between interacting operators [147].

Another way of comparing the EFT operators is by relative strength to get a single event for an assumed efficiency and exposure. The expected rate, given by Equation 4.10, is proportional to the coupling coefficients, $\{c_i^0, c_i^1\}$, and the operator form factors, $F_{i,j}^{\tau,\tau'}$, as

$$\frac{dR}{dE} \propto \int_{v_{\min}}^{\infty} d^3\vec{v} \frac{f(\vec{v})}{v} \sum_{i,j=1}^{11} \sum_{\tau,\tau'} c_i^\tau c_j^{\tau'} F_{i,j}^{\tau,\tau'}(v^2, q^2). \tag{5.1}$$

Because the velocity dependences of the form factors are known and are one of two options (v^0 or v^2), the integration over velocity can be carried out to get velocity

independent form factors, $F_{i,j}^{\tau,\tau'}(q^2)$. This gives a rate equation of

$$\frac{dR}{dE} \propto \sum_{i,j=1}^{11} \sum_{\tau,\tau'} c_i^{\tau} c_j^{\tau'} F_{i,j}^{\tau,\tau'}(q^2). \tag{5.2}$$

Because we are only considering single operators ($i = j$) within the isoscalar/isovector basis ($\tau, \tau' = 0, 1$), this simplifies to

$$\frac{dR}{dE} \propto (c_i^0)^2 F_i^{(0,0)}(q^2) + 2c_i^0 c_i^1 F_i^{(0,1)}(q^2) + (c_i^1)^2 F_i^{(1,1)}(q^2) \tag{5.3}$$

with $F_i^{(0,1)} = F_i^{(1,0)}$. For a chosen coupling coefficient phase, θ_c and arbitrary amplitude, A_i, this equation becomes

$$\frac{dR_i}{dE} \propto A_i^2 \cos^2\theta_c \left(\tan^2\theta_c F_i^{(0,0)}(q^2) + 2\tan\theta_c F_i^{(0,1)}(q^2) + F_i^{(1,1)}(q^2)\right) \tag{5.4}$$

or

$$\frac{dR_i}{dE} \propto A_i^2 \left.\frac{dR}{dE}\right|_{A_i=1}. \tag{5.5}$$

For an isoscalar-only interaction, $c_i^1 = 0$ (isovector-only, $c_i^0 = 0$), the phase is given by $\theta_i = \pi/2$ ($\theta_i = 0$).

The total number of expected events, N_i, is calculated by

$$N_i = \int dE\epsilon(E)\frac{dR_i}{dE} = A_i^2 \int dE\epsilon(E) \left.\frac{dR_i}{dE}\right|_{A_i=1}, \tag{5.6}$$

where $\epsilon(E)$ is the experimental exposure and energy-dependent efficiency. If $N_i = 1$, then

$$A_i^{\text{str}} = \frac{1}{\sqrt{\int dE\epsilon(E) \left.\frac{dR}{dE}\right|_{A_i=1}}} \tag{5.7}$$

is the amplitude required to get 1 total event at the chosen phase, θ_c. The larger the value of A_i is, the weaker the operator is.

In order to see the effect of exposure and energy threshold, two representative efficiencies and exposures were chosen: one based on CDMS II Ge [148], and one based on CDMSlite [48]. The two live times are shown in Figure 5.1. The CDMS II Ge experiment has a higher energy threshold than CDMSlite and an overall larger live time. This allows for a comparison of the effect of a lower threshold on spectral shape, but the change in overall exposure complicates the comparison of relative strength of the

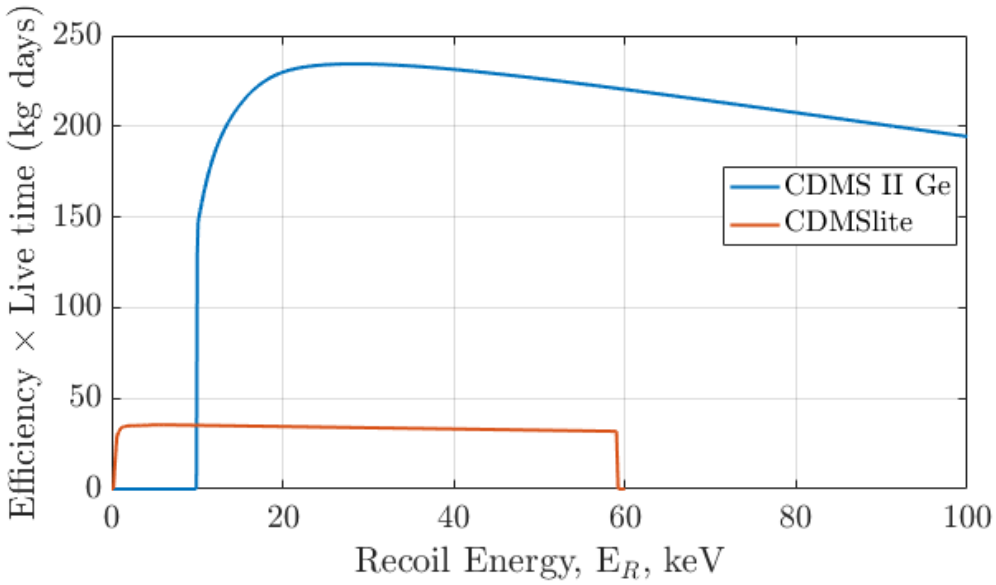

Figure 5.1: Comparison of exposures based on CDMS II Ge [148] (blue) and CDMSlite [48] (orange) chosen for the exploration of the EFT parameter space.

coupling coefficients. The change in strength will be due to both the change in live time and in the energy threshold. These two variables have opposite effects on coupling coefficient strength. Therefore, comparisons of coupling coefficient strength are only useful between operators within one experiment but not between the two experiments.

Figure 5.2 shows the coupling-coefficient amplitude for each EFT operator required to get 1 event for an isoscalar-only ($\theta_c = \pi/2$) interaction for both of the chosen experiments. The affect of the lower threshold of the CDMSlite experiment can be seen by the lower reach in mass in Figure 5.2b than in Figure 5.2a. Once the spectrum of a WIMP mass is below the experimental threshold, no coupling-coefficient amplitude can result in 1 event. The effect of the difference in exposures is less obvious, but the operators require slightly smaller (on the order of half an order of magnitude) amplitudes to get 1 event for CDMS II Ge than for CDMSlite. Because which experiment is chosen doesn't have a large effect on the coupling-coefficient amplitude strength, this shows that the decrease in experimental threshold and decrease in exposure can balance each other out.

Figure 5.2 also shows the difference in magnitude between the coupling-coefficient

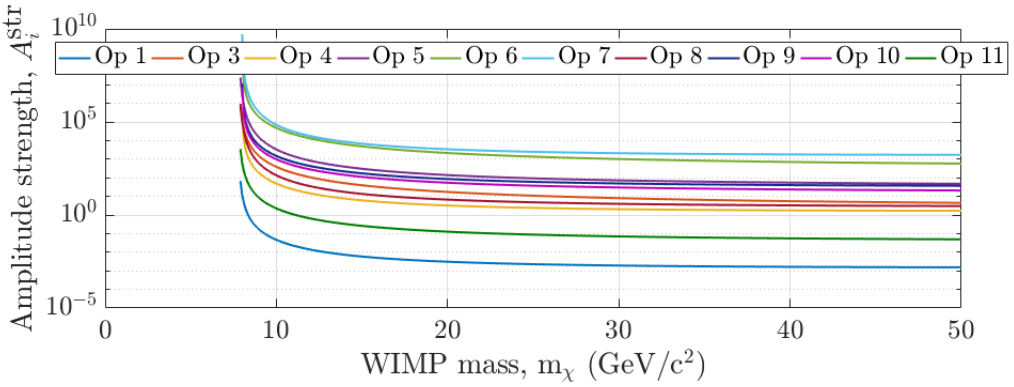

(a) CDMS II Ge

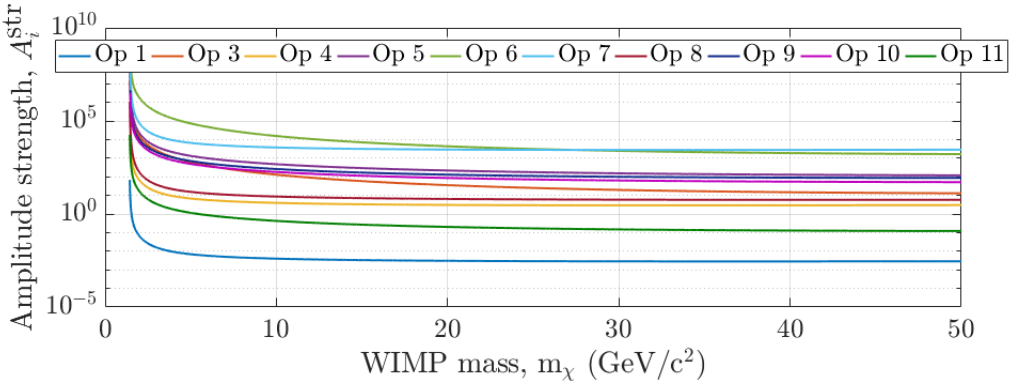

(b) CDMSlite

Figure 5.2: The coupling-coefficient amplitude required to get 1 event for a proton-only ($\theta_c = \pi/2$) interaction for each EFT operator shown for CDMS II Ge (top) and CDMSlite (bottom).

amplitude necessary to get 1 event between the weakest and the strongest EFT operators. The mass-dependence and order of the operators is similar for both experiments chosen. In both cases, EFT operator 1 (the typically chosen SI operator) is the strongest operator, as it requires the smallest coupling-coefficient amplitude to get 1 event. EFT operators 6 and 7 are the weakest, with the order of these two switching around 25 GeV for CDMSlite. The rest of the operators fall somewhere between these limits.

As shown in Equation 5.3, the rate equation depends on an interference term, represented by the form factor $F_i^{(0,1)}(q^2)$. This represents the interference between the

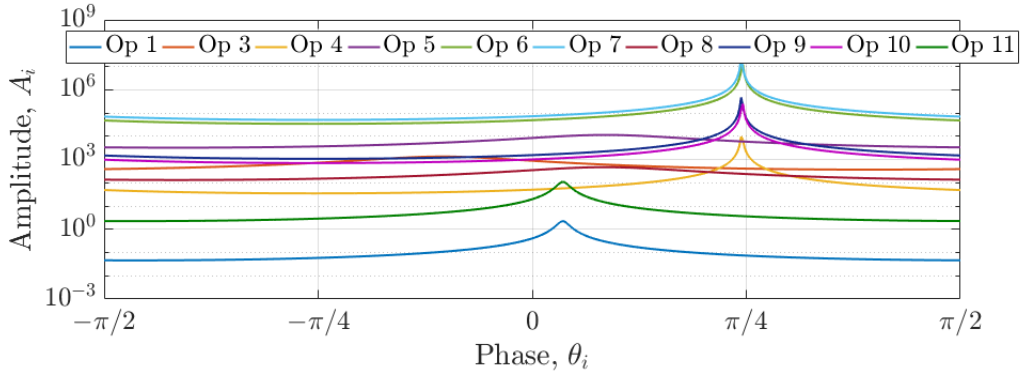

(a) CDMS II Ge

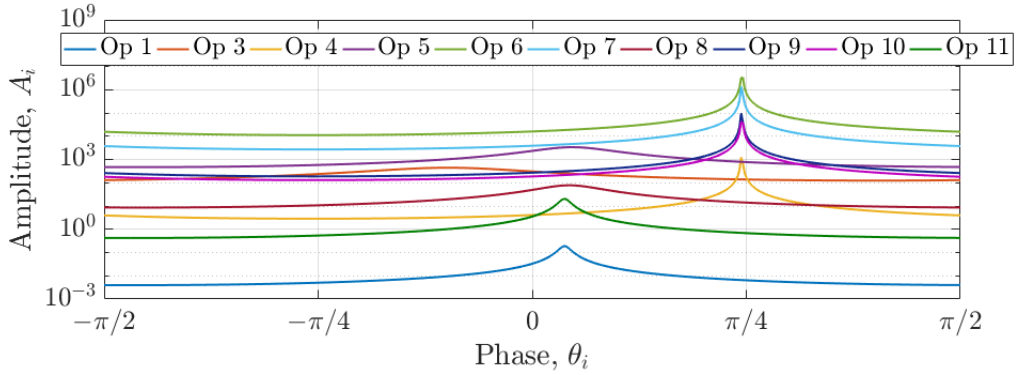

(b) CDMSlite

Figure 5.3: Maximum interference phases for each EFT operator at 10 GeV for CDMS II Ge (top) and CDMSlite (bottom).

isoscalar and isovector (or proton and neutron) terms within a single EFT operator. There also exists interference terms between operators 1 and 3, 4 and 5, 4 and 6, and 8 and 9, but these are not considered here. For each interference, there is a coupling-coefficient phase, θ_i, such that the event rate is minimized. This phase corresponds to the maximum interference of the parameter space and may contain a dependence on WIMP mass. At this minimum phase, there will be a positive spike in the amplitude required to get 1 event.

Figure 5.3 shows the maximum interference phases for all EFT operators using both chosen experiments at a WIMP mass of 10 GeV. In general, the same pattern in

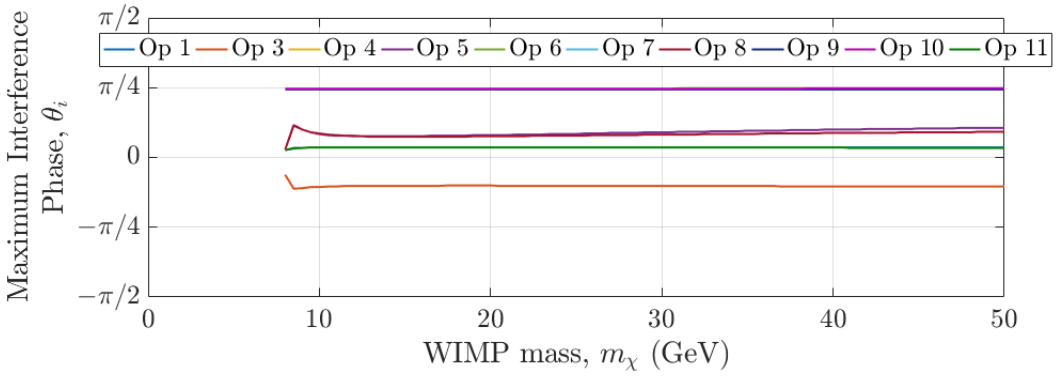

(a) CDMS II Ge

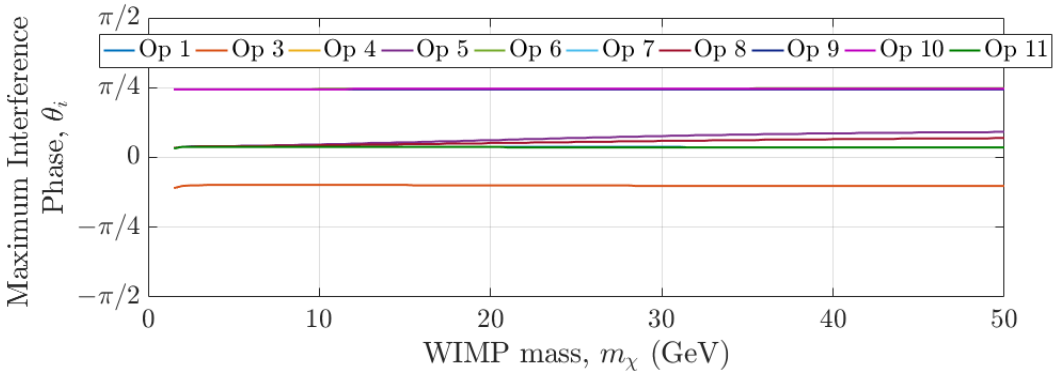

(b) CDMSlite

Figure 5.4: The mass dependence of the maximum interference phases for each EFT operator for CDMS II Ge (top) and CDMSlite (bottom).

strength of operators that was seen for isoscalar-only ($\theta_c = \pi/2$) is seen for the entire range of phases. However, for the operators with a sharp maximum interference regions, the coupling-coefficient amplitude increases by a couple of orders of magnitude in that region and may cross another operator, changing the order of relative strengths. In general, the two strongest operators are 1 and 11, the two weakest are 6 and 7, and the rest are somewhere in between. However, this plot also shows additional categorizations of operators based on the maximum interference phase. This is also seen, along with the mass dependence of this ratio, in Figure 5.4. These patterns are as follows:

- Operators 1 and 11 have strong mass-independent maximum interference phases

around $\theta_c = 0.1$. As shown in Table 4.1, these two operators have identical nuclear responses of M or SI only. However, they have exactly opposite symmetries for parity and time-reversal and dependence on the WIMP spin.

- Operators 4, 6, 7, 9, and 10 all have strong mass-independent maximum interference ratios just less than $\theta_c = \pi/4$. These operators all have nuclear responses consisting of only Σ' or Σ'', the two SD responses. Most of these come from different symmetry categories in Table 4.1; however, operators 4 and 6 are from the same category and have interference terms between them as well.

- Operators 5 and 8 both have weak or wide maximum interference ratios that show a strong mass dependence. For CDMSlite, this ratio starts around $\theta_c = 0.1$ and ends around $\theta_c = 0.2 - 0.3$. For CDMS II Ge, this ratio stays in the region around the $\theta_c = 0.2 - 0.3$ with a small spike around $m_\chi = 8.5$ GeV. These operators both have nuclear responses consisting of the SI M and the LD Δ and are from different symmetry categories in Table 4.1.

- Operator 3 is the only one to show a negative maximum interference ratio. It has a weak or wide ratio around $\theta_c = -0.3$ that is not mass dependent. Operator 3 has one SD nuclear response (Σ') and one LSD response (Φ'').

An additional way of categorizing the EFT operators is by the spectral shape of the event rate. Figure 5.5 compares the two spectral shape options using the efficiency and exposures of Figure 5.1. Each plot includes the isoscalar spectral shape for 4 different WIMP masses whose amplitudes have been normalized for 1 event as described in Equation 5.7. The experimental threshold is included for comparison.

In general, there are two spectral shapes seen within the EFT operators: exponential decay and a beta distribution. Operators 1, 4, 7, and 8 show exponential decay; while operators 3, 5, 6, 9, 10, and 11 look more like the beta distribution. Unlike the maximum interference region, which seemed most effected by the nuclear response, the shape is most strongly influenced by the momentum dependence of the operator. Operators 1, 4, 7, and 8 have no dependence on momentum transfer, q. All of the operators with a beta distribution-like shape all show some dependence on q. Operator 6 has a dependence on q^2; all others are just dependent on q. These dependencies are shown in Table 4.1.

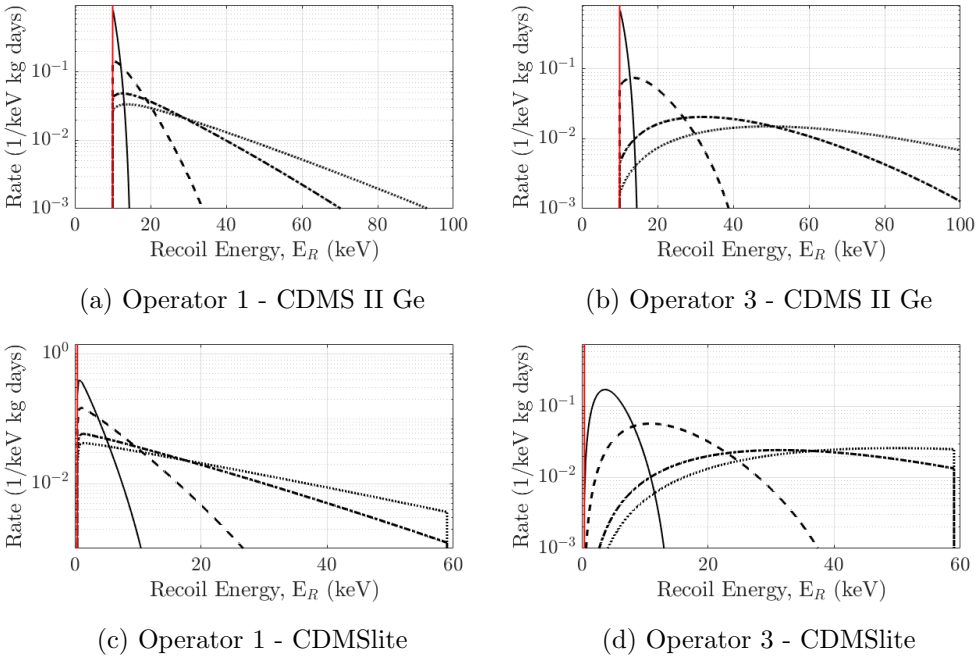

(a) Operator 1 - CDMS II Ge

(b) Operator 3 - CDMS II Ge

(c) Operator 1 - CDMSlite

(d) Operator 3 - CDMSlite

Figure 5.5: Examples of the two spectral shapes of the EFT operators for CDMS II Ge (top) and CDMSlite (bottom) using an isoscalar interaction normalized to 1 event. Operator 1 (left) is an example of the exponential-decay shape also seen in operators 4, 7, and 8. Operator 3 (right) is an example of the beta-distribution shape of also seen in operators 5, 6, 9, 10, and 11. Each shape is shown for four masses in black: 10 GeV (solid line), 20 GeV (dashed line), 50 GeV (dot-dashed line), and 100 GeV (dotted line). The experimental energy threshold is shown in red.

Comparing the shapes between between CDMS II Ge and CDMSlite shows the effect of the threshold on the spectral shape. Not only does it allow access to lower WIMP masses, but it allows for better distinction between shapes. For example, the spectral shape for the 10 GeV mass WIMP (solid black line) of Figures 5.5a and 5.5b show very little difference in shape. Because shape distinction is only possible further from the experimental threshold, lowering the threshold allows for discrimination down to lower masses.

The mass dependence of the spectral shapes in Figure 5.5 also show the upper limit of the prior probability distributions for mass that can be used in a likelihood analysis.

For CDMSlite, the operators of both shapes are cut off by the 60 keV upper limit on the efficiency somewhere around or before $m_\chi = 50$ GeV. Therefore, the highest allowed mass in the prior probability distribution of a likelihood analysis of CDMSlite should be around $m_\chi = 50$ GeV in order to keep the theoretical spectra within the energy region used to compare to the experimental data.

5.2 3D Analysis of CDMS II and LUX

The EFT analysis methodology described in Section 4.2 can be used to present new interpretations of previously published WIMP search results. To demonstrate this, consider three past results obtained using experiments with different target materials: Cryogenic Dark Matter Search (CDMS) experiment observed three WIMP candidate events using silicon detectors [56] and two using germanium detectors [148], while the Large Underground Xenon (LUX) experiment observed one candidate WIMP event using a liquid xenon detector [149]. While not the most recent results in the field, they were chosen to illustrate an example of a tension between different experiments. All three measurements assumed an isoscalar spin-independent interaction (cross section, σ_1^0) and published results for a range of WIMP masses (m_χ) based on detected nuclear recoil events. The energies of the detected events, total exposure, and expected background for each experiment are shown in Table 5.1. A comparison of the exposures of each experiment, including the efficiencies and energy thresholds, is shown in Fig. 5.6.

Using these parameters, the results obtained by the three experiments were reproduced using the EFT SI operator. Figure 5.7 compares the previously published results to the constraints calculated using the EFT likelihood analysis technique for each experiment over the two-dimensional parameters space of the WIMP mass and the elastic

Experiment	Exposure (kg days)	Events (keV)	Background (counts)
CDMS II Si [56]	140.2	8.2, 9.5, 12.3	0.41±0.48
CDMS II Ge [148]	612	10.81, 12.3	0.64±0.17
LUX [149]	10065.4	∼4.5	0.64±0.16

Table 5.1: Overview of the published results from each of the chosen experiments.

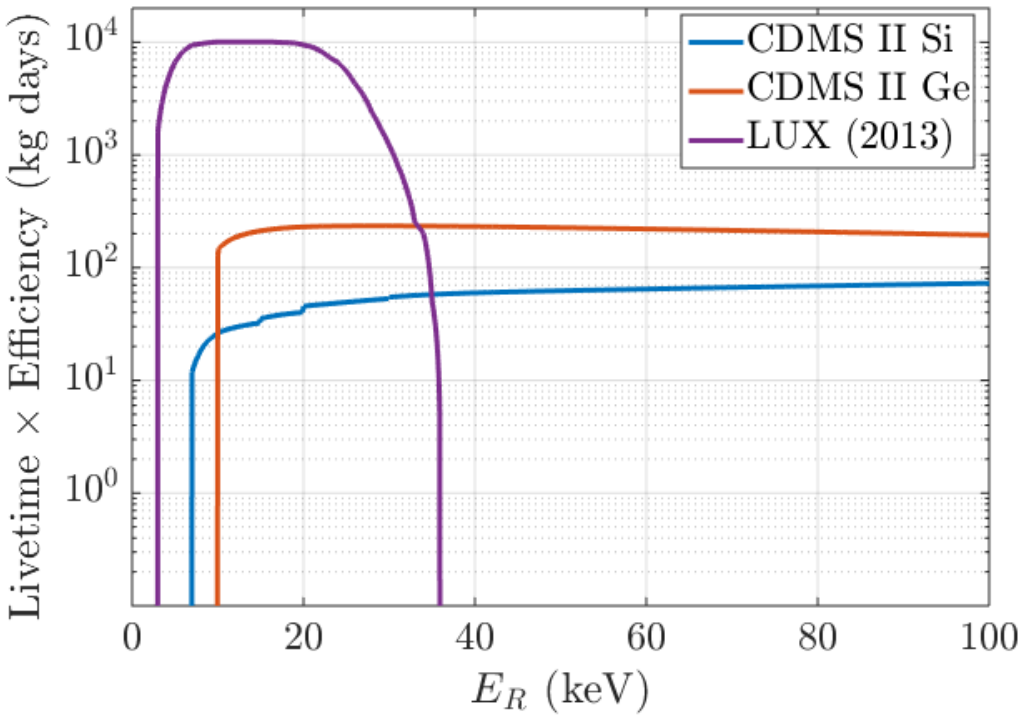

Figure 5.6: Exposures of CDMS II Si [56], CDMS II Ge [148], and LUX [149] as a function of recoil energy including the experimental efficiencies and energy thresholds.

scattering cross section due to the isoscalar component of operator 1, σ_1^0. The published upper limits from all three experiments and the detection contour for the CDMS II Si result are in good agreement with the corresponding constraints obtained with the EFT likelihood analysis. In both cases, the LUX limit, shown in purple, completely excludes the CDMS II Si contour, shown in blue, leading to a visible tension between these experiments in the low mass region. Previous dark matter simulations [126, 139] have shown that assuming the incorrect model for dark matter-target interactions can lead to biased contours and can cause tension between experiments.

The tension between these experiments can be relieved by generalizing the WIMP-nucleus interaction, thus including more EFT operators in the analysis. The simplest addition is the inclusion of the isovector component of $\mathcal{O}_1$ to the SI interaction leading to a likelihood calculated over the 3D parameter space $\{m_\chi, c_1^0, c_1^1\}$. We then marginalize

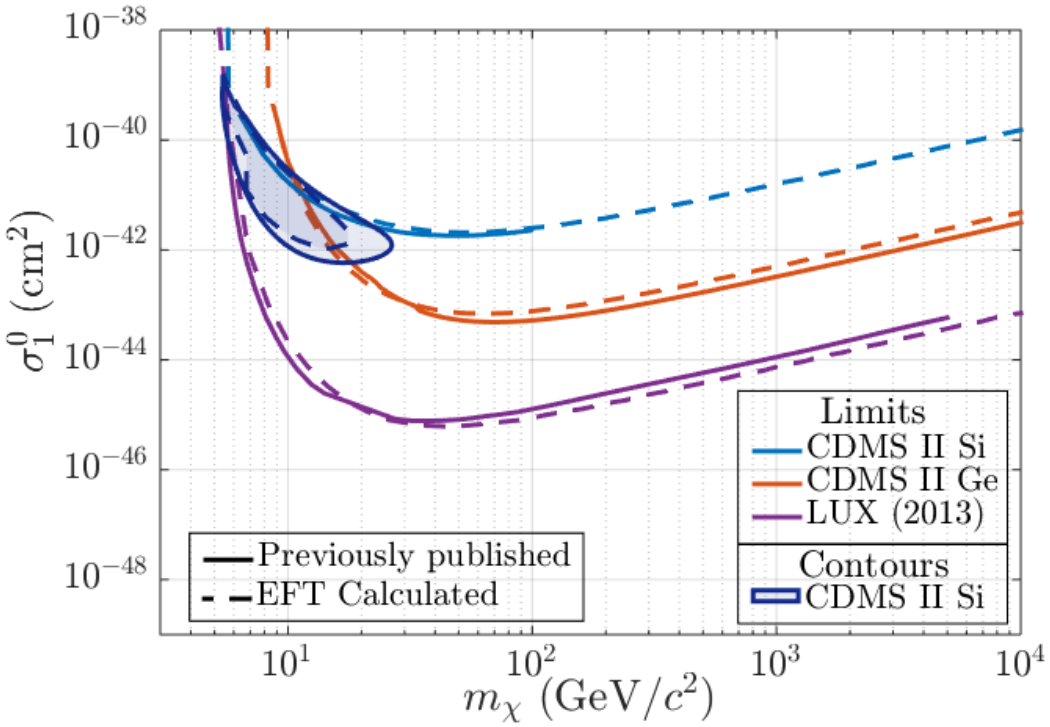

Figure 5.7: EFT 95% upper limit contours for each experiment and the silicon 95% detection contour, which were calculated in a 2D likelihood analysis of WIMP mass and the isoscalar operator 1 cross section, are compared to the published optimal interval contours for the CDMS experiments [56, 148] and to the profile likelihood ratio upper limit from LUX [149]. The LUX limit (purple) rules out the CDMS II Si contour (blue).

over one of the parameters to compute 2D marginalized likelihoods for each experiment individually, as shown in Fig. 5.8. The 95% confidence contours shown for CDMS II Ge and LUX are open contours, consistent with the published LUX and CDMS limits. The symmetries visible in the likelihoods, especially in CDMS II Ge, indicate that the isoscalar and isovector components have the same sign. Combining all three experiments together into a single likelihood makes this symmetry stronger, such that no negative values of the isovector coupling coefficient remain. Figure 5.9 shows the joint likelihood (with all three experiments combined) marginalized over one of the parameters (top row) or over two of the three parameters (bottom row). The cross section is plotted

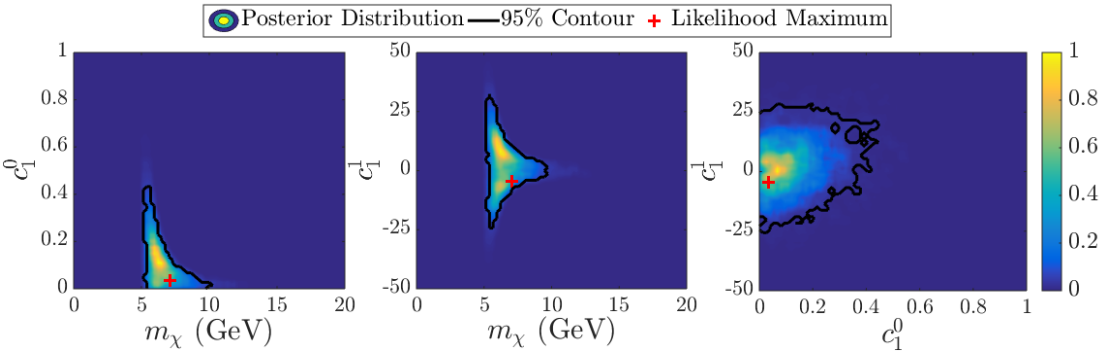

(a) CDMS II Si [56]

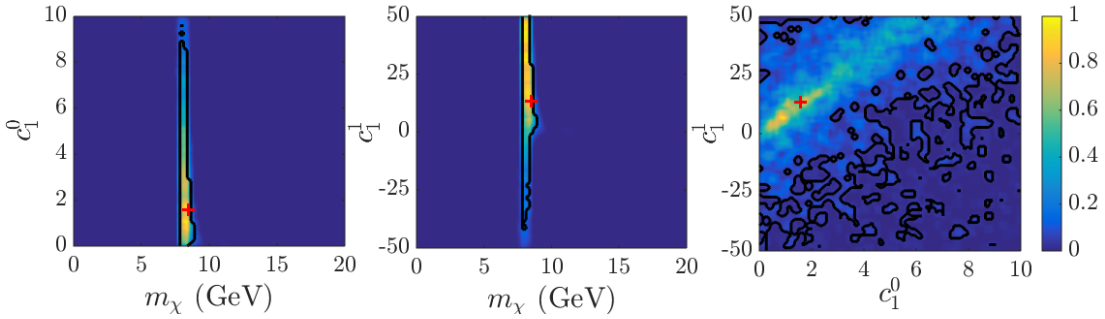

(b) CDMS II Ge [148]

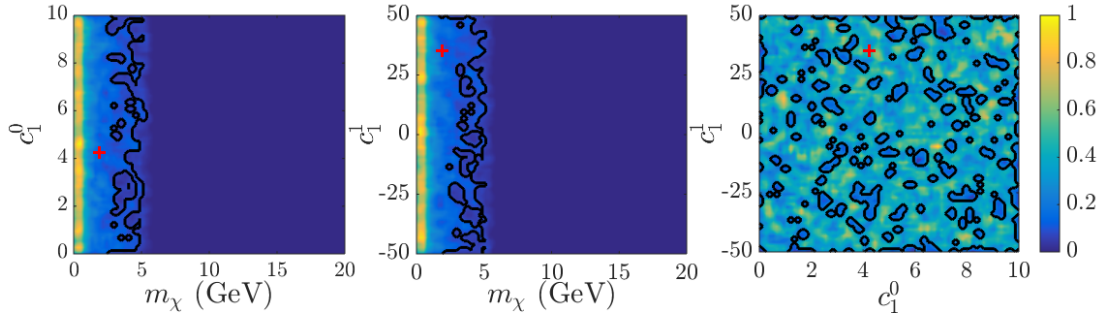

(c) LUX (2013) [149]

Figure 5.8: 2D marginalized likelihoods from the 3D likelihood of each previously published experiment calculated using WIMP mass (m_χ) and both isoscalar (c_1^0) and isovector (c_1^1) coupling coefficient components of operator 1. Contours are calculated at the 95% confidence level, and the global likelihood maximum is depicted.

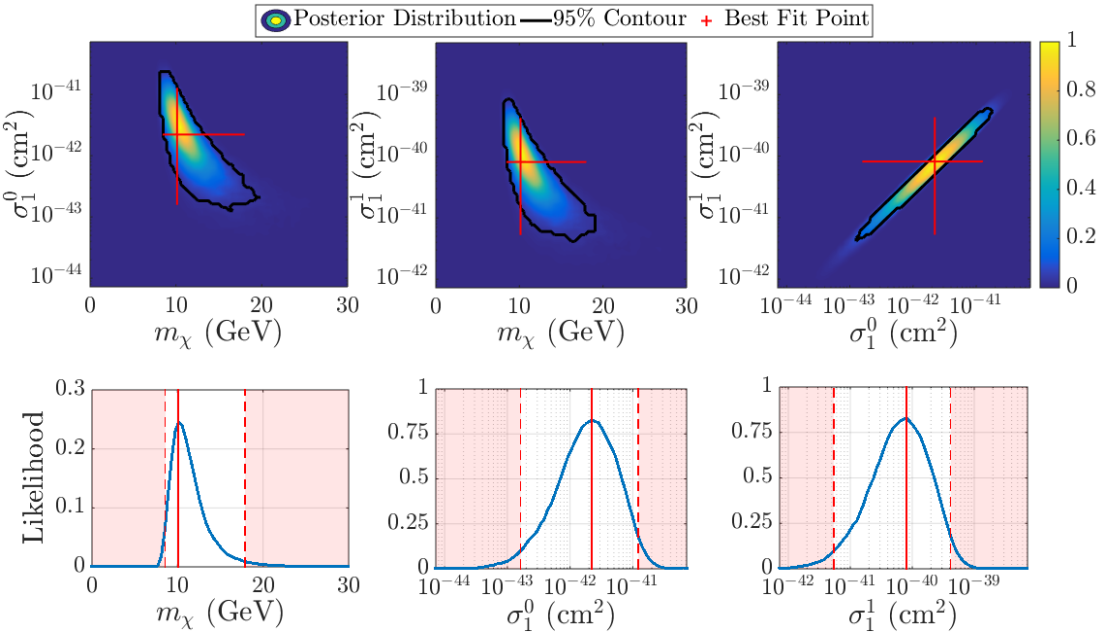

Figure 5.9: Joint 3D likelihood combining CDMS II Si [56], CDMS II Ge [148], and LUX [149] data. Plotted are WIMP mass (m_χ), isoscalar operator 1 cross section (σ_1^0), and isovector operator 1 cross section (σ_1^1). The top row depicts 2D marginalized likelihoods obtained by marginalizing over one of the parameters, while the bottom row shows 1D marginalized likelihoods obtained by marginalizing over two of the three parameters. Also shown are the 95% confidence contours and the point of best fit with error bars derived from the 1D marginalized likelihoods.

instead of the coupling coefficient, defined by

$$\sigma_1^\tau = \frac{(Am_N)^2}{4\pi\langle V\rangle^4(1+A)^2}(c_1^\tau)^2, \tag{5.8}$$

where A is the number of nucleons of the target material and $\langle V\rangle = 246.2$ GeV is the Higgs vacuum expectation value, used here to represent the electroweak scale and to define dimensionless coefficients [135].

The best fit point of the joint likelihood is shown in Fig. 5.9 in red with 95% confidence intervals as calculated from the 1D marginalized likelihoods. The parameters of this point with 95% confidence intervals are $m_\chi = 10.1\pm^{7.8}_{1.5}$ GeV, $\sigma_1^0 = (2.2\pm^{10.1}_{2.1}) \times 10^{-42}$ cm^2, and $\sigma_1^1 = (8.2\pm^{33.2}_{7.6}) \times 10^{-41}$ cm^2. The ratio between coupling coefficients of

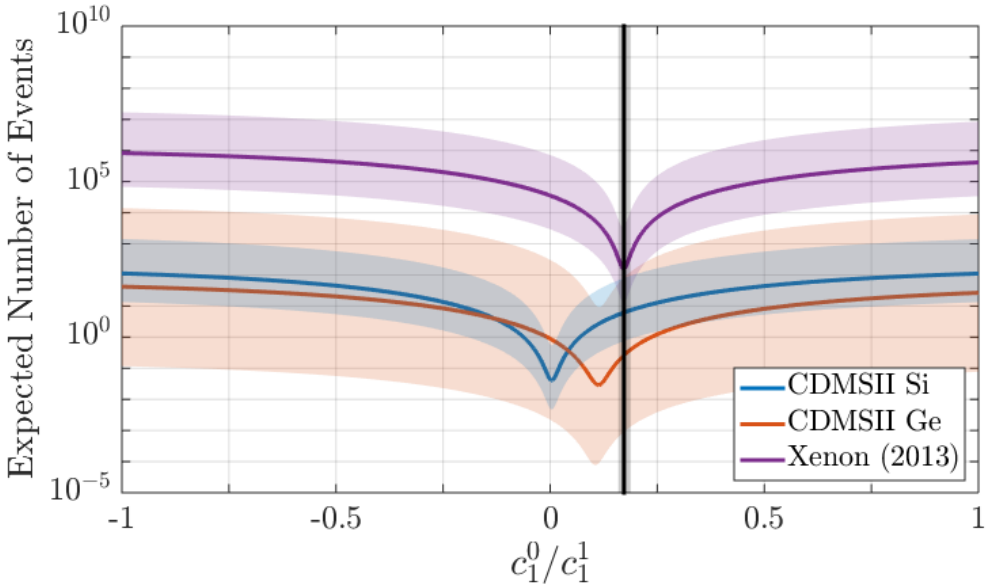

Figure 5.10: Total integrated rate for each experiment over a range of coupling coefficient ratios for $\mathcal{O}_1$ calculated at the best fit mass of $m_\chi = 10.1$ GeV and total coupling coefficient amplitude of $\sqrt{(c_1^0)^2 + (c_1^1)^2} = 0.12\pm^{0.20}_{0.09}$. The minimum for each experiment represents the ratio for which that experiment would detect the fewest number of events. The best fit point of the combined 3D likelihood is shown with 95% confidence errors by the vertical line close to the minimum for LUX. The width of the rate for each experiment was calculated from the 95% confidence regions of the best fit mass and of the total coupling coefficient amplitude.

the best fit point, $c_1^0/c_1^1 = 0.172\pm^{0.016}_{0.013}$, coincides with the point for which the sensitivity of LUX is at the lowest, as shown in Fig. 5.10, showing that the LUX result constrains the combined likelihood the most. The 95% or 2σ confidence contours around the best fit point are closed, as shown in Fig. 5.9; however, at 5σ confidence, the contours are open, so we make no claim of dark matter detection.

The Bayesian evidence can be used to evaluate whether the goodness of fit was improved by adding an isovector component. The evidence for each experiment in both the 2D and 3D analyses are shown in Table 5.2. For each experiment individually the evidence is greater when both coupling components are included, indicating that the

Model	CDMS II Si [56]	CDMS II Ge [148]	LUX [149]
c_1^0 only	3.54×10^{-6}	1.99×10^{-4}	0.00365
c_1^0 and c_1^1	2.84×10^{-5}	4.38×10^{-4}	0.0104
3D / 2D	8.02	2.20	2.84

Table 5.2: Bayesian evidence for each experiment and for the two models: isoscalar spin-independent coupling only (the typically assumed case, 2D) and isoscalar and isovector spin-independent coupling (3D). For all three experiments, the evidence favors coupling via a combination of both isoscalar and isovector couplings as shown by the ratio between the 3D and 2D cases.

3D model is a better fit than the simple 2D WIMP mass and isoscalar coupling model.

5.3 Simulated Dark Matter Data from Future Experiments

Assuming a wrong operator for WIMP-nucleon coupling when conducting an analysis of WIMP search data can lead to erroneous conclusions about the WIMP mass and interactions. Possible failure modes are demonstrated with a set of simulated experiments where the WIMP-nucleon interaction proceeds via nonstandard operators. Three hypothetical direct dark matter experiments are defined. The silicon (Si) and germanium (Ge) experiments are based on the proposed SuperCDMS SNOLAB [46] experiment with backgrounds given by Poissonian errors of 1 count/year for 400 kg of Ge and 0.86 counts/year for 170 kg of Si. The liquid xenon (LXe) experiment is based on the LUX upgrade with a low threshold [150] and background [151] over a live time of 33500 kg days [59]. An overview of the assumed backgrounds, exposures, and energy thresholds is given in Table 5.3. The efficiencies are assumed to be a simple step function between the experimental threshold and the energy at which the experiment's efficiency drops back to 75%.

We present two simulations, one in which the WIMP-nucleon scattering proceeds via EFT $\mathcal{O}_8$ and the other in which the WIMP-nucleon scattering proceeds via $\mathcal{O}_3$. In each case, the values for the WIMP mass and isoscalar and isovector coupling coefficients are chosen in order to compute the theoretical recoil energy spectra for each of the three

Target	Live time (kg days)	Total background (counts)
Si	63000	0.86±0.93
Ge	145000	1±1
LXe	33500	3.5±0.4

Table 5.3: Details used to build the simulated data for each target chosen. Each simulated experiment is assigned an energy threshold of 1 keV. The Si and Ge experiments are based on the proposed SuperCDMS SNOLAB [46], and the LXe on the most recent results from LUX [59, 150, 151].

Benchmark point	m_χ (GeV)	$\{c_1^0, c_1^1\}$	$\{c_3^0, c_3^1\}$	$\{c_8^0, c_8^1\}$
BP_8	3.0	{0,0}	{0,0}	{4.875,24.375}
BP_3	8.0	{0,0}	{16, -6.4}	{0,0}

Table 5.4: WIMP mass and coupling coefficients for $\mathcal{O}_1$, $\mathcal{O}_3$, and $\mathcal{O}_8$ as benchmark points to simulate the detected dark matter data.

simulated experiments. The parameters chosen for each benchmark experiment are listed in Table 5.4. Treating the recoil energy spectra as probability density functions, we randomly draw WIMP-event recoil energies, with the number of events in each simulated experiment given by the integral of the theoretical recoil energy spectrum. The energies of the simulated background events were randomly drawn from a flat probability density function over the energy range set by the efficiency. The simulated dark matter events and simulated background events together were used as the detected events for each simulated experiment.

5.3.1 5D Analysis of Data Simulated in Operator 8

The EFT operator $\mathcal{O}_8$, described by $\vec{S}_\chi \cdot \vec{v}^\perp$, is dependent on the WIMP spin (here assumed to be S_χ=1/2), the transverse component of relative velocity ($\vec{v}^\perp$), and spin-independent and angular-momentum-dependent target nuclear responses. The spin-independent nuclear response is the same as that found in the standard SI interaction, $\mathcal{O}_1$ [133]. Therefore, $\mathcal{O}_8$ and $\mathcal{O}_1$ have the same exponential recoil energy spectral shape; however, the overall rate depends on the WIMP mass and does so differently depending

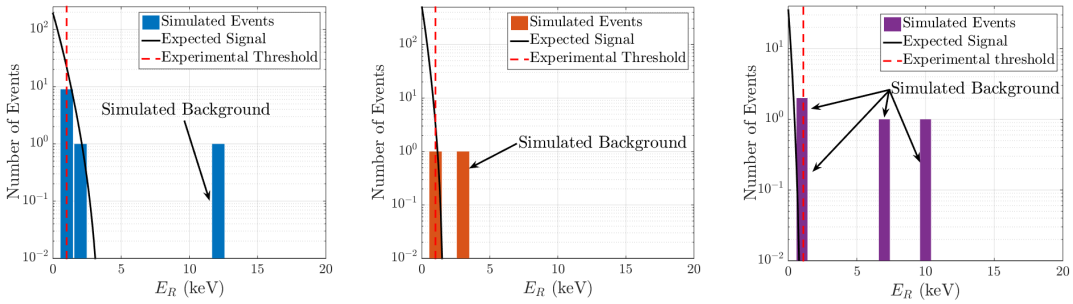

(a) Si (b) Ge (c) LXe

Figure 5.11: The total (signal plus background) recoil energy spectra simulated for each experiment compared to the expected rates of WIMP-nucleon scattering for the chosen interaction parameters in the $\mathcal{O}_8$ simulation (BP_8). The dashed line indicates the energy threshold used in the simulation.

on the target material. This operator was chosen in order to illustrate the challenge of identifying the correct WIMP-nucleon interaction operator when the operator yields similar recoil energy spectral shape to $\mathcal{O}_1$, and the only target-dependent modifier is the overall integrated rate.

We consider the benchmark point, BP_8, with parameters as defined in Table 5.4. This example was chosen specifically to produce a distinctive signal in Si but not in Ge or LXe. The chosen ratio of isoscalar to isovector components, $c_8^0/c_8^1 = 0.2$, favors interactions with Si over Ge. Also, the low WIMP mass of 3 GeV is below the experimental threshold assumed for LXe. For exposures considered in Table 5.3, this resulted in 11, 1, and 0 events for Si, Ge, and LXe, respectively. This corresponds to 12, 2, and 4 events when the background is included.

The simulated WIMP events for the three experiments are shown in Fig. 5.11. All of the simulated events for Ge sit right at the experimental threshold, so very little shape information is available. On the contrary, for Si some simulated WIMP events pass the experimental threshold, so the shape information should be more helpful in distinguishing between operators. Even though all of the simulated data for LXe are background events, they mimic the energy distribution of an exponentially decaying WIMP spectrum, which allows the background events to be easily misinterpreted as a

Reconstructed point	m_χ (GeV)	$\{c_1^0, c_1^1\} \times 10^3$	$\{c_8^0, c_8^1\}$
BP_8 in $\mathcal{O}_1$	2.0 (1.5, 4.0)	$\{1, 30\}$ $\{(0, 20), (-860, 900)\}$	...
BP_8 in $\mathcal{O}_8$	2.4 (1.9, 3.7)	...	$\{5, 16\}$ $\{(3, 19), (-92, 94)\}$
BP_8 in $\mathcal{O}_1$ and $\mathcal{O}_8$	2.03 (1.56, 2.85)	$\{2, 30\}$ $\{(0, 18), (-820, 870)\}$	$\{0, -\}$ $\{(-18, 18), (-95, 95)\}$

Table 5.5: Best fit points with 95% confidence regions for the 3D and 5D reconstructions of the benchmark point BP_8 of Table 5.4, based on 1D marginalized likelihoods. As noted in the header, $\mathcal{O}_1$ coupling coefficients have been enlarged by 10^3.

WIMP signal.

We start by analyzing the simulated data in the EFT likelihood formalism assuming $\mathcal{O}_1$ interaction only; that is, the likelihood is computed over the 3D parameter space of $\{m_\chi, c_1^0, c_1^1\}$. The resulting 3D likelihood is shown in Fig. 5.12a with the 2D marginalized likelihoods shown on top and the 1D marginalized likelihoods on the bottom. The best-fit point, which is calculated from the 1D marginalized likelihoods and is listed in Table 5.5, is also depicted along with the error bars. The point representing the simulated data ($c_1^0 = 0, c_1^1 = 0$) is contained within the 1D 95% confidence intervals but not in two of the 2D 95% confidence contours. For example, the c_1^0 vs. c_1^1 contour plot on the far top right of Fig. 5.12a shows that the simulated point is not contained within the 95% confidence contour. This example demonstrates the fact that marginalizations to one dimension, with their necessary loss of information, can be misleading. The 2D representation must be used in order to develop a better understanding of the parameter space. In this particular simulation the 2D marginalized likelihoods indicate that nonzero $\mathcal{O}_1$ couplings are needed in order to explain the simulated data. This, of course, is not consistent with the assumed simulation parameters, and it is a consequence of the fact that a wrong operator was used to analyze the data. In other words, assuming the wrong operator when calculating the likelihood can lead to reasonable 2D contours that do not represent the true (in this case, simulated) nature of dark matter.

This analysis is then repeated assuming $\mathcal{O}_8$ interaction only, and the likelihood is

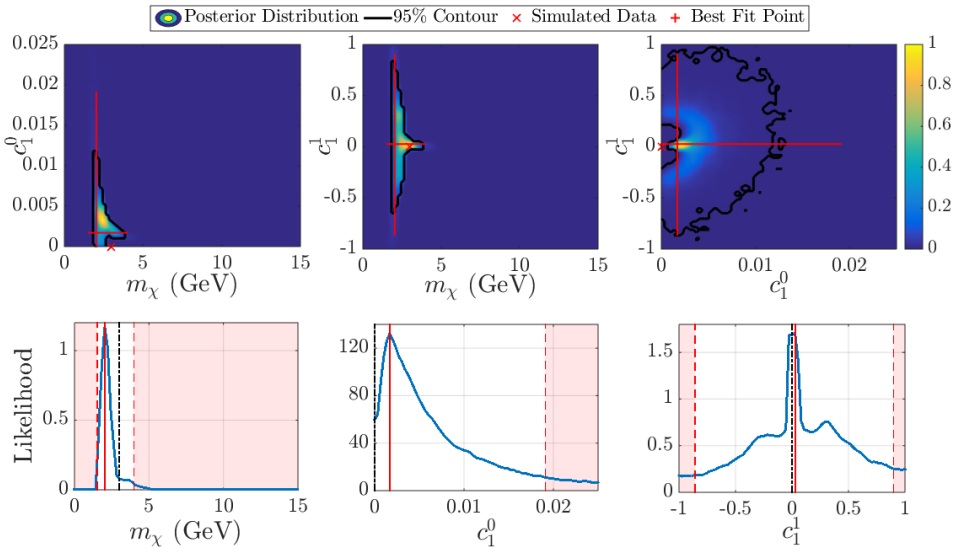

(a) $\mathcal{O}_1$ recovery

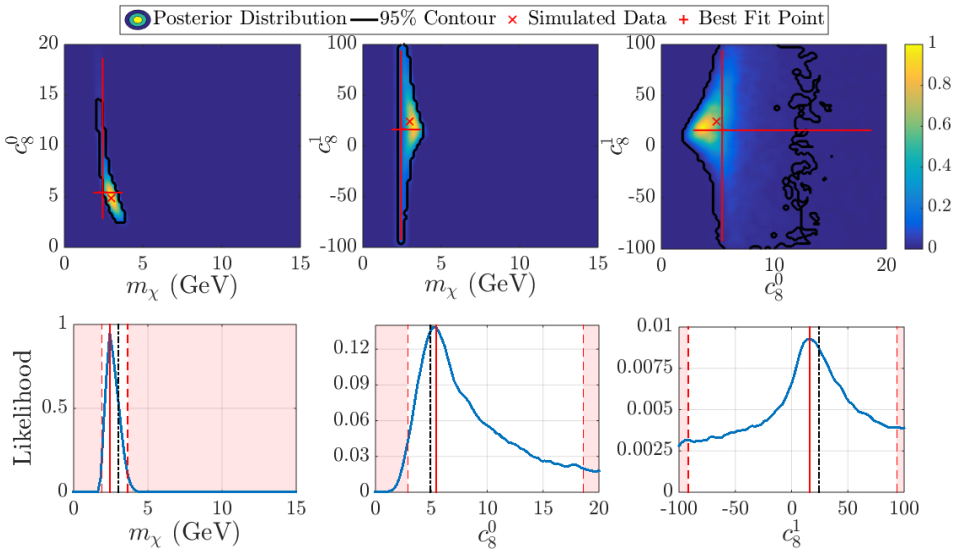

(b) $\mathcal{O}_8$ recovery

Figure 5.12: 3D likelihoods of the data simulated using BP_8 and analyzed under the assumption of $\mathcal{O}_1$ (top) or $\mathcal{O}_8$ (bottom) for all three experiments combined. For each recovery operator, the top row of plots shows 2D marginalized likelihoods and the bottom row shows the 1D marginalized likelihoods. Also shown is the point representing the simulated data, marked by x in 2D and a black dashed line in 1D and the best fit point represented by the red + in 2D and red vertical line in 1D.

computed over the 3D parameter space of $\{m_\chi, c_8^0, c_8^1\}$, as shown in Fig. 5.12b. In this case, the simulated point is well within the 95% confidence 2D contours and 1D intervals, as one would expect since this recovery assumes the correct operator. The resulting likelihood is well defined in WIMP mass and isoscalar coupling coefficient but less so in the isovector component. The 95% confidence intervals computed from 1D marginalized likelihoods are also shown in Table 5.5. These intervals were calculated using the joint (Si, Ge, and LXe) likelihood and are tighter than for any single experiment alone. Specifically, since Si detected the largest number of events (11 events versus 1 for Ge and 0 for Xe), the Si-only likelihood is expected to best match the results of the joint likelihood. However, the widths of the 95% confidence contours were ~ 1.4 times larger for Si alone than for the joint likelihood case, demonstrating that combining experiments tightens the resulting contours.

Additional information can be gleaned from the Bayesian evidence. From the 3D likelihoods, the evidence for $\mathcal{O}_1$ is 2×10^{-9}, whereas the evidence for $\mathcal{O}_8$ is 3 times larger at 6×10^{-9}. This shows that $\mathcal{O}_8$ is the better fit to this data.

In the proposed procedure for analysis of WIMP search data, step 3 proposes a likelihood analysis in higher-dimensional parameter space including operators with the highest evidences in 3D likelihood analyses. Applying this approach to our simulation, we perform the EFT likelihood analysis of the 5D parameter space $\{m_\chi, c_1^0, c_1^1, c_8^0, c_8^1\}$. The results are shown in Fig. 5.13 with the 2D marginalized likelihoods on the top and the 1D marginalized likelihoods on the bottom. The 1D marginalizations of the 5D likelihood were calculated from six different 3D subspaces and averaged together to give one 1D likelihood. The six marginalizations from different 3D subspaces are plotted in varying colors in Fig. 5.13 (bottom) with the averaged curve in black. Note that all marginalized likelihoods (for a given parameter) are similar, indicating that the possible systematic error in this marginalization procedure is not significant.

The parameters of the best fit point calculated from the 1D likelihoods are found in Table 5.5. Note that the open contour for c_8^1 implies a flat spectrum with no discernible peak. The simulated data point is contained within all of the 95% confidence intervals except for WIMP mass. The WIMP mass sits just outside the 95% confidence (or 2σ confidence) contour at 2.4σ or at 1.6% probability of occurring. One factor that could contribute to this are the two LXe background events just above threshold that mimic

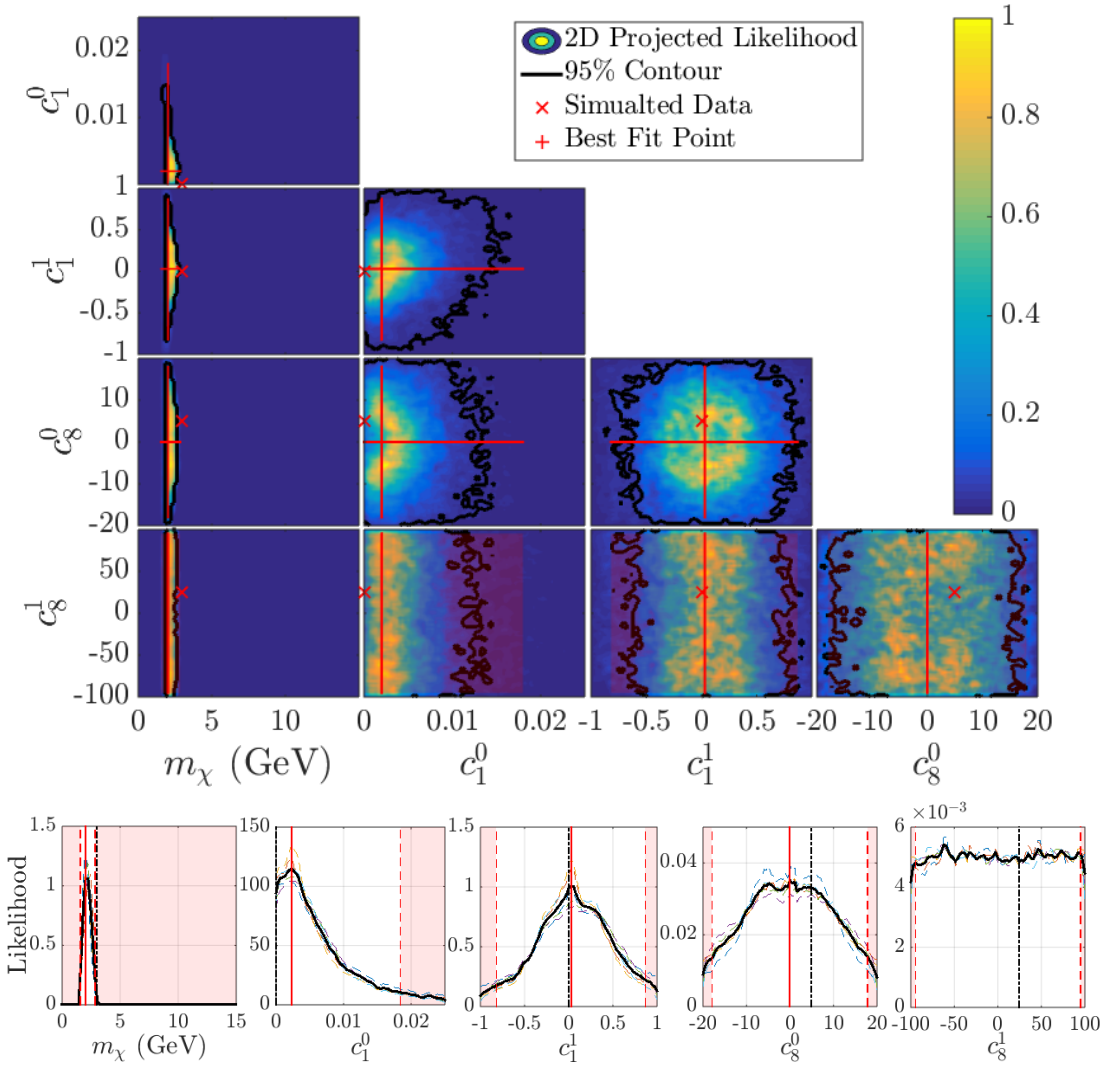

Figure 5.13: 5D likelihood of the data simulated in $\mathcal{O}_8$ and recovered assuming interactions in both $\mathcal{O}_1$ and $\mathcal{O}_8$, for all three experiments combined. The 95% confidence contours in 2D marginalized likelihoods are shown on the top and the 1D marginalized likelihoods are shown in the bottom row of plots. The multiple colors in the 1D plot represent the marginalizations of the six subspaces and the black line the averaged. Also shown is the point representing the simulated data, marked by x in 2D and a black dashed line in 1D and the best fit point represented by the red + (or shaded red region) in 2D and red vertical line in 1D.

a low mass WIMP.

Since the spectral shapes for $\mathcal{O}_1$ and $\mathcal{O}_8$ are both exponentially decaying, it is difficult to separate the four coupling coefficients from each other using only three target materials. This is most apparent in the 1D projections of the likelihood, where the peaks of c_1^1 and c_8^0 are very wide, and the likelihood for c_8^1 is completely flat. In other words, although the 5D likelihood analysis detects the WIMP and places a strong constraint on the WIMP mass (consistent with the simulated WIMP mass), it cannot constrain the individual couplings in $\mathcal{O}_1$ and $\mathcal{O}_8$ due to their degeneracies. Additional experiments with different targets would be needed to break these degeneracies.

5.3.2 5D Analysis of Data Simulated in Operator 3

The EFT operator $\mathcal{O}_3$ is given by $i\vec{S}_N \cdot (\vec{q} \times \vec{v}^{\perp})$, has no dependence on the WIMP spin, and relies on two nuclear responses of the target: a spin-dependent response (transverse to the momentum transfer) and a spin-and-angular-momentum-dependent response [133]. Therefore, the event rate spectrum of $\mathcal{O}_3$ has a different shape than that of $\mathcal{O}_1$. In particular, the event rate spectrum for $\mathcal{O}_1$ smoothly decays exponentially with recoil energy, while for $\mathcal{O}_3$, even with no experimental efficiencies included, the event rate is suppressed at low energies with a pronounced peak at higher energies, as shown in Fig. 5.14. The energy and amplitude of the peak is dependent on the WIMP mass, the combination of coupling coefficients, and the target chosen. This operator was chosen to demonstrate how differences in the shape of recoil energy spectra can be used to improve parameter estimation.

The three benchmark experiments (Ge, Si, LXe) are simulated in the $\mathcal{O}_3$ framework using the benchmark point BP_3 listed in Table 5.4 with the ratio of isoscalar and isovector components of $c_3^0/c_3^1 = -2.5$. For the simulated exposures and energy ranges described in Table 5.3, Si detected three WIMP events, Ge detected 19 events, and LXe detected 21 events. Including the simulated background, the total number of simulated detected events for each experiment is 4, 20, and 25 events respectively. The simulated data compared to the expected recoil energy spectra for each experiment are shown in Fig. 5.14.

The numbers of simulated events for Ge and LXe (Fig. 5.14) are large enough to distinguish between the spectral shapes of $\mathcal{O}_3$ and $\mathcal{O}_1$. Si (also Fig. 5.14) has a low

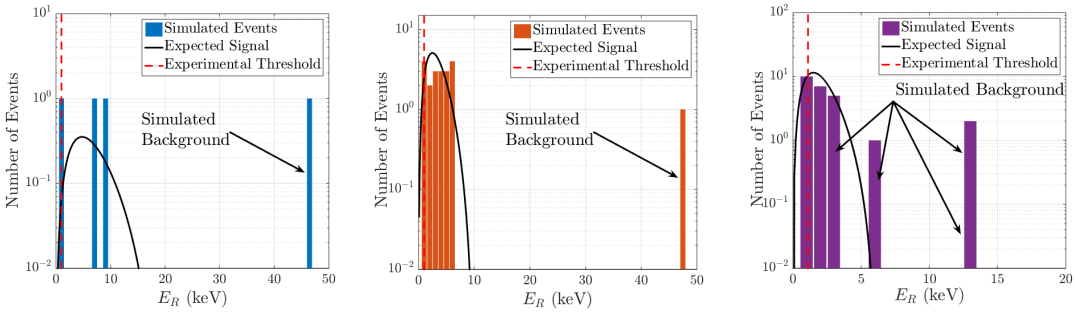

(a) Si (b) Ge (c) LXe

Figure 5.14: The total (signal plus background) simulated data for each experiment compared to the expected recoil energy spectra of WIMP-nucleon scattering for the chosen $\mathcal{O}_3$ interaction parameters using BP_3. The dashed line indicates the energy threshold used in the simulation.

number of simulated events such that little information on the spectral shape is available. However, the relatively large range of recoil energies points to the nature of the underlying spectrum; for an exponentially decaying spectrum, most of the WIMP events would be expected to cluster at the experimental threshold.

As in the case of $\mathcal{O}_8$ above, we use 3D EFT likelihood analyses to test steps 1 and 2 of the proposed analysis procedure. The 3D likelihood is first computed assuming that the WIMP-nucleon scattering proceeds via the standard SI operator, that is over the parameter space $\{m_\chi, c_1^0, c_1^1\}$. This is then contrasted with the likelihood computed assuming the correct scattering operator, that is over the parameter space $\{m_\chi, c_3^0, c_3^1\}$. Both likelihoods are joint, combining all three simulated experiments (Si, Ge, and LXe). Figure 5.15a shows the 2D marginalized likelihoods (top) and the 1D marginalized likelihoods (bottom) assuming the $\mathcal{O}_1$ interaction. In both the 2D and 1D marginalized likelihoods, the simulated data point represented by $\{m_\chi, c_1^0, c_1^1\} = \{8.0\ \mathrm{GeV}, 0, 0\}$ is not included in the 95% confidence contours/intervals. That is, these contours do not accurately represent the underlying nature of the simulated dark matter, which is a consequence of assuming the wrong interaction operator in the analysis. The parameter values of the point of maximum likelihood with 95% confidence intervals calculated from the 1D marginalized likelihoods are shown in Table 5.6.

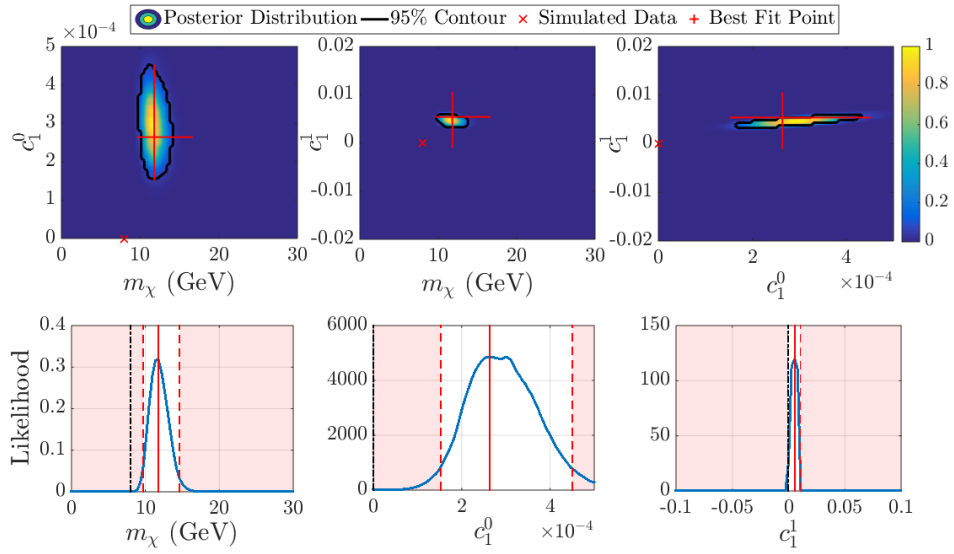

(a) $\mathcal{O}_1$ recovery

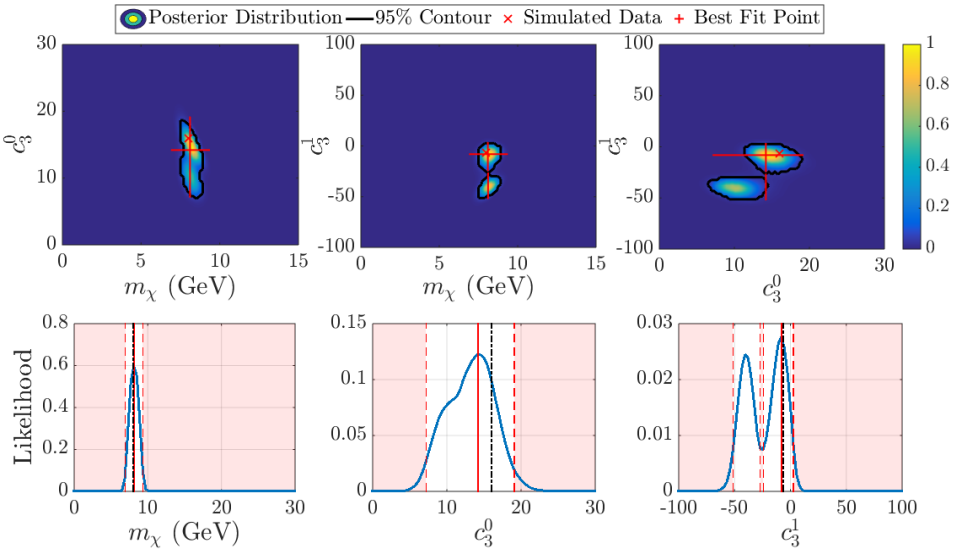

(b) $\mathcal{O}_3$ recovery

Figure 5.15: 3D likelihoods of the data simulated using BP_3 and analyzed under the assumption of $\mathcal{O}_1$ (top) or $\mathcal{O}_3$ (bottom) for all three experiments combined. For each recovery operator, the top row of plots shows 2D marginalized likelihoods and the bottom row shows the 1D marginalized likelihoods. Also shown is the point representing the simulated data, marked by x in 2D and a black dashed line in 1D and the best fit point represented by the red + in 2D and red vertical line in 1D.

Reconstructed point	m_χ (GeV)	$\{c_1^0, c_1^1\} \times 10^3$	$\{c_3^0, c_3^1\}$
BP$_3$ in $\mathcal{O}_1$	11.8 $(9.7, 14.6)$	$\{0.26, 5.4\}$ $\{(0.15, 0.45), (-0.9, 10.4)\}$	...
BP$_3$ in $\mathcal{O}_3$	8.1 $(7.0, 9.3)$	...	$\{14.2, -8\}$ $\{(7.2, 19.2),$ $(-51, -27) \cup (-24, 3)\}$
BP$_3$ in $\mathcal{O}_1$ and $\mathcal{O}_3$	8.1 $(6.9, 9.7)$	$\{0.13, 0.5\}$ $\{(0.00, 0.42), (-5.3, 4.2)\}$	$\{15, -8\}$ $\{(-21, 0) \cup (4, 28),$ $(-62, -29) \cup (-27, 54)\}$

Table 5.6: Best fit points with 95% confidence regions for the 3D and 5D reconstructions of the benchmark point BP$_3$ of Table 5.4, based on 1D marginalized likelihoods. As noted in the header, $\mathcal{O}_1$ coupling coefficients have been enlarged by 10^3.

If instead the analysis assumes the same operator as the simulation (in this case $\mathcal{O}_3$), the 95% confidence contours include the simulated data point $\{m_\chi, c_3^0, c_3^1\} = \{8.0 \text{ GeV}, 16, -6.4\}$ as shown in Fig. 5.15b by the 2D marginalized likelihoods (top) and 1D marginalized likelihoods (bottom). Even though two regions of high likelihood are visible in each 2D marginalized likelihood, the likelihood favors the region that contains the simulated data point. Additionally, the point of maximum likelihood agrees closely with the simulated data point. This is also shown numerically in Table 5.6. Bayesian evidence further supports the hypothesis that the operator $\mathcal{O}_3$ fits the simulated data better than $\mathcal{O}_1$: the evidence calculated for $\mathcal{O}_3$ is 2×10^{-18}, about 20 times higher than for $\mathcal{O}_1$ at 1×10^{-19}. This indicates that the simple Bayesian evidence measure can be used to compare recoveries with different assumed operators in order to determine which operator(s) perform best in terms of explaining the observed data from multiple experiments.

Both 3D likelihoods shown in Fig. 5.15 were calculated by combining all three experiments into a single likelihood, resulting in better-defined contours than for any individual experiment. Even when the likelihood for each experiment individually is fairly flat over the entire prior range, such as for c_3^0 from the 3D likelihood assuming $\mathcal{O}_3$

interaction, combining experiments can create a closed contour for the coupling coefficient, as shown in Fig. 5.15b. Unfortunately, it is also possible to obtain closed contours when combining experiments for a likelihood calculated by assuming the wrong EFT operator, which stresses the importance of considering the Bayesian evidence.

The Ge and LXe experiments detected many more events than Si, with 19 and 21 respectively, compared to only three for Si. The 95% confidence intervals calculated for the joint likelihood assuming $\mathcal{O}_3$ interaction, shown in Table 5.6, are, on average, 1.4 times tighter than for Ge only and 4.3 times tighter than for LXe only. Since there were more simulated data events in LXe than in Ge, it might be expected that the LXe contours would be the closest to the joint likelihood. However, due to the flatness of the $\mathcal{O}_3$ likelihood in LXe for the isovector coupling coefficient, c_3^1, the average between the three 2D marginalized likelihoods is slightly higher than for Ge alone or for Si, Ge, and LXe combined.

As suggested in step 3 of the proposed analysis procedure, computing the 5D likelihood for both $\mathcal{O}_1$ and $\mathcal{O}_3$ should help differentiate between the two operators by allowing constraints to be set simultaneously for both operators. Since the simulation assumed only nonzero components in $\mathcal{O}_3$, the $\mathcal{O}_1$ coupling coefficient contours should include zero, which was the simulated value of those parameters. For the $\mathcal{O}_8$ simulation, the 5D likelihood including $\mathcal{O}_1$ and $\mathcal{O}_8$ ended up being overparameterized due to the similar recoil energy spectral shapes for all four of the coupling coefficients involved and due to the low number of simulated data points. The $\mathcal{O}_3$ simulation has the advantage of having more simulated WIMP events and different spectral shapes for $\mathcal{O}_1$ and $\mathcal{O}_3$. We compute the 5D likelihood over the parameter space $\{m_\chi, c_1^0, c_1^1, c_3^0, c_3^1\}$ and show the 2D marginalized likelihoods (top) and the 1D marginalized likelihoods (bottom) in Fig. 5.16. The 1D marginalized likelihoods were computed in the same manner as for $\mathcal{O}_8$. Unlike the $\mathcal{O}_8$ simulation, none of the parameters in the 5D analysis have a flat likelihood. Hence, the simulated data point is better recovered, and it is fully contained within all of the 2D 95% confidence contours and 1D 95% confidence intervals.

Table 5.6 shows the value of the point of highest likelihood with the 95% confidence intervals as calculated from the 1D marginalized likelihoods. The simulated data point is well contained within all of the 95% confidence intervals and is closer to the point of maximum likelihood than suggested by the width of these intervals. In this instance,

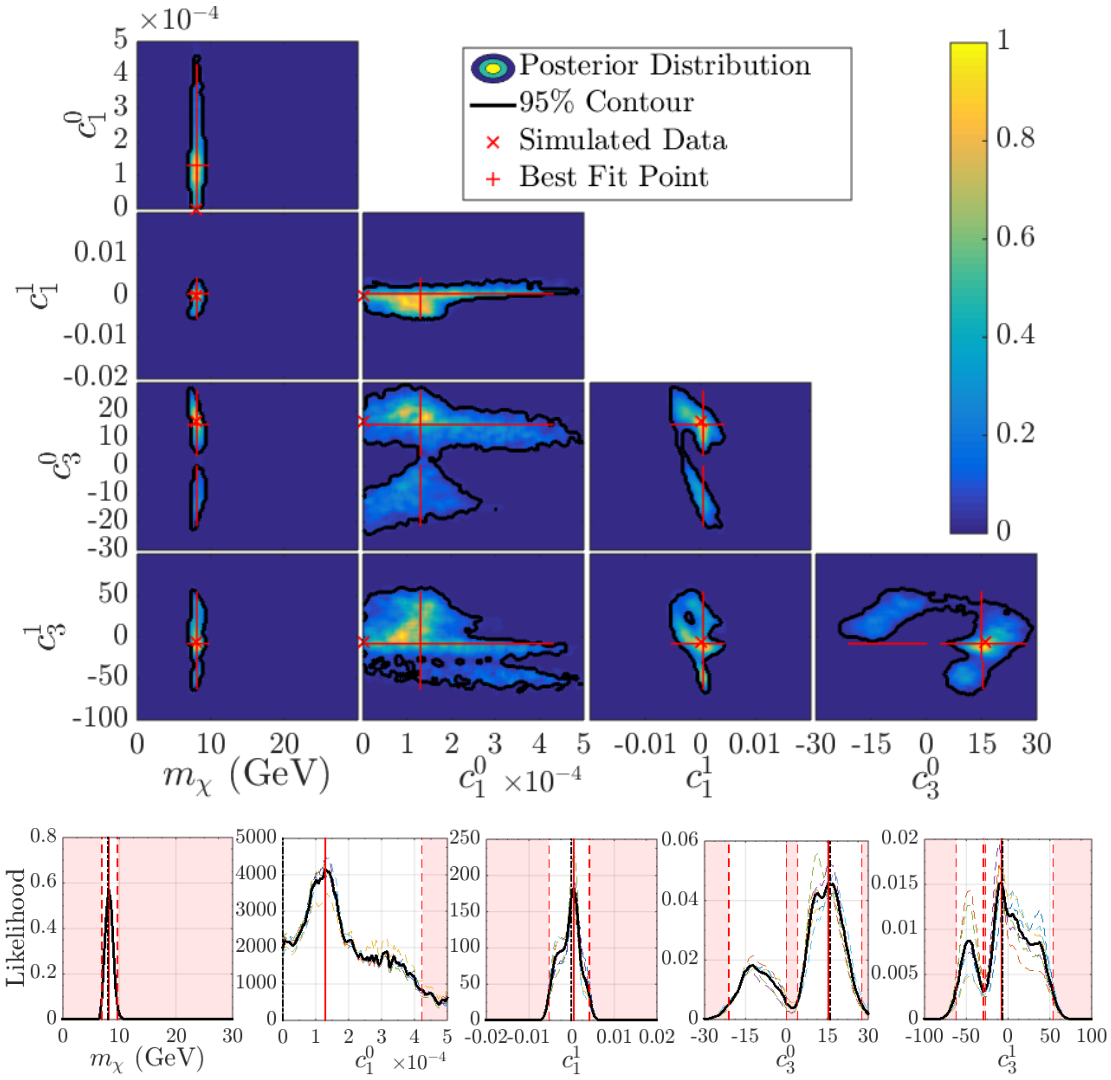

Figure 5.16: 5D likelihood of the data simulated in $\mathcal{O}_3$ and computed assuming WIMP-nucleon interaction in $\mathcal{O}_1$ and $\mathcal{O}_3$, for all three experiments combined. The 95% confidence contours in 2D marginalized likelihoods are shown on the top and the 1D marginalized likelihoods are shown in the bottom row of plots. The multiple colors in the 1D plot represent the marginalizations of the six subspaces and the black line the averaged. Also shown is the point representing the simulated data, marked by x in 2D and a black dashed line in 1D and the best fit point represented by the red + in 2D and red vertical line in 1D.

the 5D likelihood was able to successfully fit the simulated values of WIMP mass and coupling coefficients. The point of highest likelihood is very similar to that of the 3D $\mathcal{O}_3$ likelihood, but as expected by the increase in the number of parameters, the 95% confidence intervals are larger for the 5D than for the 3D likelihood.

Chapter 6

Full EFT Analysis of CDMSlite

6.1 CDMSlite Run 2 Analysis

CDMSlite Run 2, which ran at the Soudan Underground Laboratory in northern Minnesota in 2014, used a single ($\sim$ 600 g) Ge crystal. Results from this run were previously published up to 20 keV_{ee} (electron equivalent energy) or $\sim$ 60 keV_{nr} (nuclear recoil energy). This previous analysis assumed an isoscalar spin-independent interaction and was analyzed using the Optimum Interval method with no background subtraction [48, 77]. Here, the CDMSlite Run 2 data was analyzed in the full EFT framework using a Bayesian likelihood method.

In order to analyze the CDMSlite Run 2 results, the total exposure (WIMP detection efficiency $\times$ live time), background models, and binned recoil energy spectra must be defined. The data spectrum here uses all CDMSlite Run 2 events passing data quality and fiducial cuts from the experimental threshold of 0.304 keV_{nr} up to 60 keV_{nr} binned into 300 energy bins ($\Delta E \approx 0.2\ \text{keV}_{\text{nr}}$). For this analysis, in order to mitigate high errors in the background models around known activation peaks, energy regions around each peak have been removed from the analysis. The resulting data spectrum, efficiency, and remaining background models are shown in Figure 6.1. For further discussion on the efficiency and data spectrum see Agnese *et al.* [152]. The backgrounds included in the analysis are the continuous recoil energy spectra due to the tritium decay and Compton scattering. Additional backgrounds from contaminations and additional activation peaks exist in the CDMSlite data set; however, the peaks from these contributions are

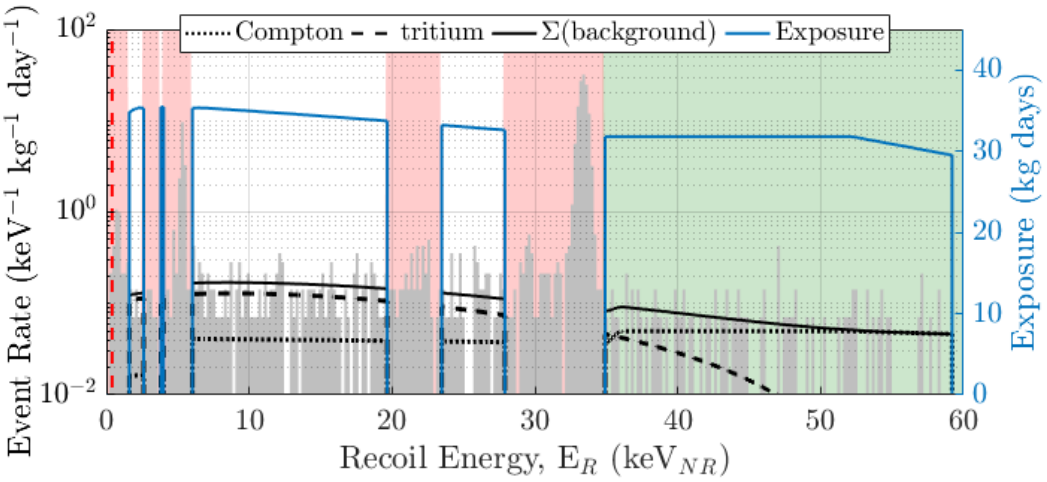

Figure 6.1: CDMSlite Run 2 detected events (light gray) and exposure (blue) with removed regions (red) and remaining background sources (dotted black = Compton, dashed black = tritium, solid black = total background). The green shaded region designates the region used to determine the ratio between Compton and tritium backgrounds. The amplitudes of the background models shown here were chosen to show the shapes of the spectra and do not represent the best fits to the data.

below the sensitivity of the experiment and not clearly visible in the data set, so models for these backgrounds were not included in this analysis.

The removed regions are defined as within 5σ of the K-shell, L-shell, and M-shell peaks for ^{71}Ge, ^{68}Ge, ^{68}Ga, ^{65}Zn, ^{55}Fe, and ^{54}Mn. The detail of how each of these isotopes contribute to the removed regions are listed in Table 6.1. These isotopes were chosen because hints of their characteristic peaks are visible in the CDMSlite Run 2 spectrum. Removing the regions around known activation peaks makes the analysis less susceptible to uncertainties in the activation models and amplitudes. This approach removes the lowest energy events (as indicated in the Region I of Table 6.1), effectively increasing the energy threshold. In order to set more conservative limits, the next highest bin was also removed from the analysis, effectively raising the energy threshold for this analysis to 1.605 keV$_{\mathrm{nr}}$.

The observed energy resolution (σ) of K, L, and M activation peaks and of random

Region	Energy Range (keV_{nr})	Source	Energy (keV_{nr})
1	0 - 1.605	^{54}Mn M-shell	0.40 ± 0.06
		^{55}Fe M-shell	0.44 ± 0.06
		^{65}Zn M-shell	0.63 ± 0.06
		^{68}Ga M-shell	0.71 ± 0.06
		^{68}Ge M-shell	0.80 ± 0.08
		^{71}Ge M-shell	0.80 ± 0.08
2	2.408 - 3.813	^{54}Mn L-shell	3.01 ± 0.09
		^{55}Fe L-shell	3.30 ± 0.09
3	19.46 - 23.68	^{65}Zn L-shell	4.5 ± 0.1
		^{71}Ge L2-shell	4.7 ± 0.1
		^{68}Ga L-shell	4.9 ± 0.1
		^{68}Ge L-shell	5.3 ± 0.1
		^{71}Ge L-shell	5.3 ± 0.1
4	4.013 - 6.020	^{54}Mn K-shell	20.6 ± 0.2
		^{55}Fe K-shell	23.3 ± 0.2
5	27.69 - 35.32	^{65}Zn K-shell	29.1 ± 0.3
		^{68}Ga K-shell	31.4 ± 0.3
		^{68}Ge K-shell	33.4 ± 0.3
		^{71}Ge K-shell	33.4 ± 0.3

Table 6.1: Energies of the removed regions, which were determined at 5σ of the activation peaks from ^{71}Ge, ^{68}Ge, ^{68}Ga, ^{65}Zn, ^{55}Fe, and ^{54}Mn [153].

zero energy events, were determined from a fit to the function

$$\sigma(E_{ee}) = \sqrt{\sigma_0^2 + \epsilon_\gamma F E_{ee} + (A E_{ee})^2}, \tag{6.1}$$

where $\sigma_0 = 9.26 \pm 0.11$ eV_{ee}, F is the Fano factor with $\epsilon_\gamma F = 0.64 \pm 0.11$ eV_{ee}, $A = (5.68 \pm 0.94) \times 10^{-3}$, and E_{ee} is the electron equivalent energy [77]. In order to compare with expected EFT rates, all energies must be converted to the nuclear recoil energy, E_{nr}. The conversion between electron and nuclear recoil is given in Section 2.2.

The main background source outside the removed regions is due to Compton scattering and tritium contamination. These backgrounds were modeled as follows. Due to the discrete binding energy of each electron shell, an energy of a recoiling electron must have at least the binding energy of the shell it came from; therefore, the low energy Compton scattering spectrum has step-like decreases at the energy of each electron shell. In order to include the detector resolution with these steps, the shape of the Compton spectrum [154, 155] is described by error functions as

$$B_C(E_{\rm ee}) = a_C \sum_{j=\rm K,L,M} 0.5 A_j \left(1 + \mathrm{erf}\left(\frac{E_{\rm ee} - \mu_j}{\sqrt{2}\sigma_j}\right)\right), \tag{6.2}$$

where a_C is the amplitude of the Compton spectrum, μ_j and σ_j are the energy and energy resolutions of the Ge K-shell, M-shell, or L-shell activation peaks as listed in Table 6.1, and A_j are the electron shell-dependent constants given as $A_K = 0.0041 \pm 0.0001$, $A_L = 0.015 \pm 0.001$, and $A_M = 0.0345 \pm 0.0006$ as determined by a fit to calibration data [156].

Exposure of the Ge crystals to high-energy cosmic-ray secondary particles causes backgrounds from tritium β^- decay [157]. The emitted electron has a spectral shape given by

$$B_T(E_{\rm ee}) = a_T(Q - E_{\rm ee})^2(E_{\rm ee} + m_e)F(Z_{\rm He}, E_{\rm ee})\sqrt{E_{\rm ee}^2 + 2E_{\rm ee}m_e}, \tag{6.3}$$

where a_B is the amplitude of the tritium spectrum, $Q = 18.6$ keV$_{\rm ee}$ is the endpoint energy of the tritium decay, m_e is the electron mass, and $F(Z_{\rm He}, E_{\rm ee})$ is the Fermi function. Because $Q \ll m_e$,

$$F \simeq \frac{2\pi\eta}{1 - e^{-2\pi\eta}} \tag{6.4}$$

with

$$\eta = \frac{\alpha Z_{\rm He} E_{\rm ee}}{p_{\rm ee}}. \tag{6.5}$$

Here, $\alpha = 1/137$ is the fine structure constant, $Z_{\rm He} = 2$ is the atomic number of the tritium decay daughter nucleus, and $E_{\rm ee}$ and $p_{\rm ee}$ are the total energy and momentum of the emitted electron [158].

Almost all likelihood calculations discussed in this chapter used the entire energy range 0 to 60 keV$_{\rm nr}$ excluding the removed regions shown in Table 6.1. Some likelihood calculations assumed a fixed ratio between Compton and tritium backgrounds. That

fixed ratio was estimated using only data within the allowed region above 35 $\mathrm{keV_{nr}}$ (just above the Ge K-shell). Data within this region was assumed to be background only, because the upper mass limit of 25 GeV precludes any significant WIMP contribution above 35 $\mathrm{keV_{nr}}$.

The only two background sources in this region are due to tritium decay and Compton scattering; therefore, the observed spectrum in this region can be used to fix the ratio of Compton and tritium background amplitudes independent of any possible WIMP contribution. The ratio was estimated using a 2D maximum likelihood calculation with 0.1 eV energy bins using a Poissonian likelihood and flat prior probability functions for each background amplitude (a_C and a_T for Compton and tritium, respectively) such that the total background rate is between 0 and 4 times the total rate of events in the region of interest. The Poissonian likelihood, $\mathcal{L}_{\mathrm{ratio}}$, for energy bins E_k between 35 $\mathrm{keV_{nr}}$ and 60 $\mathrm{keV_{nr}}$ is given by

$$\mathcal{L}_{\mathrm{ratio}}(a_C, a_T) = \prod_k \frac{1}{N_k!} \left[a_C B_C(E_k) + a_T B_T(E_k)\right]^{N_k} e^{-a_C B_C(E_k) - a_T B_T(E_k)}, \tag{6.6}$$

where $\vec{N}$ is the set of the number of detected events in each bin (N_k). The total rate of each background, R_i with $i = C$, T, or $C + T$, can be calculated from the best fit amplitude and the shape of the spectrum by

$$R_i = \int_0^{E_{max}} a_i B_i(E) dE \tag{6.7}$$

where $E_{\mathrm{max}} = 60$ $\mathrm{keV_{nr}}$. From the best fits of a_C and a_T, the ratio of total Compton to tritium events was determined to be $R_{\mathrm{C}}/R_{\mathrm{T}} = 0.78 \pm^{0.47}_{0.36}$ with the errors calculated at the 2σ level.

This analysis followed the method described in Section 4.2 but included data with high expected backgrounds. If the energy dependence of the expected background is known, it can be included in the likelihood, leading to the combined likelihood of

$$\mathcal{L}_{\mathrm{DM+bkg}}(\vec{N}|\{m_\chi, c_i^0, c_i^1\}) = \prod_{k=1}^{n} \frac{1}{N_k!} (\eta_k + b_k)^{N_k} e^{-(\eta_k + b_k)}, \tag{6.8}$$

where η_k is the theoretical number of expected WIMP events expected assuming $\mathcal{O}_i$, N_k is the number of events detected, and b_k is the expected number of background events in the kth energy bin.

Instead of calculating the EFT likelihoods in terms of the coupling coefficients, the likelihoods were calculated in polar EFT coordinates of amplitude, A, and phase, θ. The coupling-coefficient amplitude is included with the prior probability function

$$\Pr(\log(A_i) = \begin{cases} \frac{1}{\log(A_{i,\max})-\log(A_{i,\min})}, & A_{i,\min} \leq A_i \leq A_{i,\max} \\ 0, \text{ otherwise} \end{cases}, \tag{6.9}$$

where $A_{i,\max}$ and $A_{i,\min}$ were chosen for each operator to span roughly 13 orders of magnitude around a low number of expected events that still allows for the detected spectrum to be a WIMP signal.

The coupling-coefficient phase is included with a flat prior given by

$$\Pr(\theta_i) = \begin{cases} \frac{1}{\pi}, & -\pi/2 \leq \theta_i \leq \pi/2 \\ 0, \text{ otherwise} \end{cases}. \tag{6.10}$$

The limits of $(-\pi/2 \leq \theta_i \leq \pi/2)$ were chosen because only the relative sign of the c_i^0 and c_i^1 matter. Both positive and both negative (or either one being positive and the other negative) have the same physical meaning. Therefore, all possible interactions are included within the chosen prior. The limits set in polar coordinates can be converted into the coupling-coefficient plane by recognizing that

$$\begin{aligned} c_i^0 &= A_i \sin(\theta_i) \\ c_i^1 &= A_i \cos(\theta_i). \end{aligned} \tag{6.11}$$

The WIMP mass, m_χ is included using a flat prior ranging from 0 to 25 GeV. Because CDMSlite Run 2 was designed to focus on the detection of low-mass WIMPS, the prior for WIMP mass was chosen with an upper limit of $m_{\max} = 25$ GeV for all operators. This mass limit was chosen because for all operators with a beta distribution spectral shape, above $m_{\max}$, a large portion of the theoretical event rate spectrum is past the 35 keV_{nr} upper threshold. Additionally, data from previous CDMS Ge experiments have set strong limits in this region on operators with an exponential spectral shape, such as operator 1 [49, 148].

For WIMP mass and coupling-coefficient amplitude, two possible options for the prior probability function are flat or log-flat. Changing the priors on WIMP mass and coupling-coefficient amplitude between these two options can change the 2σ contours in the amplitude-mass plane by a factor of 1 to ~ 2.5. In comparison to the 13 orders

of magnitude scanned for amplitude, this change is fairly minor. Therefore, the prior probability distributions stated above were chosen due to their ability to sufficiently sample the region of interest for each parameter. Further discussion on the effect of the choice of prior probability distribution can be found in Appendix B.

Where relevant, each background amplitude is included in the likelihood analysis using a flat prior on the background amplitude that spans from zero to the amplitude that corresponds to a background rate of two times the total number of detected events. In this way, every calculation that includes backgrounds allows for the possibility of the detected events containing no background or only background events. The exception to this rule appears only in analyses where we use the pre-determined ratio between Compton and tritium events (discussed above). Even though the same priors are used to compute this ratio, the shape of the background spectrum was determined under the assumption that all events with recoil energies larger than 35 keVnr are background.

6.2 Comparison to Published CDMSlite Run 2 Limit

As a test of the methodology and to show the power of including a background model, a 2D posterior distribution was determined for EFT operator 1 using the WIMP mass and the isoscalar coupling-coefficient amplitude ($\theta = 0$) parameters. This posterior distribution was calculated using the background models and removed energy regions described above. The resulting 2σ contour can be compared to the published CDMSlite Run 2 optimum interval (OI) limit on spin-independent WIMP-nucleon elastic scattering cross-section [48] and is shown in Figure 6.2a. This comparison is possible, because for operator 1, cross-section (σ_1^0) and coupling-coefficient amplitude (A_1) can be converted as described in Equation 5.8.

There are some key differences in the methods of how the CDMSlite Run 2 OI limit and the EFT 90% contour were calculated. The EFT contour is the result of a Bayesian analysis, while the OI limit provides the classical confidence interval [45]. The OI limit does not include any background models; this means that the entire signal is assumed to be a possible WIMP signal. For the EFT 90% contours, the Compton scattering and tritium contamination spectra (Equations 6.2 and 6.3) were included in the likelihood analysis, and the regions of high background around the activation peaks were removed

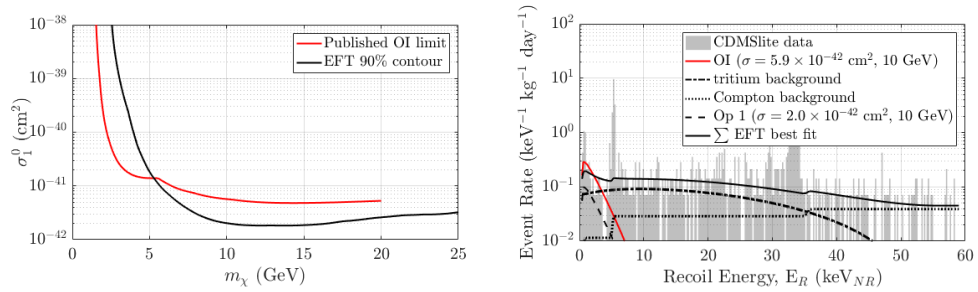

(a) Limit comparison (b) Spectrum comparison

Figure 6.2: Comparison of the published CDMSlite Run 2 Optimum Interval (OI) limit [48] and the EFT isoscalar operator 1 90% upper limit (left) and of the best fit cross-section recoil energy spectra at $m_\chi = 10$ GeV for both methods (right).

entirely. The maximum recoil energies considered vary between analyses as well. The analysis stopped at 20 keV$_{\text{nr}}$ for the OI method and 60 keV$_{\text{nr}}$ for the EFT analysis. The EFT likelihood analysis is also better able to take into account the different shapes of the data and input spectra.

The EFT likelihood analysis results in a 90% contour on cross-section that is ∼3 times lower at $m_\chi = 10$ GeV. A comparison of the spectra for these cross-sections at 10 GeV is shown in Figure 6.2b. For the EFT analysis, the included background models are shown as well. Both the OI spectra and the summed EFT spectra are compared to the CDMSlite Run 2 data. By eye, the EFT analysis seems to have resulted in a theoretical spectrum that more accurately reflects the shape of the experimental data spectrum due to the inclusion of the Compton scatter and tritium background models. The EFT analysis also results in a 90% contour that has a higher minimum WIMP mass limit ($\sim$ 1.3 GeV for the OI analysis and $\sim$ 2.6 GeV for the EFT analysis). The higher WIMP mass limit is due to the raised energy threshold from removing the energy regions around activation peaks.

6.3 Bayesian Evidence and Model Selection

As defined in Equation 4.20, the Bayesian evidence can be used to select which model is most likely to accurately describe the observed dark matter search data. The higher the

evidence, the better the fit of that model to the data. Each combination of EFT operator and background configuration can be considered a separate model. The background models considered are:

- ***two-parameter*** background model – Background model includes Compton and tritium backgrounds separately. This analysis has two background parameters (a_C and a_T) for a total of five parameters (m_χ, A_i, θ_i, a_C, and a_T).
- ***fixed ratio*** – Background model includes Compton and tritium backgrounds summed together with a predetermined ratio ($R_{\text{Compton}}/R_{\text{tritium}} = 0.78 \pm^{47}_{36}$). This analysis has one background parameter ($a_{\text{C+T}}$) for a total of four background parameters (m_χ, A_i, θ_i, and $a_{\text{C+T}}$).
- ***Compton*** only – Background model includes Compton backgrounds only. This analysis has only one background parameter (a_C) for a total of four parameters (m_χ, A_i, θ_i, and a_C).
- ***tritium*** only – Background model includes tritium backgrounds only. This analysis has only one background parameter (a_T) for a total of four parameters (m_χ, A_i, θ_i, and a_T).
- ***no background*** – No background models included in this analysis for a total of three parameters (m_χ, A_i, and θ_i).

The Bayesian evidence of each model is shown in Table 6.2. The prior probability functions used to calculate these evidences were a flat mass prior and flat $\log(A_i)$ prior (Equation 6.9). The model with the highest evidence is a background-only model; therefore, the CDMSlite Run 2 data is entirely consistent with the expected backgrounds. Because the background-only analysis for the ***fixed ratio*** option had the highest evidence, it was chosen as the reference model for calculating the evidence ratios. Table 6.3 gives the ratio between the evidence of a given model to the evidence of the reference model.

The ***fixed ratio*** evidences are all larger than the evidences for any other background model. This implies that as long as the ratio is predetermined correctly, it is unnecessary to include each background amplitude separately in the likelihood calculation. This

Bkg Model:	***Two-parameter***	***Fixed ratio***	***Compton*** only	***Tritium*** only	***No background***
Dimensions:	5 (Bkg = 2)	4 (Bkg = 1)	4 (Bkg= 1)	4 (Bkg = 1)	3 (Bkg = 0)
EFT Models	$\log(\mathcal{Z})$				
Bkg only	-303.40 ± 0.03	$\mathbf{-301.10 \pm 0.03}$	-331.91 ± 0.02	-532.94 ± 0.02	–
$\mathcal{O}_1$	-303.77 ± 0.03	-301.59 ± 0.03	-315.29 ± 0.04	-343.36 ± 0.06	-338.37 ± 0.05
$\mathcal{O}_3$	-304.32 ± 0.03	-302.26 ± 0.03	-311.24 ± 0.04	-307.00 ± 0.04	-327.96 ± 0.04
$\mathcal{O}_4$	-304.00 ± 0.03	-301.85 ± 0.03	-316.66 ± 0.04	-319.86 ± 0.06	-313.29 ± 0.05
$\mathcal{O}_5$	-304.19 ± 0.03	-302.12 ± 0.03	-307.68 ± 0.04	-307.98 ± 0.04	-308.12 ± 0.04
$\mathcal{O}_6$	-304.39 ± 0.04	-302.27 ± 0.03	-311.30 ± 0.04	-307.16 ± 0.04	-324.01 ± 0.05
$\mathcal{O}_7$	-303.93 ± 0.03	-301.87 ± 0.03	-318.60 ± 0.04	-351.98 ± 0.07	-313.20 ± 0.05
$\mathcal{O}_8$	-304.04 ± 0.03	-302.01 ± 0.03	-309.13 ± 0.05	-311.52 ± 0.05	-308.39 ± 0.04
$\mathcal{O}_9$	-304.01 ± 0.03	-301.92 ± 0.03	-307.51 ± 0.04	-314.92 ± 0.06	-312.79 ± 0.05
$\mathcal{O}_{10}$	-304.46 ± 0.04	-301.52 ± 0.03	-307.51 ± 0.04	-309.24 ± 0.04	-307.46 ± 0.04
$\mathcal{O}_{11}$	-304.16 ± 0.03	-302.08 ± 0.03	-307.44 ± 0.04	-310.96 ± 0.04	-307.34 ± 0.04

Table 6.2: Bayesian evidence, $\mathcal{Z}$, for each combination of background and EFT models. The reference chosen is the fixed ratio background only run, which has been highlighted in yellow and bolded.

Bkg Model:	***Two-parameter***	***Fixed ratio***	***Compton*** only	***Tritium*** only	***No background***
Dimensions:	5 (Bkg = 2)	4 (Bkg = 1)	4 (Bkg= 1)	4 (Bkg = 1)	3 (Bkg = 0)
EFT Models	$\mathcal{Z}_{\text{model}}/\mathcal{Z}_{\text{ref}}$				
Bkg only	0.100 ± 0.004	**1.00**	$(4.2 \pm 0.2) \times 10^{-14}$	$(2.06 \pm 0.07) \times 10^{-101}$	–
$\mathcal{O}_1$	0.069 ± 0.003	0.61 ± 0.03	$(6.9 \pm 0.3) \times 10^{-7}$	$(4.4 \pm 0.3) \times 10^{-19}$	$(6.5 \pm 0.4) \times 10^{-17}$
$\mathcal{O}_3$	0.040 ± 0.002	0.31 ± 0.01	$(3.9 \pm 0.2) \times 10^{-5}$	0.0027 ± 0.0001	$(2.2 \pm 0.1) \times 10^{-12}$
$\mathcal{O}_4$	0.055 ± 0.002	0.47 ± 0.02	$(1.75 \pm 0.09) \times 10^{-7}$	$(7.1 \pm 0.5) \times 10^{-9}$	$(5.1 \pm 0.3) \times 10^{-6}$
$\mathcal{O}_5$	0.046 ± 0.002	0.36 ± 0.02	$(1.39 \pm 0.07) \times 10^{-3}$	$(1.03 \pm 0.05) \times 10^{-3}$	$(8.9 \pm 0.4) \times 10^{-4}$
$\mathcal{O}_6$	0.037 ± 0.002	0.31 ± 0.01	$(3.7 \pm 0.2) \times 10^{-5}$	0.0023 ± 0.0001	$(1.12 \pm 0.07) \times 10^{-10}$
$\mathcal{O}_7$	0.059 ± 0.003	0.46 ± 0.02	$(2.5 \pm 0.1) \times 10^{-8}$	$(8.0 \pm 0.6) \times 10^{-23}$	$(5.6 \pm 0.3) \times 10^{-6}$
$\mathcal{O}_8$	0.053 ± 0.002	0.40 ± 0.02	$(3.3 \pm 0.2) \times 10^{-4}$	$(3.0 \pm 0.2) \times 10^{-5}$	$(6.8 \pm 0.3) \times 10^{-4}$
$\mathcal{O}_9$	0.054 ± 0.002	0.44 ± 0.02	$(1.65 \pm 0.08) \times 10^{-3}$	$(9.96 \pm 0.07) \times 10^{-7}$	$(8.4 \pm 0.05) \times 10^{-6}$
$\mathcal{O}_{10}$	0.035 ± 0.002	0.66 ± 0.03	$(1.65 \pm 0.08) \times 10^{-3}$	$(2.9 \pm 0.1) \times 10^{-4}$	$(1.73 \pm 0.09) \times 10^{-3}$
$\mathcal{O}_{11}$	0.047 ± 0.002	0.38 ± 0.02	$(1.76 \pm 0.09) \times 10^{-3}$	$(5.2 \pm 0.3) \times 10^{-5}$	0.0019 ± 0.0001

Table 6.3: The ratio of Bayesian evidence of each model compared to the reference, $\mathcal{Z}_{\text{model}}/\mathcal{Z}_{\text{ref}}$. The reference chosen is the fixed ratio background only run, which has been highlighted in yellow and bolded.

reduces the complexity and running time of the likelihood calculation. Comparing the ***fixed ratio*** or ***two-parameter*** runs to the ***tritium***, ***Compton***, and ***no background*** runs shows that Bayesian evidence is consistently higher when both background sources are included in the analysis. This demonstrates that each of the background sources included are necessary to describe the CDMSlite data and that no single EFT operator entirely mimics either background shape. For a background-limited experiment like CDMSlite, the fact that the background shapes differ from the theoretically expected WIMP spectrum means that even though the evidences show the data is consistent with background, upper limits on WIMP mass and coupling-coefficient amplitudes can still be set from the likelihood calculations.

6.4 Calculated Posterior Distributions

The Bayesian evidences in Table 6.2 provide a complete summary of the results of this analysis. However, further details can be seen in the posterior distribution. Section 6.4.1 describes the posterior distributions for the background-only models and Section 6.4.2 has the posterior distributions for the single EFT operators models. The two-operator interference models exist as well, but they have not been included in this analysis. Because the evidences for the ***fixed ratio*** option were consistently much higher than any other background configuration, only these posterior distributions are shown.

6.4.1 Background-only Model

The total number of background events in the CDMSlite Run 2 data set were estimated using the background models for either the ***fixed ratio*** or the ***two-parameter*** cases. Figure 6.3 shows the posterior distributions for the background-only models. The ***fixed ratio*** model only has one background parameter ($R_{\mathrm{C+T}}$), and the ***two-parameter*** model has two (R_{C} and R_{T}). The best fit point of each of the 1D posterior distributions can be used to calculate the rate of background. The total rate is the sum across all energy bins for the chosen background while including the regions that had been previously removed from the analysis. Unless otherwise noted, the errors quoted were calculated at the 2σ level.

The ***fixed ratio*** background-only posterior distribution is nearly symmetric about

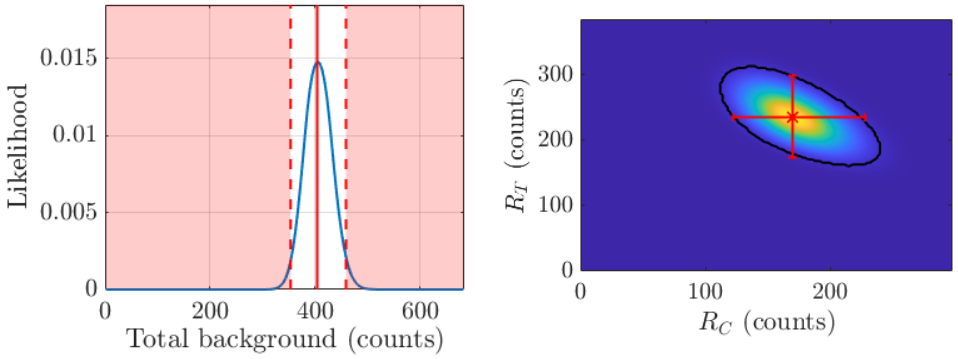

(a) ***Fixed ratio*** (b) ***Two-parameter***

Figure 6.3: Background-only posterior distributions. For the 1D ***fixed ratio*** posterior distribution (left), the total number of background events includes both the Compton and tritium with the predetermined ratio of $R_{\mathrm{C}}/R_{\mathrm{T}} = 0.78\pm^{0.47}_{0.36}$. The solid red line designates the point of maximum likelihood, the dashed red lines the edge of the 2σ confidence region, and the red shaded are the regions excluded by the 2σ confidence region. For the 2D ***two-parameter*** posterior distribution (right), the 2σ contour is shown with the black line and the best best fit background configuration is shown in red with 2σ errors.

the point of maximum likelihood. The error on the best fit point is calculated at 2σ from this point. According to the best fit point, the total rate of all background sources is $404\pm^{55}_{51}$ events. With the pre-determined ratio of $R_{\mathrm{C}}/R_{\mathrm{T}} = 0.78\pm^{0.47}_{0.36}$, this leads to a total Compton background of $177\pm^{65}_{51}$ events and a tritium background of $227\pm^{67}_{54}$ events. The errors on these background estimates include the error on the ratio estimate. If instead the 2D posterior distribution from the background-only ***two-parameter*** fit is used, the total number of backgrounds for each source is $170\pm^{58}_{48}$ events for Compton and 236 ± 62 events for tritium with a total background of $406\pm^{85}_{78}$. This leads to a slightly higher result for tritium and a lower result for Compton, although the results are very similar. As a measure of the systematic errors of the background estimates, a drop in energy of the "step" below the K-shell of the Compton spectrum on the order of 3% changes the count of the individual backgrounds on the order of 6% and the total background on the order of 0.3%.

Recently, an attempt to calculate the background rates for all background types in CDMSlite Run 2 was completed using a different maximum likelihood technique [152]. This analysis resulted in a calculated total Compton background of $138 \pm^{22}_{18}$ events and total tritium background of 256 ± 23 events with the errors listed at the 1σ level. While these results have a slightly different best-fit ratio between Compton to tritium than the results presented here, the numbers of events of each species in the two analyses are within error of each other.

6.4.2 Single Operator EFT Models

The single operator models for the ***fixed ratio*** analysis result in 4D likelihoods. The 4D operator posterior distributions must be marginalized into three 2D posterior distributions on WIMP parameters and one 1D background posterior distribution. These 2D WIMP-parameter marginalized posterior distributions are shown in Figures 6.4, 6.5, and 6.6 for the prior choices of a flat mass prior and a flat $\log(A_i)$ prior (Equation 6.9). Each marginalized posterior distribution is shown with 2σ contours. For clarity, each marginalized posterior distribution has been renormalized such that the maximum value of the likelihood is 1 (yellow) and the minimum value zero (dark blue). In the mass-amplitude plane (far left plot for each operator), all operators show 2σ contours whose shapes resemble that of the optimum interval upper limits given in a standard CDMS analysis (compare to Figure 6.2a) [46, 48, 56, 70, 77, 148]. This is not unexpected, given that the Bayesian evidences show that the CDMSlite Run 2 data is consistent with the expected backgrounds. Most of these operators have flat posterior distributions below the 2σ contour, and the mass-phase plane is nearly flat for every operator.

The amplitude-phase plane (shown in polar coordinates), shows a tendency to favor lower amplitudes with spikes into higher amplitudes at particular angles. A spike in the 2σ contour represent directions in which the limit on amplitude is weaker due to destructive inference in the phase of that operator for Ge. The maximum interference phase is the phase at which the isoscalar and isovector components of the coupling coefficients have the largest destructive interference. Destructive interference causes the amplitudes of the theoretical WIMP signal to decrease, meaning it takes a larger amplitude to get to the same number of events as for other phases. Because the maximum interference phase can be different for different target materials, combining the CDMSlite Run 2 data

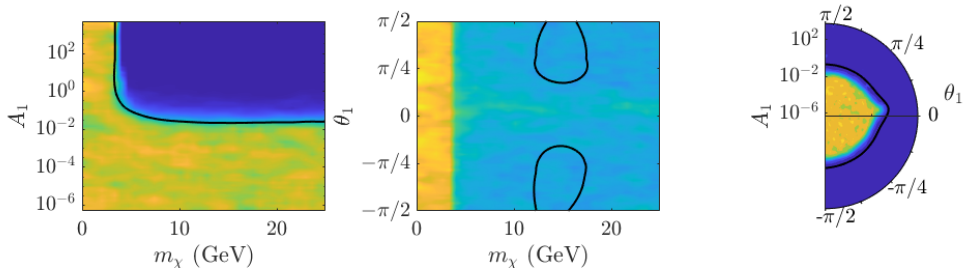

(a) Operator 1

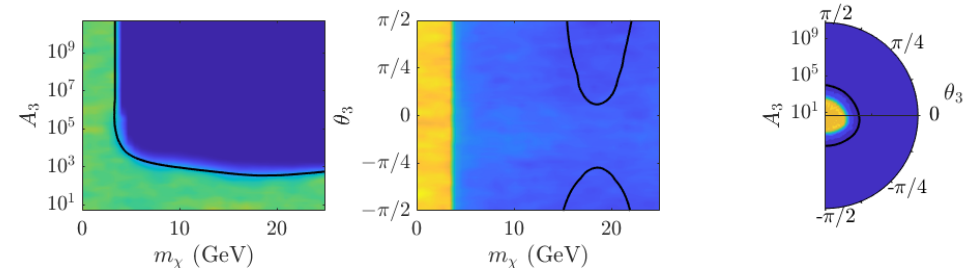

(b) Operator 3

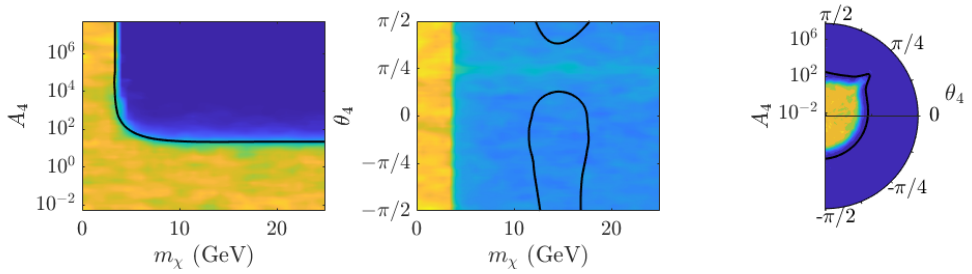

(c) Operator 4

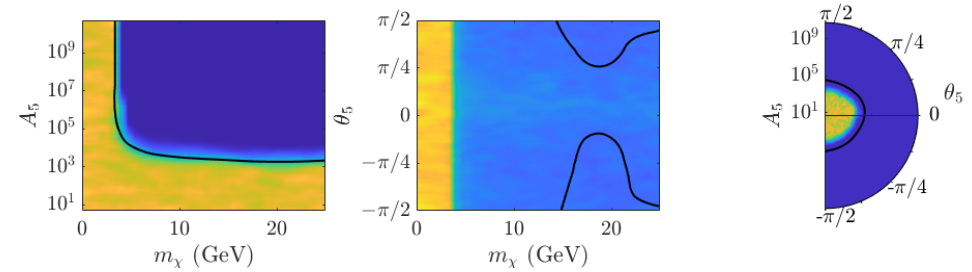

(d) Operator 5

Figure 6.4: Fixed ratio 2D marginalized posterior distributions for the polar parameters (m_χ, A_i, and θ_i) of each single EFT operator likelihood for operators 1 - 5. 2σ contours are shown in black.

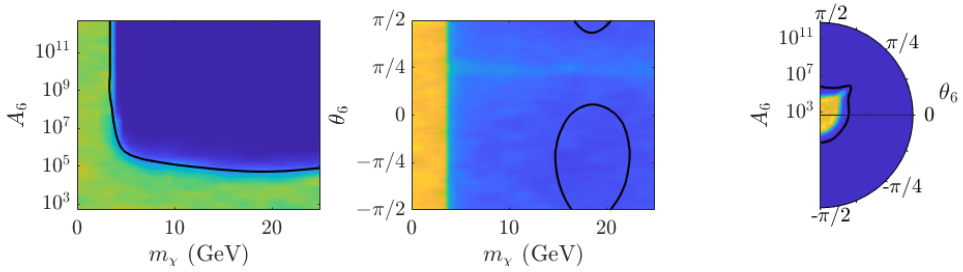

(a) Operator 6

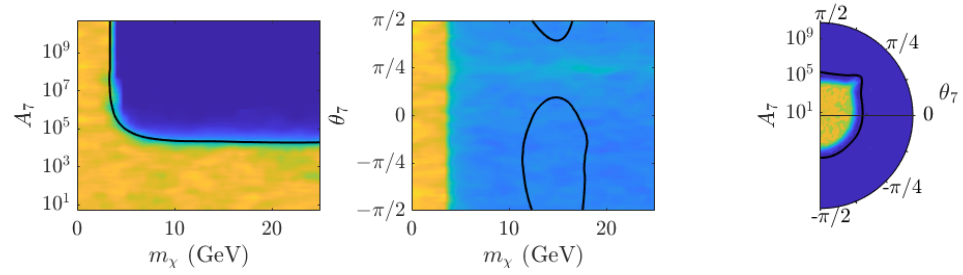

(b) Operator 7

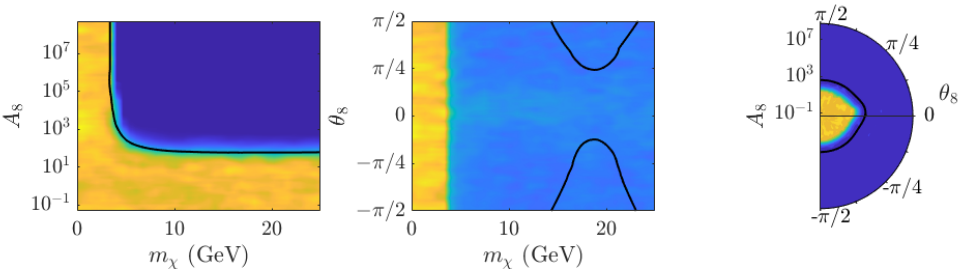

(c) Operator 8

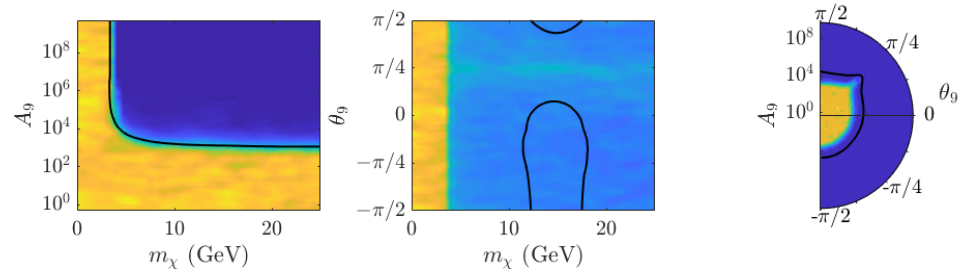

(d) Operator 9

Figure 6.5: Fixed ratio 2D marginalized posterior distributions for the polar parameters (m_χ, A_i, and θ_i) of each single EFT operator likelihood for operators 6 - 9. 2σ contours are shown in black.

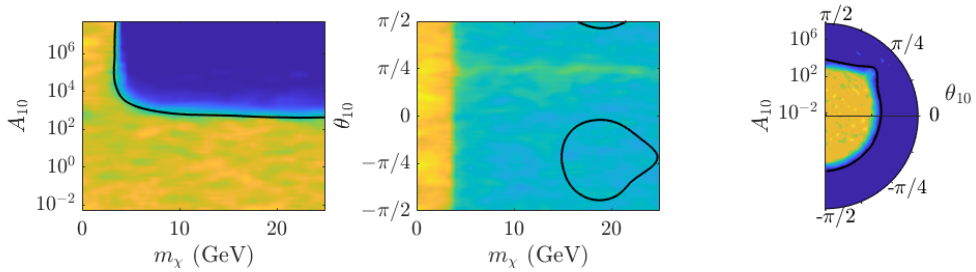

(a) Operator 10

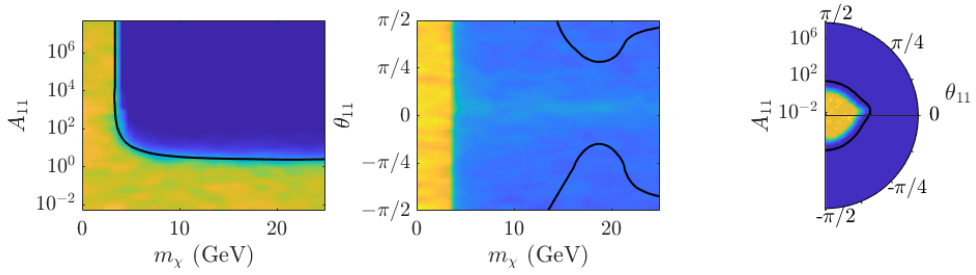

(b) Operator 11

Figure 6.6: Fixed ratio 2D marginalized posterior distributions for the polar parameters (m_χ, A_i, and θ_i) of each single EFT operator (10 and 11). 2σ contours are shown in black.

with data from another experiment (such as the future SuperCDMS HV Si data [46]) can set stronger limits even if there is no WIMP detection [124, 130–132]. SD operators 4, 6, 7, 9, and 10 and SI operator 5 show destructive interference at $\theta = \pi/4$, which represents proton-coupling. Operators 1, 8, and 11 show a slight weakness towards isoscalar-couplings ($\theta = 0$), while operator 3 is slightly weak towards neutron-coupling ($\theta = -\pi/4$).

The background likelihood for each operator is one-dimensional. The 1D posterior distributions are shown in Figure 6.7, similarly to the background-only posterior distributions in Figure 6.3. For the most part, all of these posterior distributions look near-Gaussian, and the location of the peak does not vary between operators. All of the peaks are at 404 events, which is consistent with the 404^{+55}_{-51} events of the ***fixed ratio*** background-only likelihood and is consistently 2 events less than the total counts for the ***two-parameter*** background-only likelihood (406^{+85}_{-78}). Therefore, the theoretical

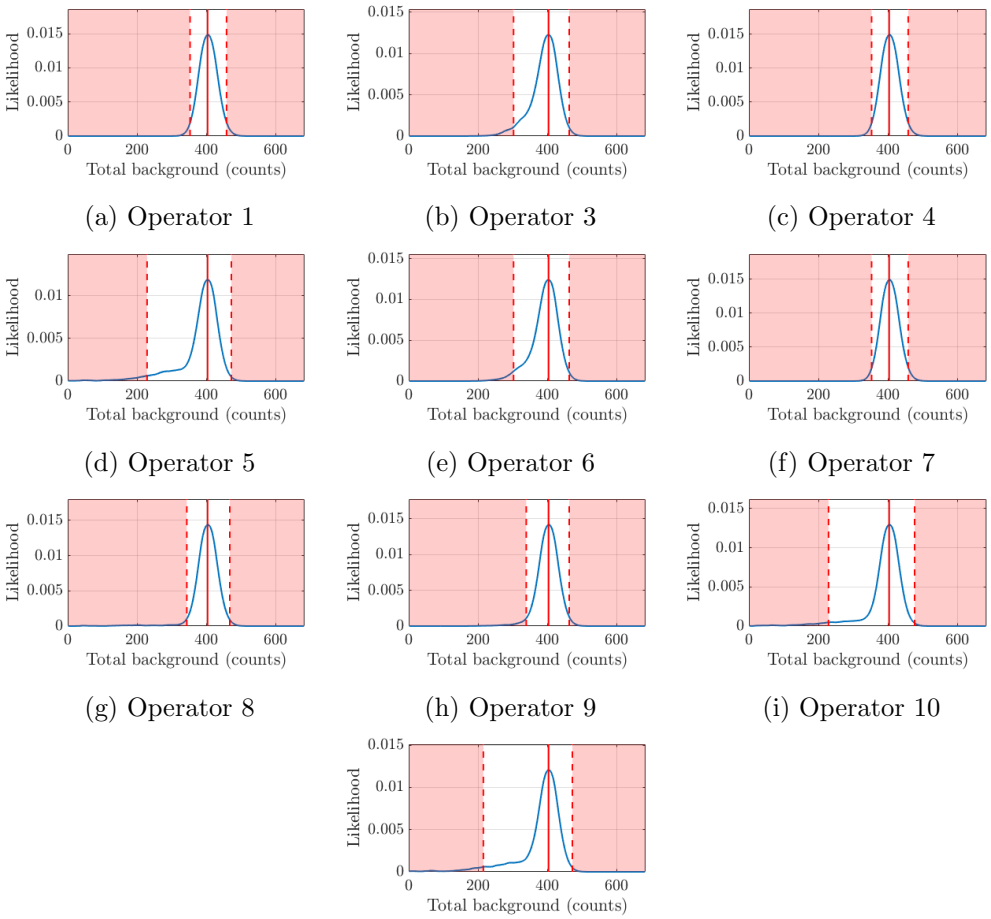

(a) Operator 1 (b) Operator 3 (c) Operator 4

(d) Operator 5 (e) Operator 6 (f) Operator 7

(g) Operator 8 (h) Operator 9 (i) Operator 10

(j) Operator 11

Figure 6.7: Fixed ratio 1D marginalized posterior distributions for the total background of each single EFT operator. The solid red line designates the point of maximum likelihood, the dashed red lines the edge of the 2σ confidence region, and the red shaded are the regions excluded by the 2σ confidence region.

EFT spectra are fitting ~ 2 events of the detected data spectrum.

Chapter 7

Conclusion

Plans for upgrading SuperCDMS SNOLAB include the possibility of putting in a neutron veto. Plastic is an attractive choice because of the danger of leaks from a liquid option. The feasibility of using gadolinium doped organic plastic scintillators read out using SiPMs coupled to WLS fibers has been tested in order to inform design decisions. Samples of Gd-doped plastic scintillators were successfully fabricated with up to 0.055% wt. Gd. This is a significantly lower concentration than what simulations show should be necessary for SuperCDMS SNOLAB (loading of 1% wt. Gd); however, higher concentrations are possible with the use of co-monomers [111]. Collaboration with the Bertrand *et al.* [111] group has begun with the plan of testing their more highly-loaded samples.

The proposed readout strategies for the active neutron veto were tested and characterized. These included quantum efficiency and photon detection efficiency measurements of the PMT and SiPMs respectively. Included within these measurements was a calculation of the gain of each photo detector. The gains were all calculated to be on the order of 10^6, and the quantum efficiencies were reasonably similar to the manufacturer's specifications. Additionally, the dark count of one SiPM were measured to be 1.33 ± 0.52 MHz, which matches the the acceptable dark count rate at room temperature given by Hamamatsu [116]. The optical tests of plastic scintillator samples that were polymerized at UMN included the emission spectra and effective attenuation length measurements. These tests showed only minor changes due to gadolinium loading. The WLS fiber was also characterized by the emission spectrum and fiber trapping efficiency

and determined to be a reasonable choice for the design.

With the systematic analysis procedure suggested in Section 4.2, higher-dimensional analysis of dark matter data using the model-independent EFT framework is possible. MultiNest [143–145] is an effective Bayesian inference tool that can be used to efficiently scan high-dimensional likelihoods. The number of operators or dimensions in a likelihood can be limited by using the Bayesian evidence for single-operator 3D likelihoods to determine which operators best fit the observed events. Higher-dimensional likelihoods can be marginalized down to 2D and 1D likelihoods in order to ease visualization and set constraints on the WIMP mass and coupling coefficients.

Assumptions about the operators could lead to tension between experiments. For example, the tension between the isoscalar operator 1 (spin-independent) analyses published by CDMS II Si [56], CDMS II Ge [148], and LUX [149] could be relieved by including other coupling coefficients in the analysis, such as the isovector operator 1 component, while setting new limits on dark matter interactions. Combining the three experiments into a single joint likelihood leads to stronger limits than what is possible from a single target or experiment alone.

Using simulated data (assuming $\mathcal{O}_3$ or $\mathcal{O}_8$ interaction) to test the proposed analysis procedure showed that the simulated data point can be reconstructed assuming one EFT operator or assuming two operators during the likelihood analyses. Comparisons of the Bayesian evidence for 3D (WIMP mass and a single EFT operator) likelihoods can identify which operator(s) fit the data well. However, it is critical to include more than one target in the analysis, in order to differentiate between operators of similar recoil energy spectra and to create better defined confidence contours, especially when dealing with a low number of detected events per experiment.

When operators, such as $\mathcal{O}_1$ and $\mathcal{O}_3$, have different recoil energy spectral shapes due to different momentum dependencies, they can be more easily distinguished from each other by the proposed analysis procedure. When using spectral shape in this way, it is extremely important to have a low enough experimental energy threshold in order to be able to measure the spectral differences. For a recoil energy spectrum similar to that of $\mathcal{O}_3$, if the experimental energy threshold is above or near the peak of the spectrum (as it was for LXe in our $\mathcal{O}_3$ simulation) then the spectral shape can appear to follow the standard exponential decay of $\mathcal{O}_1$. Very low-threshold dark matter experiments, such

as the previously published CDMSlite [48, 70] and the proposed SuperCDMS SNOLAB High-Voltage experiments [46] will be particularly useful to convincingly perform spectral shape discrimination in the EFT framework.

The analysis in Section 6 represents the first dark matter EFT analyses of CDMSlite data and of high background data in general. The techniques used to handle the background include removing energy bins around known activation peaks of several background sources and modeling the shapes of the remaining backgrounds. The relative amounts of each background source included in the analysis (Compton and tritium) were predetermined using a maximum likelihood estimation method on CDMSlite data above ~ 35 keV$_{\mathrm{nr}}$. Posterior distributions were calculated for combinations of five different background models (both backgrounds included separately, both backgrounds included with set relative amounts, each background included on its own, and no backgrounds) and each EFT operator.

The Bayesian evidences of these likelihoods show that the CDMSlite Run 2 data is well described by the Compton and tritium backgrounds, and that the fit is not greatly improved by including any of the EFT operators. Using the ***two-parameter*** background-only posterior distribution, the amount of Compton backgrounds was calculated to be $170\pm^{58}_{48}$ events, and the amount of tritium to be 236 ± 62 events. However, some of the EFT operators do fit the data better than others, with operators 1, 4, 7, and 10 having a ratio of evidence to the ***fixed ratio*** background-only likelihood of greater than 0.45. Even having data consistent with background, it is possible to calculate clean 2σ upper limits in the mass-amplitude plane of each EFT operator. These are similar to (but not directly comparable to) the cross-section vs. mass upper limits published by dark matter experiments.

The characterization measurements for an active neutron veto and the development of an effective field theory based dark matter analysis benefit SuperCDMS moving forward. After more germanium or silicon towers are added to the payload at SNOLAB, the neutron background will become more dominant. An active neutron veto will become necessary, and the characterization measurements listed here can be used to make prototyping and design decisions. As shown in Figure 1.5 of Section 1.3, for a large portion of the WIMP parameter space, SuperCDMS will not have the lowest sensitivity. However, the complementarity between targets suggested by the EFT analysis means

that without multiple targets, direct detection data can be easily misinterpreted and that experiments with the lowest sensitivities cannot set strong limits on WIMP mass and cross-sections on their own. The EFT analysis technique is also useful for high-background data in order to provide background-subtracted limits to WIMP interaction parameters.

Bibliography

[1] J. C. Kapteyn. First Attempt at a Theory of the Arrangement and Motion of the Sidereal System. *Astrophys. J.*, 55:302–328, 1922.

[2] F. Zwicky. Die Rotverschiebung von extragalaktischen Nebeln. *Helv. Phys. Acta*, 6:110–127, 1933. [Gen. Relativ. Gravit.41,207(2009)].

[3] J. H. Oort. Some Problems Concerning the Structure and Dynamics of the Galactic System and the Elliptical Nebulae NGC 3115 and 4494. *Astrophys J.*, 91:273, April 1940.

[4] P. A. R. Ade et al. Planck 2015 results. XIII. Cosmological parameters. *Astron. Astrophys.*, 594:A13, 2016, 1502.01589.

[5] Douglas Clowe, Anthony Gonzalez, and Maxim Markevitch. Weak lensing mass reconstruction of the interacting cluster 1E0657-558: Direct evidence for the existence of dark matter. *Astrophys. J.*, 604:596–603, 2004, astro-ph/0312273.

[6] É. Aubourg et al. Cosmological implications of baryon acoustic oscillation measurements. *Phys. Rev.*, D92(12):123516, 2015, 1411.1074.

[7] K. Jedamzik and Maxim Pospelov. Big Bang Nucleosynthesis and Particle Dark Matter. *New J. Phys.*, 11:105028, 2009, 0906.2087.

[8] Gerard Jungman, Marc Kamionkowski, and Kim Griest. Supersymmetric dark matter. *Phys. Rept.*, 267:195–373, 1996, hep-ph/9506380.

[9] Marco Cirelli, Nicolao Fornengo, and Alessandro Strumia. Minimal dark matter. *Nucl. Phys.*, B753:178–194, 2006, hep-ph/0512090.

[10] Ernesto Lopez Fune, Paolo Salucci, and Edvige Corbelli. Radial dependence of the dark matter distribution in M33. *Mon. Not. Roy. Astron. Soc.*, 468(1):147–153, 2017, 1611.01409.

[11] S. Fay. Scalar fields properties for flat galactic rotation curves. *Astron. Astrophys.*, 413:799, 2004, gr-qc/0402103.

[12] Richard Massey, Thomas Kitching, and Johan Richard. The dark matter of gravitational lensing. *Rept. Prog. Phys.*, 73:086901, 2010, 1001.1739.

[13] M. James Jee, William A. Dawson, Andra Stroe, David Wittman, Reinout J. Van Weeren, Marcus Bruggen, Marusa Bradac, and Huub Rottgering. MC^2: Mapping the Dark Matter Distribution of the "Toothbrush" Cluster RX J0603.3+4214 with Hubble Space Telescope and Subaru Weak lensing. *Astrophys. J.*, 817(2):179, 2016, 1510.03486.

[14] Raphael Gavazzi, Tommaso Treu, Jason D. Rhodes, Leon Ve Koopmans, Adam S. Bolton, Scott Burles, Richard Massey, and Leonidas A. Moustakas. The Sloan Lens ACS Survey. 4. The mass density profile of early-type galaxies out to 100 effective radii. *Astrophys. J.*, 667:176–190, 2007, astro-ph/0701589.

[15] T. P. Walker, G. Steigman, H.-S. Kang, D. M. Schramm, and K. A. Olive. Primordial nucleosynthesis redux. *Astrophys. J.*, 376:51–69, 1991.

[16] Vuk Mandic. *First Results from the Cryogenic Dark Matter Search Experiment at the Deep Site*. PhD thesis, Univeristy of California, Berkeley, 2004.

[17] Wayne Hu. Mapping the dark matter through the cmb damping tail. *Astrophys. J.*, 557:L79–L83, 2001, astro-ph/0105424.

[18] D. N. Spergel et al. Wilkinson Microwave Anisotropy Probe (WMAP) three year results: implications for cosmology. *Astrophys. J. Suppl.*, 170:377, 2007, astro-ph/0603449.

[19] Bernard J. Carr. Baryonic dark matter in galaxies. *ASP Conf. Ser.*, 239:37, 2001, astro-ph/0008028.

[20] Dennis J. Hegyi and Keith A. Olive. Evidence against baryonic dark matter in elliptical galaxies. *Astrophys. J.*, 346:648–652, November 1989.

[21] Evalyn I. Gates, Geza Gyuk, and Michael S. Turner. Microlensing and halo cold dark matter. *Phys. Rev. Lett.*, 74:3724–3727, 1995, astro-ph/9411073.

[22] Michael S. Turner. Windows on the Axion. *Phys. Rept.*, 197:67–97, 1990.

[23] Georg G. Raffelt, Javier Redondo, and Nicolas Viaux Maira. The meV mass frontier of axion physics. *Phys. Rev.*, D84:103008, 2011, 1110.6397.

[24] Simon D. M. White, C. S. Frenk, and M. Davis. Clustering in a Neutrino Dominated Universe. *Astrophys. J.*, 274:L1–L5, 1983.

[25] V. Barger, Wai Yee Keung, D. Marfatia, and G. Shaughnessy. PAMELA and dark matter. *Phys. Lett.*, B672:141–146, 2009, 0809.0162.

[26] Thomas Appelquist, Hsin-Chia Cheng, and Bogdan A. Dobrescu. Bounds on universal extra dimensions. *Phys. Rev.*, D64:035002, 2001, hep-ph/0012100.

[27] Hsin-Chia Cheng and Ian Low. TeV symmetry and the little hierarchy problem. *JHEP*, 09:051, 2003, hep-ph/0308199.

[28] Vernon Barger, Paul Langacker, Mathew McCaskey, Michael J. Ramsey-Musolf, and Gabe Shaughnessy. LHC Phenomenology of an Extended Standard Model with a Real Scalar Singlet. *Phys. Rev.*, D77:035005, 2008, 0706.4311.

[29] M. G. Aartsen et al. IceCube Search for Dark Matter Annihilation in nearby Galaxies and Galaxy Clusters. *Phys. Rev.*, D88:122001, 2013, 1307.3473.

[30] K. Choi, Carsten Rott, and Yoshitaka Itow. Impact of the dark matter velocity distribution on capture rates in the Sun. *J. Cosmol. Astropart. Phys.*, 1405:049, 2014, 1312.0273.

[31] T. Tanaka et al. An Indirect Search for WIMPs in the Sun using 3109.6 days of upward-going muons in Super-Kamiokande. *Astrophys. J.*, 742:78, 2011, 1108.3384.

[32] S. Adrian-Martinez et al. First results on dark matter annihilation in the Sun using the ANTARES neutrino telescope. *JCAP*, 1311:032, 2013, 1302.6516.

[33] Alex Geringer-Sameth. The VERITAS Dark Matter Program. In *Proceedings, 4th International Fermi Symposium: Monterey, California, USA, October 28-November 2, 2012*, 2013, 1303.1406.

[34] A. Abramowski et al. Search for Photon-Linelike Signatures from Dark Matter Annihilations with H.E.S.S. *Phys. Rev. Lett.*, 110:041301, 2013, 1301.1173.

[35] F. Aharonian et al. Observations of the Crab Nebula with H.E.S.S. *Astron. Astrophys.*, 457:899–915, 2006, astro-ph/0607333.

[36] Elmo Tempel, Andi Hektor, and Martti Raidal. Fermi 130 GeV gamma-ray excess and dark matter annihilation in sub-haloes and in the Galactic centre. *JCAP*, 1209:032, 2012, 1205.1045. [Addendum: JCAP1211,A01(2012)].

[37] A. A. Abdo et al. Observations of Milky Way Dwarf Spheroidal galaxies with the Fermi-LAT detector and constraints on Dark Matter models. *Astrophys. J.*, 712:147–158, 2010, 1001.4531.

[38] Rolf Kappl and Martin Wolfgang Winkler. Dark Matter after BESS-Polar II. *Phys. Rev.*, D85:123522, 2012, 1110.4376.

[39] K. Abe et al. Measurement of the cosmic-ray antiproton spectrum at solar minimum with a long-duration balloon flight over Antarctica. *Phys. Rev. Lett.*, 108:051102, 2012, 1107.6000.

[40] J. D. Lewin and P. F. Smith. Review of mathematics, numerical factors, and corrections for dark matter experiments based on elastic nuclear recoil. *Astropart. Phys.*, 6:87–112, 1996.

[41] D. G. Cerdeño and A. M. Green. Direct detection of wimps. In G. Bertone, editor, *Particle Dark Matter: Observations, Models, and Searches*. Cambridge University Press, Cambridge, England, 2010, 1002.1912.

[42] A. K. Drukier, Katherine Freese, and D. N. Spergel. Detecting Cold Dark Matter Candidates. *Phys. Rev.*, D33:3495–3508, 1986.

[43] Christopher McCabe. The Astrophysical Uncertainties Of Dark Matter Direct Detection Experiments. *Phys. Rev.*, D82:023530, 2010, 1005.0579.

[44] Marco Cirelli, Eugenio Del Nobile, and Paolo Panci. Tools for model-independent bounds in direct dark matter searches. *J. Cosmol. Astropart. Phys.*, 1310:019, 2013, 1307.5955.

[45] S. Yellin. Finding an upper limit in the presence of unknown background. *Phys. Rev.*, D66:032005, 2002, physics/0203002.

[46] R. Agnese et al. Projected Sensitivity of the SuperCDMS SNOLAB experiment. *Phys. Rev.*, D95(8):082002, 2017, 1610.00006.

[47] D. S. Akerib et al. LUX-ZEPLIN (LZ) Conceptual Design Report. 2015, 1509.02910.

[48] R. Agnese et al. New Results from the Search for Low-Mass Weakly Interacting Massive Particles with the CDMS Low Ionization Threshold Experiment. *Phys. Rev. Lett.*, 116(7):071301, 2016, 1509.02448.

[49] R. Agnese et al. Search for Low-Mass Weakly Interacting Massive Particles with SuperCDMS. *Phys. Rev. Lett.*, 112(24):241302, 2014, 1402.7137.

[50] E. Aprile et al. First Dark Matter Search Results from the XENON1T Experiment. *Phys. Rev. Lett.*, 119(18):181301, 2017, 1705.06655.

[51] E. Aprile et al. XENON100 Dark Matter Results from a Combination of 477 Live Days. *Phys. Rev.*, D94(12):122001, 2016, 1609.06154.

[52] G. Angloher et al. Results on light dark matter particles with a low-threshold CRESST-II detector. *Eur. Phys. J.*, C76(1):25, 2016, 1509.01515.

[53] P. Agnes et al. Results from the first use of low radioactivity argon in a dark matter search. *Phys. Rev.*, D93(8):081101, 2016, 1510.00702. [Addendum: Phys. Rev.D95,no.6,069901(2017)].

[54] P. Agnes et al. Low-mass Dark Matter Search with the DarkSide-50 Experiment. 2018, 1802.06994.

[55] F. Ruppin, J. Billard, E. Figueroa-Feliciano, and L. Strigari. Complementarity of dark matter detectors in light of the neutrino background. *Phys. Rev.*, D90(8):083510, 2014, 1408.3581.

[56] R. Agnese et al. Silicon Detector Dark Matter Results from the Final Exposure of CDMS II. *Phys. Rev. Lett.*, 111(25):251301, 2013, 1304.4279.

[57] C. Savage, G. Gelmini, P. Gondolo, and K. Freese. Compatibility of DAMA/LIBRA dark matter detection with other searches. *JCAP*, 0904:010, 2009, 0808.3607.

[58] Riccardo Catena and Paolo Gondolo. Global fits of the dark matter-nucleon effective interactions. *J. Cosmol. Astropart. Phys.*, 1409(09):045, 2014, 1405.2637.

[59] D. S. Akerib et al. Results from a search for dark matter in the complete LUX exposure. *Phys. Rev. Lett.*, 118(2):021303, 2017, 1608.07648.

[60] C. E. Aalseth et al. DarkSide-20k: A 20 tonne two-phase LAr TPC for direct dark matter detection at LNGS. *Eur. Phys. J. Plus*, 133(3):131, 2018, 1707.08145.

[61] P. Agnes et al. First Results from the DarkSide-50 Dark Matter Experiment at Laboratori Nazionali del Gran Sasso. *Phys. Lett.*, B743:456–466, 2015, 1410.0653.

[62] Jonathan H. Davis. Fitting the annual modulation in DAMA with neutrons from muons and neutrinos. *Phys. Rev. Lett.*, 113:081302, 2014, 1407.1052.

[63] C. Tomei. SABRE: Dark matter annual modulation detection in the northern and southern hemispheres. *Nucl. Instrum. Meth.*, A845:418–420, 2017.

[64] Walter C. Pettus. DM-Ice: Current Status and Future Prospects. In *Proceedings, 12th Conference on the Intersections of Particle and Nuclear Physics (CIPANP 2015): Vail, Colorado, USA, May 19-24, 2015*, 2015, 1510.00378.

[65] Julio Amare et al. The ANAIS Dark Matter Project: Status and Prospects. In *Proceedings, 14th Marcel Grossmann Meeting on Recent Developments in Theoretical and Experimental General Relativity, Astrophysics, and Relativistic Field Theories (MG14) (In 4 Volumes): Rome, Italy, July 12-18, 2015*, volume 3, pages 2414–2419, 2017, 1601.01184.

[66] E. Behnke et al. First Dark Matter Search Results from a 4-kg CF_3I Bubble Chamber Operated in a Deep Underground Site. *Phys. Rev.*, D86(5):052001, 2012, 1204.3094. [Erratum: Phys. Rev.D90,no.7,079902(2014)].

[67] M. Felizardo, T. A. Girard, T. Morlat, A. C. Fernandes, A. R. Ramos, and J. G. Marques. Recent results from the SIMPLE dark matter search. *J. Phys. Conf. Ser.*, 375:012011, 2012.

[68] E. Behnke et al. Final Results of the PICASSO Dark Matter Search Experiment. *Astropart. Phys.*, 90:85–92, 2017, 1611.01499.

[69] C. Amole et al. Dark Matter Search Results from the PICO-60 C_3F_8 Bubble Chamber. *Phys. Rev. Lett.*, 118(25):251301, 2017, 1702.07666.

[70] R. Agnese et al. Search for Low-Mass Weakly Interacting Massive Particles Using Voltage-Assisted Calorimetric Ionization Detection in the SuperCDMS Experiment. *Phys. Rev. Lett.*, 112(4):041302, 2014, 1309.3259.

[71] R. Agnese et al. Demonstration of Surface Electron Rejection with Interleaved Germanium Detectors for Dark Matter Searches. *Appl. Phys. Lett.*, 103:164105, 2013, 1305.2405.

[72] S. W. Leman. Review Article: Physics and Monte Carlo Techniques as Relevant to Cryogenic, Phonon and Ionization Readout of CDMS Radiation-Detectors. *Rev. Sci. Instrum.*, 83:091101, 2012, 1109.1193.

[73] Deep science: Underground physics. http://www.deepscience.org/contents/underground_universe.shtml. [Online; accessed 4-November-2014].

[74] SuperCDMS collaboration. The SuperCDMS SNOLAB Experiment. *DOE Proposal*, Nov. 2013.

[75] D. S. Akerib et al. Design and performance of a modular low-radioactivity readout system for cryogenic detectors in the CDMS experiment. *Nucl. Instrum. Meth.*, A591:476–489, 2008.

[76] Z. Ahmed et al. Dark Matter Search Results from the CDMS II Experiment. *Science*, 327:1619–1621, 2010, 0912.3592.

[77] R. Agnese et al. Low-mass dark matter search with CDMSlite. *Phys. Rev.*, D97(2):022002, 2018, 1707.01632.

[78] J. Lindhard, M. Scharff, and H.E. Schiott. Range Concepts And Heavy Ion Ranges (Notes On Atomic Collisions II). *Mat. Fys. Medd. Dan. Vid. Selsk.*, 33(14), 1963.

[79] J. Lindhard, V. Nielsen, M. Scharff, and P. V. Thomsen. Integral Equations Governing Radiation Effects (Notes On Atomic Collisions III). *Mat. Fys. Medd. Dan. Vid. Selsk.*, 33(10), 1963.

[80] J. Lindhard, Vibeke Nielsen, and M. Scharff. Approximation Method In Classical Scattering By Screened Coulomb Fields (Notes on Atomic Collisions, I). *Mat. Fys. Medd. Dan. Vid. Selsk.*, 36(10), 1968.

[81] R. Agnese et al. Nuclear-recoil energy scale in CDMS II silicon dark-matter detectors. 2018, 1803.02903.

[82] D. Barker and D. M. Mei. Germanium Detector Response to Nuclear Recoils in Searching for Dark Matter. *Astropart. Phys.*, 38:1–6, 2012, 1203.4620.

[83] P. Zecher, D. Wang, J. Rapaport, C. J. Martoff, and B. A. Young. Energy deposition of energetic silicon atoms within a silicon lattice. *Phys. Rev. A*, 41:4058–4061, 1990.

[84] G. Gerbier et al. Measurement of the ionization of slow silicon nuclei in silicon for the calibration of a silicon dark-matter detector. *Phys. Rev. D*, 42:3211–3214, 1990.

[85] Brian L. Dougherty. Measurements of ionization produced in silicon crystals by low-energy silicon atoms. *Phys. Rev.*, A45(3):2104, 1992.

[86] A. E. Chavarria et al. Measurement of the ionization produced by sub-keV silicon nuclear recoils in a CCD dark matter detector. *Phys. Rev.*, D94(8):082007, 2016, 1608.00957.

[87] F. Izraelevitch et al. A measurement of the ionization efficiency of nuclear recoils in silicon. *JINST*, 12(06):P06014, 2017, 1702.00873.

[88] A. R. Sattler. Ionization Produced by Energetic Silicon Atoms within a Silicon Lattice. *Phys. Rev.*, 138:A1815–A1821, 1965.

[89] K. W. Jones and H. W. Kraner. Stopping of 1- to 1.8-keV Ge-73 Atoms in Germanium. *Phys. Rev.*, C4:125–129, 1971.

[90] K. W. Jones and H. W. Kraner. Energy lost to ionization by 254-eV Ge-73 atoms stopping in Ge. *Phys. Rev.*, A11:1347–1353, 1975.

[91] P. S. Barbeau, J. I. Collar, and O. Tench. Large-Mass Ultra-Low Noise Germanium Detectors: Performance and Applications in Neutrino and Astroparticle Physics. *JCAP*, 0709:009, 2007, nucl-ex/0701012.

[92] Z. Ahmed et al. Results from a Low-Energy Analysis of the CDMS II Germanium Data. *Phys. Rev. Lett.*, 106:131302, 2011, 1011.2482.

[93] Y. Messous. Calibration of a Ge crystal with nuclear recoils for the development of a dark matter detector. *Astropart. Phys.*, 3:361–366, 1995.

[94] T. Shutt, B. Ellman, P. D. Barnes, Jr., A. Cummings, A. Da Silva, and J. Emes. Measurement of ionization and phonon production by nuclear recoils in a 60g crystal of germanium at 25-mK. *Phys. Rev. Lett.*, 69:3425, 1992.

[95] C. Chasman, K. W. Jones, H. W. Kraner, and Werner Brandt. Band-Gap Effects in the Stopping of Ge-72* Atoms in Germanium. *Phys. Rev. Lett.*, 21:1430–1433, 1968.

[96] A. R. Sattler, F. L. Vook, and J. M. Palms. Ionization Produced by Energetic Germanium Atoms within a Germanium Lattice. *Phys. Rev.*, 143:588–594, 1966.

[97] L. Baudis, J. Hellmig, H. V. Klapdor-Kleingrothaus, Yorck Alexander Ramachers, J. W. Hammer, and A. Mayer. High purity germanium detector ionization pulse shapes of nuclear recoils, gamma interactions and microphonism. *Nucl. Instrum. Meth.*, A418:348–354, 1998, hep-ex/9901028.

[98] E. Simon et al. SICANE: A Detector array for the measurement of nuclear recoil quenching factors using a monoenergetic neutron beam. *Nucl. Instrum. Meth.*, A507:643–656, 2003, astro-ph/0212491.

[99] D.M. Poehlmann et al. Characterization of Gadolinium-loaded Plastic Scintillator for Use as a Neutron Veto. 2018 (in preparation).

[100] The SuperCDMS Collaboration. SuperCDMS SNOLAB Technical Design Report. Technical report, California Institute of Technology *et al.* , April 2016.

[101] Z. W. Bell, G. M. Brown, C. H. Ho, and F. V. Sloop, Jr. Organic scintillators for neutron detection. *Proc. SPIE*, 4784:150–163, 2003.

[102] G.F. Knoll. *Radiation Detection and Measurement*. John Wiley, Danvers, MA, 4 edition, 2010.

[103] R. D. Breukers, C. M. Bartle, and A. Edgar. Transparent lithium loaded plastic scintillators for thermal neutron detection. *Nucl. Instrum. Meth*, A701:58–61, 2013.

[104] Isadore B. Berlman. 6 - graphs. In Isadore B. Berlman, editor, *Handbook of Fluorescence Spectra of Aromatic Molecules (Second Edition)*, pages 107 – 415. Academic Press, second edition edition, 1971.

[105] N. Zaitseva et al. Plastic scintillators with efficient neutron/gamma pulse shape discrimination. *Nucl. Instr. and Meth. A*, 668:88 – 93, 2012.

[106] S. Marrone et al. Pulse shape analysis of liquid scintillators for neutron studies. *Nucl. Instrum. Meth. A*, 490(1):299 – 307, 2002.

[107] N. Zaitseva, A. Glenn, H. P. Martinez, L. Carman, I. Pawelczak, M. Faust, and S. Payne. Pulse shape discrimination with lithium-containing organic scintillators. *Nucl. Instrum. Meth*, A729:747–754, 2013.

[108] Sigma-Aldrich. Gadolinium(iii) tris(isopropoxide). http://www.sigmaaldrich.com/catalog/product/aldrich/663948. [Online; accessed 1-May-2018].

[109] Alfa Aesar. Tris(2,2,6,6-tetramethyl-3,5-heptanedionato)gadolinium(iii). https://www.alfa.com/en/catalog/014486/. [Online; accessed 1-May-2018].

[110] L. Ovechkina, K. Riley, S. Miller, Z. W. Bell, and V. Nagarkar. Gadolinium loaded plastic scintillators for high efficiency neutron detection. *Phys. Proc.*, 2(2):161 – 170, 2009.

[111] G. H. V. Bertrand et al. Understanding the behaviour of different metals in loaded scintillators: discrepancy between gadolinium and bismuth. *J. Mater. Chem. C*, 3:6006–6011, 2015.

[112] C. Patrignani et al. Review of Particle Physics. *Chin. Phys.*, C40(10):100001, 2016.

[113] T.W. Burrows. Data produced by the code QCALC. National Nuclear Data Center, Brookhaven National Laboratory. Based on the Audi-Wapstra Atomic Mass Tables, G. Audi and A.H. Wapstra, The 1995 Update to the Atomic Mass Evaluation., *Nucl. Phys. A*595, 409 (1995).

[114] V.F. Sears. Neutron scattering lengths and cross sections. *Neutron News*, 3(3):26–37, 1992.

[115] C. D. Bass, E. J. Beise, H. Breuer, C. R. Heimbach, T. Langford, and J. S. Nico. Characterization of a Li-6 loaded liquid organic scintillator for fast neutron spectrometry and thermal neutron detection. *Appl. Radiat. Isot.*, 77:130–138, 2013, 1206.4036.

[116] Hamamatsu Photonics. *Opto-Semiconductor Handbook*. http://www.hamamatsu.com/us/en/hamamatsu/overview/bsd/solid_state_division/related_documents.html [Online; accessed 1-May-2017].

[117] P. M. Rubinov. (private communication).

[118] H. Chagani. *Studies of the Responses of Liquid and Solid Targets for Direct Dark Matter Searches*. PhD thesis, University of Sheffield, 2008.

[119] Hamamatsu Photonics. Photocathode Technology. http://www.hamamatsu.com/jp/en/technology/innovation/photocathode/index.html. [online; accessed 2-May-2018].

[120] Advatech UK Limited, "5 Glebe Avenue, Woodford Green, Essex, UK, IG8 9HB". *Silicon Photomultiplier CPTA 151-30*, 1 edition, July 2011.

[121] A.I. Bedrik et al. "plastic scintillator with gadolinium phenylpropionate". *Functional Materials 18*, 4:470–475, 2011.

[122] J.R. Lakowicz. *Principles of Fluorescence Spectroscopy*. Springer US, 3 edition, 2006.

[123] Saint-Gobain. Premium plastic scintillators. https://www.crystals.saint-gobain.com/sites/imdf.crystals.com/files/documents/sgc-bc400-404-408-412-416-data-sheet.pdf. [Online; accessed 23-April-2018].

[124] H. E. Rogers, D. G. Cerdeno, P. Cushman, F. Livet, and V. Mandic. Multidimensional effective field theory analysis for direct detection of dark matter. *Phys. Rev.*, D95(8):082003, 2017, 1612.09038.

[125] Anne M. Green. Determining the WIMP mass using direct detection experiments. *J. Cosmol. Astropart. Phys.*, 0708:022, 2007, hep-ph/0703217.

[126] Samuel D. McDermott, Hai-Bo Yu, and Kathryn M. Zurek. The Dark Matter Inverse Problem: Extracting Particle Physics from Scattering Events. *Phys. Rev.*, D85:123507, 2012, 1110.4281.

[127] Anne M. Green. Astrophysical uncertainties on direct detection experiments. *Mod. Phys. Lett.*, A27:1230004, 2012, 1112.0524.

[128] D. G. Cerdeño, M. Fornasa, J. H. Huh, and M. Peiro. Nuclear uncertainties in the spin-dependent structure functions for direct dark matter detection. *Phys. Rev.*, D87(2):023512, 2013, 1208.6426.

[129] Charlotte Strege, Roberto Trotta, Gianfranco Bertone, Annika H. G. Peter, and Pat Scott. Fundamental statistical limitations of future dark matter direct detection experiments. *Phys. Rev.*, D86:023507, 2012, 1201.3631.

[130] G. Bertone, D. G. Cerdeño, J. I. Collar, and B. C. Odom. WIMP identification through a combined measurement of axial and scalar couplings. *Phys. Rev. Lett.*, 99:151301, 2007, 0705.2502.

[131] Miguel Pato, Laura Baudis, Gianfranco Bertone, Roberto Ruiz de Austri, Louis E. Strigari, and Roberto Trotta. Complementarity of Dark Matter Direct Detection Targets. *Phys. Rev.*, D83:083505, 2011, 1012.3458.

[132] D. G. Cerdeño et al. Complementarity of dark matter direct detection: the role of bolometric targets. *J. Cosmol. Astropart. Phys.*, 1307:028, 2013, 1304.1758. [Erratum: JCAP1309,E01(2013)].

[133] A. Liam Fitzpatrick, Wick Haxton, Emanuel Katz, Nicholas Lubbers, and Yiming Xu. The Effective Field Theory of Dark Matter Direct Detection. *J. Cosmol. Astropart. Phys.*, 1302:004, 2013, 1203.3542.

[134] A. Liam Fitzpatrick, Wick Haxton, Emanuel Katz, Nicholas Lubbers, and Yiming Xu. Model Independent Direct Detection Analyses. 2012, 1211.2818.

[135] Nikhil Anand, A. Liam Fitzpatrick, and W. C. Haxton. Weakly interacting massive particle-nucleus elastic scattering response. *Phys. Rev.*, C89(6):065501, 2014, 1308.6288.

[136] Annika H. G. Peter, Vera Gluscevic, Anne M. Green, Bradley J. Kavanagh, and Samuel K. Lee. WIMP physics with ensembles of direct-detection experiments. *Phys. Dark Univ.*, 5-6:45–74, 2014, 1310.7039.

[137] Vera Gluscevic and Annika H. G. Peter. Understanding WIMP-baryon interactions with direct detection: A Roadmap. *J. Cosmol. Astropart. Phys.*, 1409(09):040, 2014, 1406.7008.

[138] Riccardo Catena. Prospects for direct detection of dark matter in an effective theory approach. *J. Cosmol. Astropart. Phys.*, 1407:055, 2014, 1406.0524.

[139] Riccardo Catena. Analysis of the theoretical bias in dark matter direct detection. *J. Cosmol. Astropart. Phys.*, 1409(09):049, 2014, 1407.0127.

[140] Vera Gluscevic, Moira I. Gresham, Samuel D. McDermott, Annika H. G. Peter, and Kathryn M. Zurek. Identifying the Theory of Dark Matter with Direct Detection. *J. Cosmol. Astropart. Phys.*, 1512(12):057, 2015, 1506.04454.

[141] Eugenio Del Nobile, Graciela B. Gelmini, and Samuel J. Witte. Prospects for detection of target-dependent annual modulation in direct dark matter searches. *J. Cosmol. Astropart. Phys.*, 1602(02):009, 2016, 1512.03961.

[142] Samuel J. Witte, Vera Gluscevic, and Samuel D. McDermott. Prospects for Distinguishing Dark Matter Models Using Annual Modulation. *J. Cosmol. Astropart. Phys.*, 1702(02):044, 2017, 1612.07808.

[143] F. Feroz, M. P. Hobson, and M. Bridges. MultiNest: an efficient and robust Bayesian inference tool for cosmology and particle physics. *Mon. Not. Roy. Astron. Soc.*, 398:1601–1614, 2009, 0809.3437.

[144] F. Feroz and M. P. Hobson. Multimodal nested sampling: an efficient and robust alternative to MCMC methods for astronomical data analysis. *Mon. Not. Roy. Astron. Soc.*, 384:449, 2008, 0704.3704.

[145] F. Feroz, M. P. Hobson, E. Cameron, and A. N. Pettitt. Importance Nested Sampling and the MultiNest Algorithm. 2013, 1306.2144.

[146] R. Agnese et al. Effective Field Theory Analysis of CDMSlite Run 2 Data. 2018 (in preparation).

[147] K. Schneck et al. Dark matter effective field theory scattering in direct detection experiments. *Phys. Rev.*, D91(9):092004, 2015, 1503.03379.

[148] R. Agnese et al. Improved WIMP-search reach of the CDMS II germanium data. *Phys. Rev.*, D92(7):072003, 2015, 1504.05871.

[149] D. S. Akerib et al. First results from the LUX dark matter experiment at the Sanford Underground Research Facility. *Phys. Rev. Lett.*, 112:091303, 2014, 1310.8214.

[150] D. S. Akerib et al. Improved Limits on Scattering of Weakly Interacting Massive Particles from Reanalysis of 2013 LUX Data. *Phys. Rev. Lett.*, 116(16):161301, 2016, 1512.03506.

[151] D. S. Akerib et al. Radiogenic and Muon-Induced Backgrounds in the LUX Dark Matter Detector. *Astropart. Phys.*, 62:33–46, 2015, 1403.1299.

[152] R. Agnese et al. Measurement of the Production of Tritium and Other Cosmogenic Isotopes in Germanium with CDMSlite. 2018 (in preparation).

[153] C. M. Lederer, J. M. Hollander, and I. Perlman. *Table of Isotopes*. Wiley, 6 edition, 1968.

[154] J. M. C. Brown, M. R. Dimmock, J. E. Gillam, and D. M. Paganin. A low energy bound atomic electron Compton scattering model for Geant4. *Nucl. Instrum. Meth.*, B338:77–88, 2014.

[155] D. Barker. Low Energy Background Spectrum in CDMSlite. *PoS*, ICHEP2016:874, 2016, 1611.05792.

[156] D. Barker. *TBD*. PhD thesis, University of Minnesota, 2018 (in preparation).

[157] F. T. Avignone et al. Theoretical and experimental investigation of cosmogenic radioisotope production in germanium. *Nucl. Phys. Proc. Suppl.*, 28A:280–285, 1992. [,280(1992)].

[158] A.B. Cohen. *Concepts of Nuclear Physics*. McGraw-Hill, 1971.

[159] H.E. Rogers and D. Barker. Dark matter effective field theory. (unpublished).

Appendix A

Calculation of Effective Operators

Note: This appendix was adapted from a paper written with D. Barker [159].

From the assumption that dark matter is fermionic, there are ten couplings between dark matter and quarks and four between dark matter and gluons. The interactions between dark matter and quarks assume a neutral Dirac field for dark matter and contain no flavor violating terms. These operators are listed in Table A.1, and the full interaction Lagrangian is

$$\mathcal{L}_{\text{eff}} = \sum_{k=1}^{10} \sum_{q} c_k^q \mathcal{O}_k^q + \sum_{k=1}^{4} c_k^g \mathcal{O}_k^g, \tag{A.1}$$

where $c_k^{(q,g)}$ is the coupling coefficient for the k-th operation with either quarks or gluons. From these operators the interactions between nucleons can be derived and from there to non-relativistic interactions with whole target nuclei [44].

Because the full relativistic interaction Lagrangian for dark matter with quarks and gluons is impractical for experimental observation, this Lagrangian must be reduced to an effective non-relativistic coupling between dark matter and the target nuclei. The first step in deriving the effective Lagrangian is to convert from quark and gluon couplings to proton and neutron couplings. From here the relativistic fields can be determined from non-relativistic Weyl spinors, and using nuclear form factors, the full effective interactions are calculated [133].

$\mathcal{O}_1^q = \overline{\chi}\chi\overline{q}q$	$\mathcal{O}_2^q = \overline{\chi}i\gamma^5\chi\overline{q}q$
$\mathcal{O}_3^q = \overline{\chi}\chi\overline{q}i\gamma^5 q$	$\mathcal{O}_4^q = \overline{\chi}i\gamma^5\chi\overline{q}i\gamma^5 q$
$\mathcal{O}_5^q = \overline{\chi}\gamma^\mu\chi\overline{q}\gamma_\mu q$	$\mathcal{O}_6^q = \overline{\chi}\gamma^\mu\gamma^5\chi\overline{q}\gamma_\mu q$
$\mathcal{O}_7^q = \overline{\chi}\gamma^\mu\chi\overline{q}\gamma_\mu\gamma^5 q$	$\mathcal{O}_8^q = \overline{\chi}\gamma^\mu\gamma^5\chi\overline{q}\gamma_\mu\gamma^5 q$
$\mathcal{O}_9^q = \overline{\chi}\sigma^{\mu\nu}\chi\overline{q}\sigma_{\mu\nu}q$	$\mathcal{O}_{10}^q = \overline{\chi}i\sigma^{\mu\nu}\gamma^5\chi\overline{q}\sigma_{\mu\nu}q$
$\mathcal{O}_1^g = \frac{\alpha_s}{12\pi}\overline{\chi}\chi G^a_{\mu\nu}G^a_{\mu\nu}$	$\mathcal{O}_2^g = \frac{\alpha_s}{12\pi}\overline{\chi}i\gamma^5\chi G^a_{\mu\nu}G^a_{\mu\nu}$
$\mathcal{O}_3^g = \frac{\alpha_s}{8\pi}\overline{\chi}\chi G^a_{\mu\nu}\tilde{G}^a_{\mu\nu}$	$\mathcal{O}_4^g = \frac{\alpha_s}{8\pi}\overline{\chi}i\gamma^5\chi G^a_{\mu\nu}\tilde{G}^a_{\mu\nu}$

Table A.1: Quark (upper) and gluon (lower) relativistic couplings to dark matter [44].

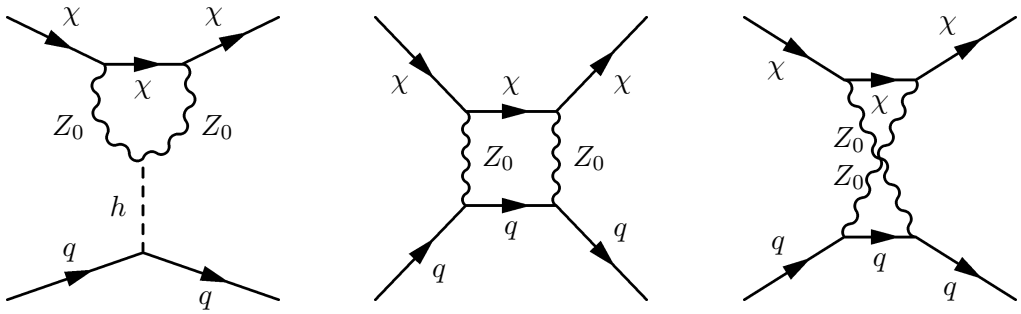

Figure A.1: One loop Feynman diagrams showing possible interactions between dark matter and quarks. From [9].

A.1 Dark Matter Coupling to Quarks

Figure A.1 shows three representative Feynman diagrams for interactions between dark matter and fermionic target matter. In order to consider an effective coupling, the one loop diagrams of Figure A.1 must be reduced to four-point interactions assuming fermionic dark matter. This calculation will be shown for the three interactions shown as an example for all of the relativistic EFT couplings. This interaction is mediated by the Z-boson, and because the mass of the Z-boson, $M_Z < \Lambda_{\rm QCD}$, the interactions between dark matter and baryonic matter should be with quarks and gluons. The momentum of the incoming (outgoing) dark matter particle is defined to be p_1 (p_2), the momentum of the incoming (outgoing) quark to be p_3 (p_4), and the internal momentum in the loop to be k. The form of the propagator for the Z-boson is

$$\frac{-i(g_{\mu\nu} - p_\mu p_\nu/M_Z^2)}{p^2 - M_Z^2}, \tag{A.2}$$

where $g_{\mu\nu}$ is the metric tensor. The propagator for a fermion, in this case both the quarks and dark matter, is

$$\frac{i(\not{p} + m_f)}{p^2 - m_f^2}. \tag{A.3}$$

The vertex factor between two fermions and a Z-boson is

$$\frac{i\epsilon g}{cos\theta_\omega}\gamma^\mu \frac{C_V^f - C_A^f\gamma^5}{2}, \tag{A.4}$$

where $\epsilon = 1$ for a quark and represents a modified coupling for a dark matter fermion, θ_ω is the Weinberg angle, and C_V^f and C_A^f are the vertex factors specific to the fermion involved. For the Higgs interactions, the propagator is

$$\frac{i}{p^2 - M_h^2} \tag{A.5}$$

with vertex factors from coupling to two Z-bosons of

$$\frac{i2M_Z^2 g_{\mu\nu}}{M_V} \tag{A.6}$$

and for the coupling with two fermions of

$$\frac{-im_f}{M_V} \tag{A.7}$$

where M_V is the vacuum excitation value of the Higgs field.

Applying conservation of momentum, $\delta(p_1 + p_3 - p_2 - p_4)$, around the loop, the left diagram of Figure A.1 gives the following equation for the loop correction of this diagram:

$$\begin{aligned} D_1 = \int \frac{d^4k}{(2\pi)^4} &\left(\frac{i\epsilon g}{\cos\theta_\omega}\gamma^\rho \frac{C_V^\chi - C_A^\chi\gamma^5}{2}\right)\left(\frac{i(\not{k} + \not{p}_1 + m_\chi}{(k+p_1)^2 - m_\chi^2}\right)\left(\frac{-i\epsilon g}{\cos\theta_\omega}\gamma^\rho \frac{C_V^\chi - C_A^\chi\gamma^5}{2}\right) \\ &\times \left(\frac{-i\left(g_{\nu\rho} - [(k+p_1-p_2)_{nu}(k+p_1-p_2)_\rho]/M_Z^2\right)}{(k+p_1-p_2)^2 - M_Z^2}\right)\left(2i\frac{M_Z^2}{M_V}g^{\mu\nu}\right) \\ &\times \left(\frac{-i\left(g_{\rho\mu} - [k_\rho k_\mu]/M_Z^2\right)}{k^2 - M_Z^2}\right). \end{aligned} \tag{A.8}$$

The momentum of the dark matter particle is not expected to change in the interaction; therefore, assuming $p_1 \approx p_2$, and $M_Z \gg k$, this reduces to

$$D_1 = -\frac{\epsilon^2 g^2 M_Z^2}{2M_V \cos^2\theta_\omega} \int \frac{d^4k}{(2\pi)^4} \gamma^\rho \left(C_V^\chi - C_A^\chi \gamma^5\right) \left(\frac{i(\not{k} + \not{p}_1 + m_\chi}{(k+p_1)^2 - m_\chi^2}\right) \gamma^\rho \left(C_V^\chi - C_A^\chi \gamma^5\right) \times \left(\frac{g_{\nu\rho}}{k^2 - M_Z^2}\right) g^{\mu\nu} \left(\frac{g_{\rho\mu}}{k^2 - M_Z^2}\right). \tag{A.9}$$

Simplifying further by contracting the Lorentz indices, the final integral for the loop correction is

$$D_1 = -\frac{2\epsilon^2 g^2 M_Z^2}{M_V \cos^2\theta_\omega} \int \frac{d^4k}{(2\pi)^4} \frac{1}{\left[(k+p_1)^2 - m_\chi^2\right]\left[k^2 - M_Z^2\right]^2} \times \left(\left[\left(C_V^\chi\right)^2 + \left(C_A^\chi\right)^2\right](\not{k} + \not{p}_1 + m_\chi)\right). \tag{A.10}$$

This, however, is just the weak loop correction to the interaction of dark matter and quarks via the Higgs boson. Examining the Higgs propagator and vertex factors, Equations A.5, A.6, and A.7, shows that there is no additional gamma structure that will be added to this integral. Therefore, this can be identified from Table A.1, which lists all possible relativistic couplings between quarks or gluons and dark matter, as the form of $\mathcal{O}_5^q$.

Applying conservation of momentum for the middle diagram of Figure A.1 gives the following integral:

$$D_2 = \int \frac{d^4k}{(2\pi)^4} \left(\frac{-i\epsilon g}{\cos\theta_\omega} \gamma^\mu \frac{C_V^\chi - C_A^\chi \gamma^5}{2}\right) \left(\frac{i(\not{k} + \not{p}_1 + m_\chi)}{(k+p_1)^2 - m_\chi^2}\right) \left(\frac{-i\epsilon g}{\cos\theta_\omega} \gamma^\nu \frac{C_V^\chi - C_A^\chi \gamma^5}{2}\right) \times \left(\frac{-i\left(g_{\nu\sigma} - \left[(k+p_1-p_2)_\nu (k+p_1-p_2)_\sigma\right]/M_Z^2\right)}{(k+p_1-p_2)^2 - M_Z^2}\right) \times \left(\frac{-ig}{\cos\theta_\omega} \gamma^\sigma \frac{C_V^q - C_A^q \gamma^5}{2}\right) \left(\frac{i(\not{k} + \not{p}_1 - \not{p}_2 - \not{p}_4 + m_q)}{(k+p_1-p_2-p_4)^2 - m_q^2}\right) \times \left(\frac{-ig}{\cos\theta_\omega} \gamma^\delta \frac{C_V^q - C_A^q \gamma^5}{2}\right) \left(\frac{-i(g_{\delta\mu} - \left[k_\delta k_\mu\right]/M_Z^2)}{k^2 - M_Z^2}\right). \tag{A.11}$$

Similarly to D_1, assuming $p_1 \approx p_2$, $p_3 \approx p_4$, and $M_Z >> k$, this equation becomes

$$D_2 = \frac{\epsilon^2 g^4}{16\cos^4\theta_\omega} \int \frac{d^4k}{(2\pi)^4} \gamma^\mu \left(C_V^\chi - C_A^\chi \gamma^5\right) \left(\frac{(\not{k} + \not{p}_1 + m_\chi)}{(k+p_1)^2 - m_\chi^2}\right) \gamma^\nu \left(C_V^\chi - C_A^\chi \gamma^5\right) \times \left(\frac{g_{\nu\sigma}}{M_Z^2}\right) \gamma^\sigma \left(C_V^q - C_A^q \gamma^5\right) \left(\frac{(\not{k} - \not{p}_4 + m_q)}{(k-p_4)^2 - m_q^2}\right) \times \gamma^\delta \left(C_V^q - C_A^q \gamma^5\right) \left(\frac{g_{\delta\mu}}{M_Z^2}\right). \tag{A.12}$$

Contracting the gamma-matrices and expanding this equation gives a loop correction of the form

$$D_2 = \frac{\epsilon^2 g^4}{M_Z^4 cos^4\theta_\omega} \int \frac{d^4k}{(2\pi)^4} \frac{1}{(p^2 - m_\chi^2)(p'^2 - m_q^2)} [C_1 \not{p}\not{p}' + C_2 \not{p}\not{p}'\gamma^5 + C_3 m_q \not{p} + C_4 m_q \not{p}\gamma^5 + C_5 m_\chi \not{p}'\gamma^5 + C_6 m_\chi \not{p}' + C_7 m_\chi m_q \gamma^5 + c_8 m_\chi m_q] \tag{A.13}$$

where here, the C_i represents some function of C_V^χ, C_A^χ, C_V^q, and C_A^q, and p and p' have been defined as $p = k + p_1$ and $p' = k - p_4$. In comparison with Table A.1, each term can be matched with an effective operator. The first term matches $\mathcal{O}_9^q$, the second matches $\mathcal{O}_{10}^q$, the third and sixth match $\mathcal{O}_5^q$, the fourth and fifth match $\mathcal{O}_8^q$, the seventh matches $\mathcal{O}_4^q$, and the eighth term is $\mathcal{O}_1^q$ and $\mathcal{O}_4^q$.

The right diagram has the same gamma structure as the second. Because of the mixing of the momentum channels, the definitions of p and p' are changed to $p = k + p_1$ and $p' = k + p_3$, but the final correction is identical for all practical purposes.

A.2 Quark/Gluon Coupling to Nucleon Coupling

From the quark/gluon interactions with dark matter, the interactions to nucleons can be calculated. The interaction operators for nucleons are shown in Table A.2, and the new effective Lagrangian is

$$\mathcal{L}_{\text{eff}} = \sum_{k=1}^{10} \sum_{N=p,n} c_k^N \mathcal{O}_k^N, \tag{A.14}$$

where the coupling coefficients (c_k^N) are now for the nucleon-dark matter interactions. In order to compare with direct dark matter detection experiments, the degrees of freedom

$\mathcal{O}_1^N = \overline{\chi}\chi\overline{N}N$	$\mathcal{O}_2^N = \overline{\chi}i\gamma^5\chi\overline{N}N$
$\mathcal{O}_3^N = \overline{\chi}\chi\overline{N}i\gamma^5N$	$\mathcal{O}_4^N = \overline{\chi}i\gamma^5\chi\overline{N}i\gamma^5N$
$\mathcal{O}_5^N = \overline{\chi}\gamma^\mu\chi\overline{N}\gamma_\mu N$	$\mathcal{O}_6^N = \overline{\chi}\gamma^\mu\gamma^5\chi\overline{N}\gamma_\mu N$
$\mathcal{O}_7^N = \overline{\chi}\gamma^\mu\chi\overline{N}\gamma_\mu\gamma^5N$	$\mathcal{O}_8^N = \overline{\chi}\gamma^\mu\gamma^5\chi\overline{N}\gamma_\mu\gamma^5N$
$\mathcal{O}_9^N = \overline{\chi}\sigma^{\mu\nu}\chi\overline{N}\sigma_{\mu\nu}N$	$\mathcal{O}_{10}^N = \overline{\chi}i\sigma^{\mu\nu}\gamma^5\chi\overline{N}\sigma_{\mu\nu}N$

Table A.2: Nucleon relativistic couplings to dark matter [44].

we want in the Lagrangian are not quark/gluons or individual nucleons but the whole target nuclei [44].

As an example of how this calculation works, for the first relativistic operator, $\mathcal{O}_1^q$, we can start with the matrix element of the scalar quark,

$$\langle N|\,\overline{q}q\,|N\rangle\,. \tag{A.15}$$

Starting with the assumption of zero momentum transfer, the nucleon mass becomes $m_N = \langle N|\,\Theta_{\mu\mu}\,|N\rangle$ where $\Theta_{\mu\mu}$ is given by

$$\Theta_{\mu\mu} = \sum_q m_q\overline{q}q + \frac{\beta(\alpha_s)}{4\alpha_s}G^a_{\mu\nu}G^a_{\mu\nu} \tag{A.16}$$

and is the trace of the QCD energy momentum tensor. The field strength tensor, $G^a_{\mu\nu}$, is the equivalent of the QED $F_{\mu\nu}$ for gluons. The next step is to integrate out the heavy quarks. This gives a lowest order term that cancels an anomaly from the expansion of $\beta(\alpha_s)$ and leaves $\Theta_{\mu\mu}$ as

$$\Theta_{\mu\mu} = \sum_q m_q\overline{q}q - \frac{9\alpha_s}{8\pi}G^a_{\mu\nu}G^a_{\mu\nu}. \tag{A.17}$$

The gluon contribution to $\Theta_{\mu\mu}$ can be written as linear combinations of the light quarks by

$$\frac{-1}{m_N}\frac{9\alpha_s}{8\pi}\langle N|\,G^a_{\mu\nu}G^a_{\mu\nu}\,|N\rangle = 1 - \sum_{q=u,d,s} f^N_{Tq} \equiv f^N_{TG}, \tag{A.18}$$

where

$$f^N_{Tq} \equiv \frac{\langle N|\,m_q\overline{q}q\,|N\rangle}{m_N} \tag{A.19}$$

is the light quark contribution to the nucleon mass [44].

A scalar operator, S, such as $\mathcal{O}_1^N$, interacts with quarks as

$$\mathcal{L}_{Sq} = S \sum_q c_q \overline{q} q, \tag{A.20}$$

where c_q is the interaction coefficient. We also have the coupling of S to the gluons via a quark loop; therefore we add

$$\mathcal{L}_{Sg} = \frac{c_g}{\Lambda} \frac{\alpha_s}{12\pi} S G^a_{\mu\nu} G^a_{\mu\nu}. \tag{A.21}$$

From this interaction Lagrangian, we see that the coupling between the scalar and the gluons is generated at the loop level. The Λ in this equation is connected to the mass of the particles in the loop. From here, the interaction between the scalar and the nucleon can be written as

$$\mathcal{L}_{SN} = \langle N | \mathcal{L}_{Sq} + \mathcal{L}_{Sg} | N \rangle \, \overline{N} N \equiv c_N S \overline{N} N, \tag{A.22}$$

where N represents the nucleon field [44].

All of this gives an effective Lagrangian of the form

$$\mathcal{L}_{\text{eff}} = \sum_{k=1}^{10} \sum_{N=p,n} c_k^N \mathcal{O}_k^N. \tag{A.23}$$

The operators from this Lagrangian are listed in Table A.2. The coupling for the first operator is

$$c_{1,2}^N = \sum_{q=u,d,s} c_{1,2}^q \frac{m_N}{m_q} f_{Tq}^N + \frac{2}{27} f_{TG}^N \left(\sum_{q=c,b,t} c_{1,2}^q \frac{m_N}{m_q} - c_{1,2}^g m_N \right). \tag{A.24}$$

The quark scalar couplings, c^q, are normally assumed to be proportional to the mass of the quark, m_q. This assumption comes from an interaction between dark matter and quarks that is mediated by a Higgs-like particle that couples to the quark masses [44].

A.3 Relativistic Reduction

Using the effective dark matter interaction Lagrangian, the dark matter-nucleus amplitude can by calculated by coherently adding all of the interaction amplitudes from each individual nucleon in the nucleus. The bound state of the nucleons of a chosen target

nucleus affect the interaction of the dark matter with the nucleus. This interaction is expressed in a form factor function, as shown in Equations 4.6 and 4.7.

The matrix element for a given interaction is

$$ {}_{\text{out}}\langle \chi, N|\, \mathcal{O}_k^N\, |\chi, N\rangle_{\text{in}}\,. \tag{A.25} $$

This matrix element can be expressed in terms of the non-relativistic operators. In order to get to the non-relativistic limit, while still assuming fermionic dark matter, the states in the matrix element can be expanded as the solution to the Dirac equation, the Weyl spinor, in the non-relativistic limit. This is given by,

$$ \begin{aligned} u^s(p) = \begin{pmatrix} \sqrt{p^\mu \sigma_\mu}\xi^s \\ \sqrt{p^\mu \overline{\sigma}_\mu}\xi^s \end{pmatrix} &= \frac{1}{\sqrt{2(p^0+m)}} \begin{pmatrix} (p^\mu \sigma_\mu + m)\xi^s \\ (p^\mu \overline{\sigma}_\mu + m)\xi^s \end{pmatrix} \\ &= \frac{1}{\sqrt{4m}} \begin{pmatrix} (2m - \vec{p}\cdot\vec{\sigma})\xi^s \\ (2m + \vec{p}\cdot\vec{\sigma})\xi^s \end{pmatrix} + \mathcal{O}(\vec{p}^2). \end{aligned} \tag{A.26} $$

The Weyl spinor is reduced through the approximation that $p^\mu = (m, \vec{p}) + \mathcal{O}(\vec{p}^2)$ in the limit that the fermions are on-shell [44].

For operator, $\mathcal{O}_1^N$, this approximation gives, up to first order in three-momenta,

$$ \overline{u}(p')u(p) \approx 2m. \tag{A.27} $$

Contracting the fermionic dark matter and nucleon bilinears with the matrix elements of $\mathcal{O}_k^N$ gives

$$ \left\langle \mathcal{O}_1^N \right\rangle = \left\langle \mathcal{O}_5^N \right\rangle = 4 m_\chi m_N \mathcal{O}_1^{NR}. \tag{A.28} $$

Operators $\mathcal{O}_1^N$ and $\mathcal{O}_5^N$ both lead to $\mathcal{O}_1^{\text{NR}}$; therefore, direct detection experiments will not be able to distinguish between these relativistic operators. Also, if dark matter interacts via both scalar and vector exchange with quarks, strong cancellations or enhancements can happen between these operators for the scattering cross-section because of the quantum interference [44]. From here, the nuclear interactions are calculated as discussed previously.

Appendix B

Choice of Prior Probability Distributions for CDMSlite Run 2

Note: This chapter will be published in Agnese *et al.* [146].

In order to include each parameter describing an EFT operator in the likelihood calculation, the prior probability distribution of each parameter must be determined. For WIMP mass, there are two viable options for prior probability distributions. The first, a flat prior, is given by the equation

$$\Pr(m_\chi) = \begin{cases} \frac{1}{m_{\max}}, \ 0 \leq m_\chi \leq m_{\max} \\ 0, \ \text{otherwise} \end{cases}, \tag{B.1}$$

where $m_{\max} = 25$ GeV. The second is a flat-log prior with a lower bound of $m_{\min} = 0.1$ GeV and is given by

$$\Pr(\log m_\chi) = \begin{cases} \frac{1}{\log(m_{\max}) - \log(m_{\min})}, \ m_{\min} \leq m_\chi \leq m_{\max} \\ 0, \ \text{otherwise} \end{cases}. \tag{B.2}$$

Similarly, there are two possible prior probability distribution choices. The flat prior is given by

$$\Pr(A_i) = \begin{cases} \frac{1}{A_{i,\max} - A_{i,\min}}, \ A_{i,\min} \leq A_i \leq A_{i,\max} \\ 0, \ \text{otherwise} \end{cases}, \tag{B.3}$$

and the flat-log prior is given by

$$\Pr(\log A_i) = \begin{cases} \frac{1}{\log(A_{i,\max})-\log(A_{i,\min})}, & A_{i,\min} \leq A_i \leq A_{i,\max} \\ 0, \text{ otherwise} \end{cases}, \tag{B.4}$$

where $A_{i,\max}$ and $A_{i,\min}$ were chosen for each operator to span roughly 13 orders of magnitude around a low number of expected events that still allows for the detected spectrum to be a WIMP signal. In this way, the size of the parameter space for different operators is the same, which simplifies the comparisons of Bayesian evidences. Because the amplitude is calculated over such a large number of decades, the flat prior cannot sample the full likelihood in a meaningful way. Therefore, in order to compare the flat prior with the flat-log prior, the limits ($A_{i,\max}$ and $A_{i,\min}$) were modified to cover only two orders of magnitude around the around the 2σ confidence contour for the posterior distribution.

Using these sets of prior probability distributions results in four possible combinations of priors:

- Prior 1: flat m_χ and flat $\log(A_i)$
- Prior 2: flat m_χ and flat A_i
- Prior 3: flat $\log(m_\chi)$ and flat $\log(A_i)$
- Prior 4: flat $\log(m_\chi)$ and flat A_i

Prior 1 matches the priors chosen for the main analysis. Figure B.1 compares the resulting 2σ contours on coupling-coefficient amplitude and WIMP mass for each EFT operator from the likelihoods calculated using each prior choice. For each operator, the 2σ contours calculated for each prior combination agree to within a factor of 1 to ~ 2.5.

There are some sampling issues visible in Prior 3 and Prior 4. The flat-log prior for mass does not sample the high mass regions well. When the flat amplitude prior, which does not sample the low amplitude regions well, is combined with the flat-log mass (Prior 4), this can cause entire regions along the 2σ contour to be poorly sampled. This is most visible in Operator 10. Both Priors 3 and 4 show extra wiggles in the contour that are not visible in Priors 1 and 2. When comparing the upper limits for all four prior combinations, the ability to sample the region of interest well becomes more important.

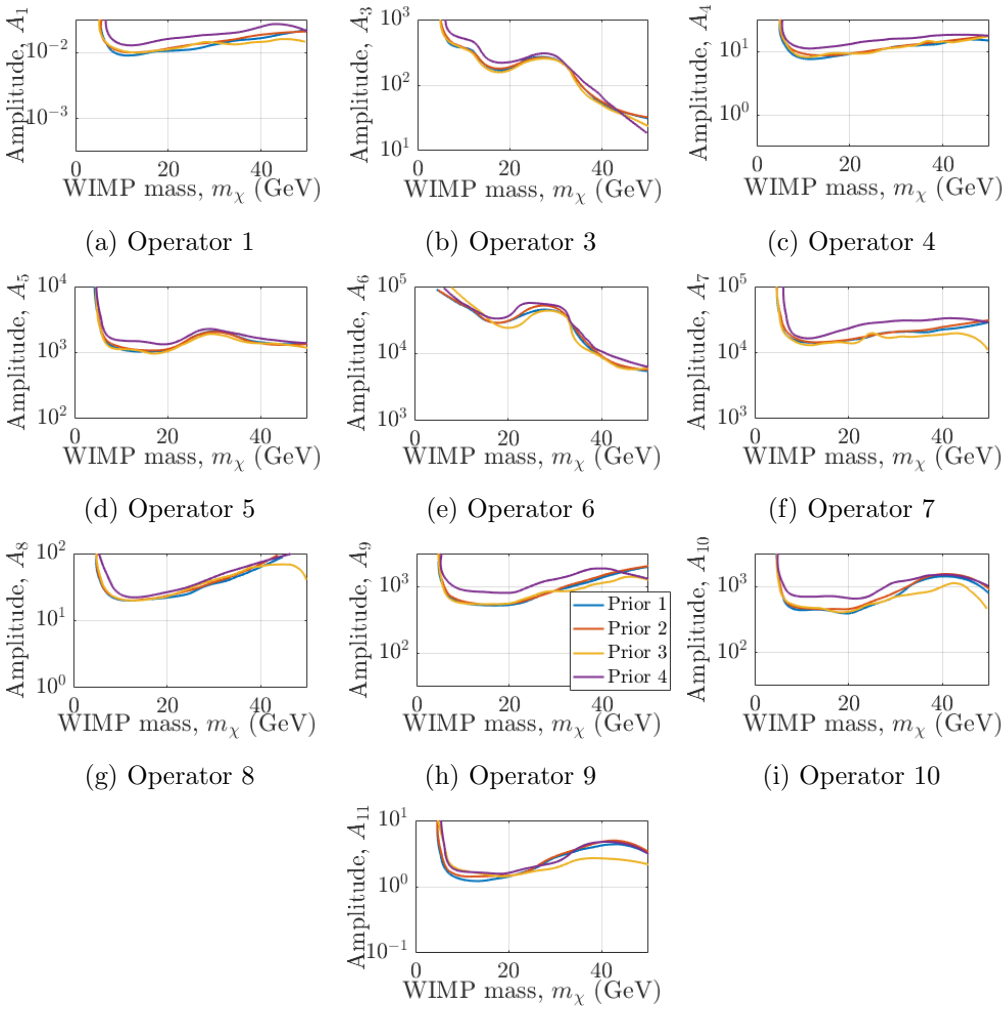

(a) Operator 1 (b) Operator 3 (c) Operator 4

(d) Operator 5 (e) Operator 6 (f) Operator 7

(g) Operator 8 (h) Operator 9 (i) Operator 10

(j) Operator 11

Figure B.1: Comparison of 2σ contours on the coupling-coefficient amplitude and WIMP mass using each prior combination for each EFT operator. Prior 1 is shown in blue, Prior 2 in orange, Prior 3 in yellow, and Prior 4 in purple.

Therefore, Prior 1 was chosen as the best prior probability distribution combination choice for the analysis.